OPEN ACCESS

JEOS-RP
Journal of the EOS
European Optical Society

The Journal of the European Optical Society – Rapid Publications

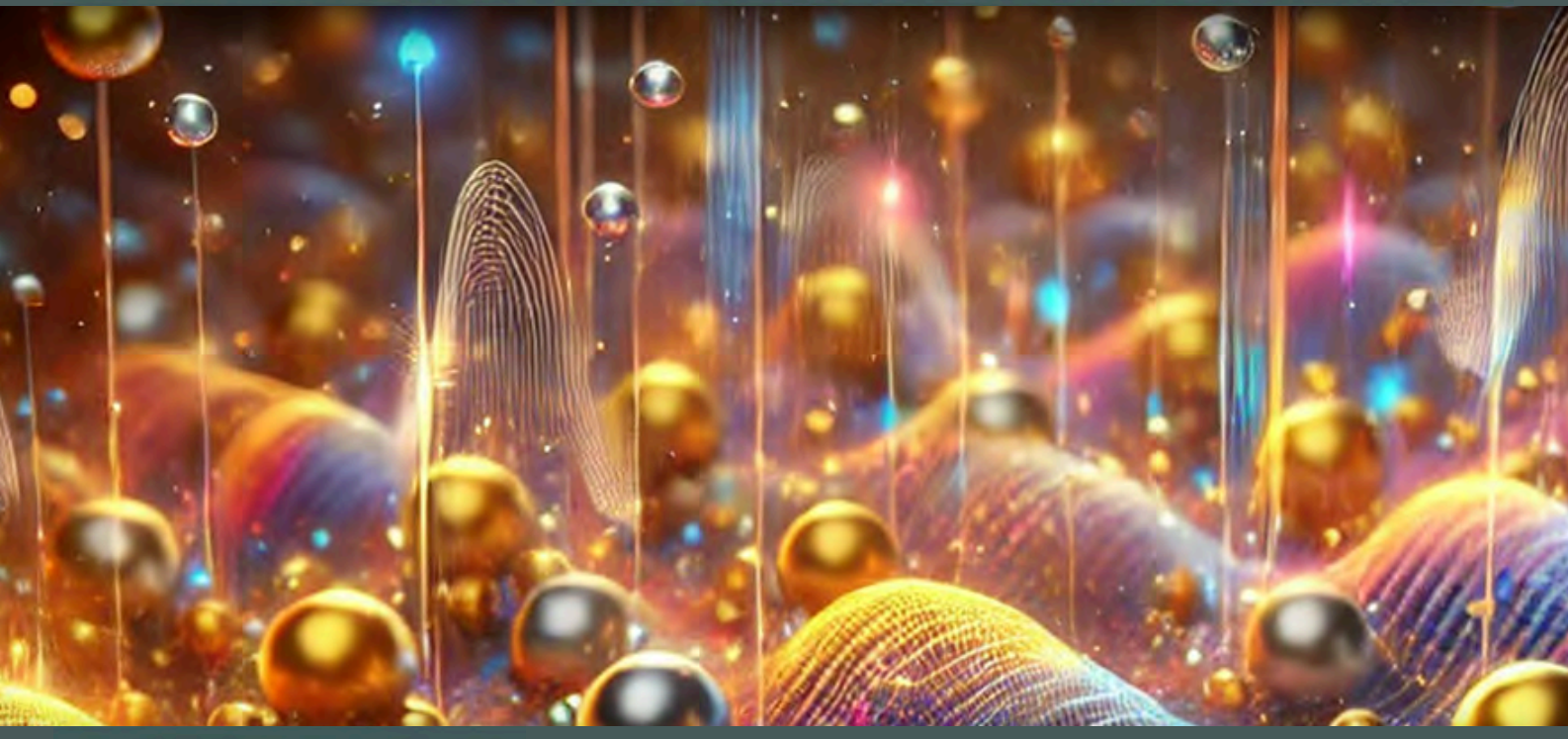

Topical Issue

PLASMONICA Collection

2024-2025

edp sciences

Table of Contents

Journal of the European Optical Society-Rapid Publications

EDITORIAL OPEN ACCESS

PLASMONICA Collection: a JEOS-RP benchmark for nano-photonics

Guest Editors: Nicoletta Granchi[1] and Antonino Foti[2]

[1] Department of Physics and Astronomy, Via Sansone 1, Sesto Fiorentino 50019, Italy; and LENS, University of Florence, Via Nello Carrara 1, Sesto Fiorentino 50019, Italy

[2] CNR-IPCF, Istituto per i Processi Chimico-Fisici del Consiglio Nazionale delle Ricerche – Viale F. Stagno D'Alcontres 37, I-98156, Messina, Italy)

PLASMONICA (https://www.plasmonica.it) represents the consolidated hub of the Italian nanophotonics community. What began in 2013 as a grassroots initiative created by a group of young researchers, has since flourished into a dynamic interdisciplinary environment that brings together researchers in physics, engineering, chemistry, biology, and materials science. Since 2015, PLASMONICA has operated as the Working Group on Plasmonics and Nano-Optics within the Italian Society for Optics and Photonics (SIOF), the Italian branch of the European Optical Society (EOS). Over the past decade, while keeping the originary brand of PLASMONICA, the community has expanded both in numbers and in scientific scope, branching out strongly into nano-optics and playing an increasingly recognized role across the European nano-photonics landscape. In fact, the annual workshop organized in Italy since 2013, has witnessed a growing interest and participation from foreign research groups, bringing international vitality to the PLASMONICA Italian community. Moreover, we are keen to highlight the steady endeavor of PLASMONICA in the proficient engagement of early-stage researchers through opportunities to present in our workshops and attend our doctoral schools.

This Topical Issue builds on this tradition by providing a fresh, appealing, and supportive publication pathway that reflects and reinforces the values of the community. This publication initiative associated with PLASMONICA has undergone a significant evolution. The Special Issue linked to the 2023 annual workshop, hosted at Politecnico di Milano, was originally envisioned as a celebratory milestone marking the tenth anniversary of the community. The wide range of contributions received highlights the diversity and vitality of the scientific activity flourishing within the PLASMONICA community. Petronijevic and Sibilia [1] have used numerical FDTD simulations to precisely tailor the directionality of second-harmonic emission from ZnO nanospheres. Simultaneously, the pursuit of low-loss platforms led Celebrano et al. [2] to investigate the epitaxial growth of high-quality Au thin films on MgO substrates, demonstrating a nearly threefold increase in surface plasmon polariton propagation length compared to conventional films. Challenging the reliance on long-range periodicity, Granchi et al. [3] provided experimental evidence that Anderson-localized modes in hyperuniform disordered photonic systems demonstrate predictable spectral scaling behavior analogous to that found in ordered photonic crystals, combining robustness with isotropy. To validate these complex designs, increasingly specialized characterization methods become crucial. For example, Mignuzzi et al. [4] employed spatially resolved cathodoluminescence spectroscopy to directly image the standing-wave pattern of the local density of optical states inside all-dielectric germanium Fabry–Pérot nanoresonators.

The powerful capabilities of photo-thermal techniques, which measure absorption directly without interference from scattered light, are also rapidly expanding. Skubisz et al. [5] introduced a new photo-acoustic spectroscopy setup utilizing a widely tunable laser and oblique incidence to measure extrinsic chirality in silver-coated metasurfaces. Furthermore, Petronijevic et al. [6] showcased the ability of the same technique to discriminate the absorption signal of a thin gold nanohole array against the strong, resonant background of a complex Si_3N_4-Si substrate by tuning the modulation frequency to enhance the contribution of the thin upper layer.

Finally, these advancements are rapidly translating into interesting applications in the biosensing field. Polito et al. [7] developed a platform featuring self-organized gold nanorods on SiO_2 to enhance infrared absorption spectroscopy, enabling to monitor light-induced conformational changes in the transmembrane protein Bacteriorhodopsin across the entire mid-infrared fingerprint region, providing crucial insight to understand the molecular functional mechanisms in complex biological systems. For non-invasive health monitoring, D'Andrea et al. [8] developed a low-cost, flexible, and wearable sensor chip based on patterned silver nanowires for surface-enhanced Raman spectroscopy (SERS). This chip allows the sensitive and label-free detection of biomarkers in human sweat in real time. Addressing another key diagnostic area, Montesi et al. [9] detailed the development of an automated microfluidic platform combined with a portable Raman spectrometer for on-site SERS analysis of microRNAs achieving picomolar detection limits comparable to sophisticated bench-top instruments.

Encouraged by this positive outcome, PLASMONICA, in collaboration with SIOF, EOS, and EDP Sciences, decided to broaden the scope of the initiative. Instead of remaining a one-off Special Issue, it has evolved into a permanent, open-ended PLASMONICA Collection within the *Journal of the European Optical Society – Rapid Publications (JEOS-RP)* [10]. This means

that, unlike traditional special issues, the Collection aims to be an evolving and updated benchmark for plasmonics and nanophotonics, offering at the same time an outlet where researcher's work can be highlighted within a coherent and visible framework. To ensure a consistently high standard of cutting-edge research while closely aligning with the emerging topics most valued by the PLASMONICA community, the guest editors of the PLASMONICA Collection will frequently rotate among the organizing members of the annual workshop and the members of the Steering Committee.

This transformation reflects a broader strategic vision. The Collection aims not only to showcase the scientific contributions of the PLASMONICA community, but also to strengthen JEOS-RP's presence as a natural publication venue for European research in plasmonics and nano-optics, directly supporting a scientific society-driven publishing model, where the value generated by authors and reviewers remains within the scientific community itself. Such an approach is particularly relevant in the current publishing landscape, where much of Europe's research output in optics is scattered across profit-making or non-European journals.

As we assume the role of guest editors for this new phase, we also would like to express our sincere gratitude to SIOF and EOS, in particular to Paolo Biagioni of Politecnico di Milano, Italy (co-founder of PLASMONICA, past president SIOF and presently in the EOS Board of Directors) and Emiliano Descrovi of Politecnico of Torino (EOS president and longtime PLASMONICA member), for their valuable contribution in conceiving and supporting this publishing model. We also want to warmly thank Attilio Zilli of Politecnico di Milano, Italy (member of the PLASMONICA Steering Committee), who coordinated the initial part of this Topical Issue and the transition towards the open-ended Collection. We are delighted to continue fostering this shared endeavor and to follow the scientific developments that will populate the PLASMONICA Collection hoping to set a positive example that can be imitated by different communities across the entire European optics and photonics landscape.

References

1 Petronijevic E, Sibilia C, Tailoring second harmonic emission by ZnO nanostructures: Enhancement of directionality, *J. Eur. Opt. Society-Rapid Publ.* **20**, 1, 11 (2024). https://doi.org/10.1051/jeos/2024009.

2 Celebrano M, Savoini M, Biagioni P, Della Valle G, Pellegrini G, Cantoni M, Rinaldi C, Cattoni A, Petti D, Bertacco R, Duò L, Finazzi M, Towards the epitaxial growth of Au thin lms on MgO substrates for plasmonic applications, *J. Eur. Opt. Society-Rapid Publ.* **20**, 1, 12 (2024). https://doi.org/10.1051/jeos/2024011.

3 Granchi N, Calusi G, Gonzini C, Lodde M, Stokkereit K, van Veldhoven PJ, Fiore A, Florescu M, Intonti F, Photonic crystal-like scaling behavior of localized Anderson modes in hyperuniform disordered systems, *J. Eur. Opt. Society-Rapid Publ.* **21,** 44 (2025). https://doi.org/10.1051/jeos/2025039.

4 Mignuzzi S, Wu X, Hecht B, Frigerio J, Isella G, Celebrano M, Finazzi M, Sapienza R, Biagioni P, Germanium Fabry-Perot nanoresonators investigated by cathodoluminescence spectroscopy, *J. Eur. Opt. Society-Rapid Publ.* **20,** 1, 14 (2024). https://doi.org/10.1051/jeos/2024012.

5 Skubisz C, Petronijevic E, Leahu G, Cesca T, Scian C, Mattei G, Sibilia C, Belardini A, Photo-acoustic technique with widely tuneable laser: Metasurface circular dichroism response, *J. Eur. Opt. Society-Rapid Publ.* **20**, 1, 20 (2024). https://doi.org/10.1051/jeos/2024016.

6 Petronijevic E, Ali H, Freddi S, Anzi L, Sordan R, Bollani M, Andreani LC, Belardini A, Photo-acoustic spectroscopy detects nanostructures against resonant and absorbing substrates, *J. Eur. Opt. Society-Rapid Publ.* **21**, 49 (2025). https://doi.org/10.1051/jeos/2025048.

7 Polito R, Sotgiu S, Sohrabi F, Ferrando G, Berkmann F, Temperini ME, Giliberti V, Buatier de Mongeot F, Ortolani M, Baldassarre L, Giordano MC, Polarization-resolved surface-enhanced infrared spectra with nanosensors based on self-organized gold nanorods, *J. Eur. Opt. Society-Rapid Publ.* **20**, 1, 15 (2024). https://doi.org/10.1051/jeos/2024015.

8 D'Andrea C, Banchelli M, Amicucci C, Polykretis P, Micheletti F, de Angelis M, Hwang B, Matteini P, Development of a wearable surface enhanced Raman scattering sensor chip based on silver nanowires for rapid detection of urea, lactate and pH in sweat, *J. Eur. Opt. Society-Rapid Publ.* **20**, 1, 10 (2024). https://doi.org/10.1051/jeos/2024013.

9 Montesi D, Bertone S, Rivolo P, Geobaldo F, Giorgis F, Novara C, Chiadò A. Towards a portable setup for the on-site SERS detection of miRNAs, *J. Eur. Opt. Society-Rapid Publ.* **20**, 1, 28 (2024). https://doi.org/10.1051/jeos/2024028.

10 Foti A, Zilli A, PLASMONICA and JEOS-RP: A new partnership for European nanophotonics, *J. Eur. Opt. Society-Rapid Publ.* **20**, E1 (2024). https://doi.org/10.1051/jeos/2024038.

J. Eur. Opt. Society-Rapid Publ. 2024, **20**, 11
© The Author(s), published by EDP Sciences, 2024
https://doi.org/10.1051/jeos/2024009
Available online at: https://jeos.edpsciences.org

Special Issue -Plasmonica 2023
Antonino Foti and Attilio Zilli (Guest editors)

Journal of the European Optical Society-Rapid Publications

RESEARCH ARTICLE OPEN ACCESS

Tailoring second harmonic emission by ZnO nanostructures: Enhancement of directionality

Emilija Petronijevic* and Concita Sibilia

Sapienza University of Rome, SBAI Department, Rome 00161, Italy

Received 28 December 2023 / Accepted 28 February 2024

Abstract. Tailoring nonlinear optical properties at the nanoscale is a hot topic in nowadays nanophotonics, promising for applications spanning from sensing to ultrafast optical communications. Here we present a numerical approach of designing a simple semiconductor nanostructure able to tailor second harmonic emission in the near- and far-field. We start from linear simulations of ZnO nanospheres, which reveal multipolar nature of the scattering. Next, we show how the same nanospheres, with radii in 30–130 nm range, excited at 800 nm, manipulate the directivity of the emitted second harmonic. We observe that the nanospheres which exhibit Kerker condition at 400 nm, emit the second harmonic field in the forward direction. We further investigate how the asymmetry (ellipsoid geometry) tailors the second harmonic directivity. We finally introduce geometry with low chiro-optical response, and observe that the second harmonic far-field depends on the handedness of the light exciting the nanostructure at 800 nm.

Keywords: Nanostructures, Nanophotonics, Nonlinear, Electromagnetic simulations.

1 Introduction

Dielectric and semiconductor nanostructures in low refractive index media support both electric and magnetic resonances, thus controlling the scattered field directionality and intensity [1]. Their low ohmic losses in the near-infrared and visible light spectra offer advantages in novel nanophotonic components, aiming at applications in biosensing, emission control, and all-optical manipulation [2–4]. Furthermore, exploring nonlinear properties of all-dielectric nanostructured media offers unique possibilities to enhance harmonic generation and tailor its radiation pattern [4–7].

ZnO is a wide direct bandgap semiconductor already widely applied in industry. With the progress of nanotechnology, micro- and nanostructuring of ZnO showed promise in efficient room-temperature nanophotonic devices based on microcavities [8] and nanowires [9]. Moreover, ZnO is non-centrosymmetric, offering efficient nonlinear optical properties at visible frequencies [10, 11]. Combining well-developed colloidal manufacturing of ZnO [12] with electromagnetic tailoring of its nonlinear properties could open fertile field in colloidal nonlinear nanophotonics.

In this numerical work, we investigate linear and nonlinear optical properties of various single ZnO nanostructures, immersed in water. We perform simulations of multipole decomposition and investigate how the supported modes tailor the second harmonic response. Starting from the nanosphere geometry, we further introduce the asymmetry, and, finally, low chiro-optical response, showing that the far-field second harmonic distribution strongly depends on the nanoparticle shape and the incident polarization.

2 Results and discussion

We perform full-wave 3D simulations based on the finite-difference-time-domain (FDTD) method in Lumerical [13]. First, a single nanosphere of radius r is considered for linear scattering in water (FDTD medium refractive index is set to 1.33); complex refractive index of ZnO is taken from ref. [14]. FDTD region is defined by perfectly matched layers (PMLs) in all directions, and the nanosphere is excited by a linearly polarized total-field-scattered-field (TFSF) source from the top (negative z-direction, normal incidence). Total scattering cross-section in the 300–1000 nm range is resolved into electric dipole (ED), magnetic dipole (MD), electric quadrupole (EQ) and magnetic quadrupole (MQ) by means of MENP, an open-source MATLAB-based solver for multipole expansion [15]. In Figure 1 we plot such decomposition for nanospheres with radiuses from 30 nm to 130 nm (with 20 nm step). While MENP method is in principle not restricted to this radii range, we chose it to bring the ZnO resonances in the visible range which is of interest

* Corresponding author: emilija.petronijevic@uniroma1.it

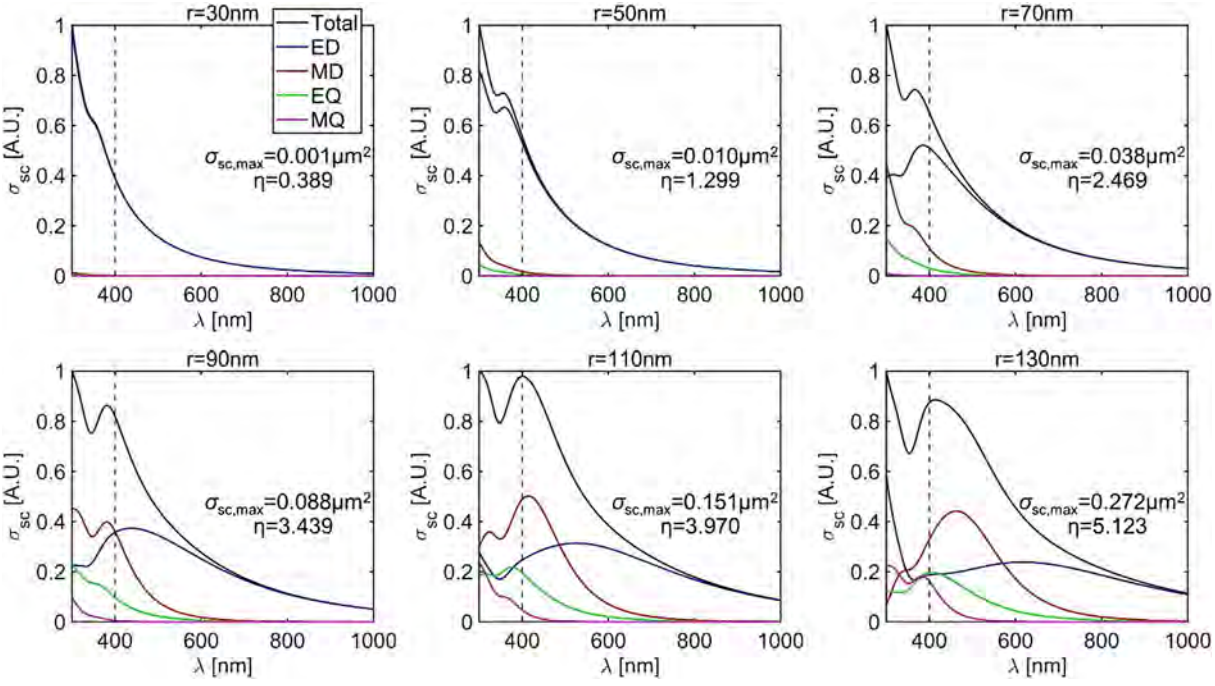

Figure 1. Multipole decomposition in ZnO nanospheres as a function of radius r; each panel is normalized to the maximum of the total scattering, indicated by $\sigma_{sc,max}$, while the scattering efficiency η indicates this maximum, normalized to the geometric cross-section.

for the future experimental work in our laboratory (e.g. excitation at 800 nm, and second harmonic measurements at 400 nm). Each panel in Figure 1 is normalized by the maximum total scattering $\sigma_{sc,max}$, while the scattering efficiency η is defined as $\sigma_{sc,max}$ normalized to geometric cross-section of the respective nanosphere. As expected, increasing the nanosphere radius red shifts the spectra and increases $\sigma_{sc,max}$, leading to a peak around 400 nm. For radiuses $r = 30 - 50$ nm, the ED mode is largely responsible for the scattering, while from $r = 70$ nm, other modes have non-negligible contribution. From $r = 90$ nm, the leading mode at 400 nm is MD mode, having its peak in this range. Interestingly, for $r = 90$ nm, ED and MD overlap around 400 nm, offering the possibility for the first Kerker condition and suppression of backward scattering [2, 16]. We note that the spectral position of the scattering resonances agrees well with the previous experimental results on ZnO nanospheres [17, 18]: in these works, photo-acoustic spectroscopy was applied to measure photothermal response of the sample and extract both absorption and scattering coefficients.

We next investigate the second harmonic far-field distribution if the nanosphere were excited at 800 nm, as in the experimental set-up which we used in previous works treating materials synthetized from [19] or containing ZnO [11]. These simulations are performed using a narrow band 800 nm excitation, with the FDTD continuous wave normalization switched off, to remove the excitation pulse influence on the collection of the results at 400 nm. As we are interested in studying the nanostructure shape influence on the far-field pattern, we approximate the ZnO nonlinearities with a non-dispersive, isotropic material having $\chi^{(2)} = 7.5$ pm/V [20]; this material is a user-defined "chi2" material model in Lumerical, which takes the linear optical properties from already defined ZnO complex refractive index, and adds the nonlinearity by importing a non-zero $\chi^{(2)}$. We underline that this is an approximation which takes into account the shape influences on the second order response, and not the ZnO anisotropy, while highly crystalline ZnO nanoparticles have anisotropic $\chi^{(2)}$ tensor (i.e. c-axis grown ZnO has five nonvanishing tensor elements). In Lumerical, it is currently easy to implement the extension of this method to materials with diagonal anisotropy. To excite the second harmonic response, we increase the excitation beam amplitude (TFSF source at 800 nm) to 10^{10} eV/m. The scattered field distribution is monitored by six monitors surrounding the TFSF source; the global monitor properties are set to override the source limits and detect fields at 400 nm instead.

Exciting the different nanospheres at 800 nm, we calculate near-fields in the xz-plane, and far-field distributions in the xy and xz planes, emitted by the nanosphere at 400 nm. The nanosphere is excited from the top, and the XZ far-field plane shows fields scattered in the forward and backward directions; the XY far-field plane shows laterally scattered fields, as seen in the inset of Figure 2; this inset also shows the spectrum of a time monitor, clearly showing the excitation spectrum and the nonlinear response generation. We examine dimensions around the Kerker condition; the strongest scattering is in the forward direction, hence we normalize each polar plot with its maximum scattering intensity in the forward direction. From XZ far-field results, we also extract the forward-to-backward ratio, (F/B). For $r = 70$ nm, there is a strong contribution of ED, and the

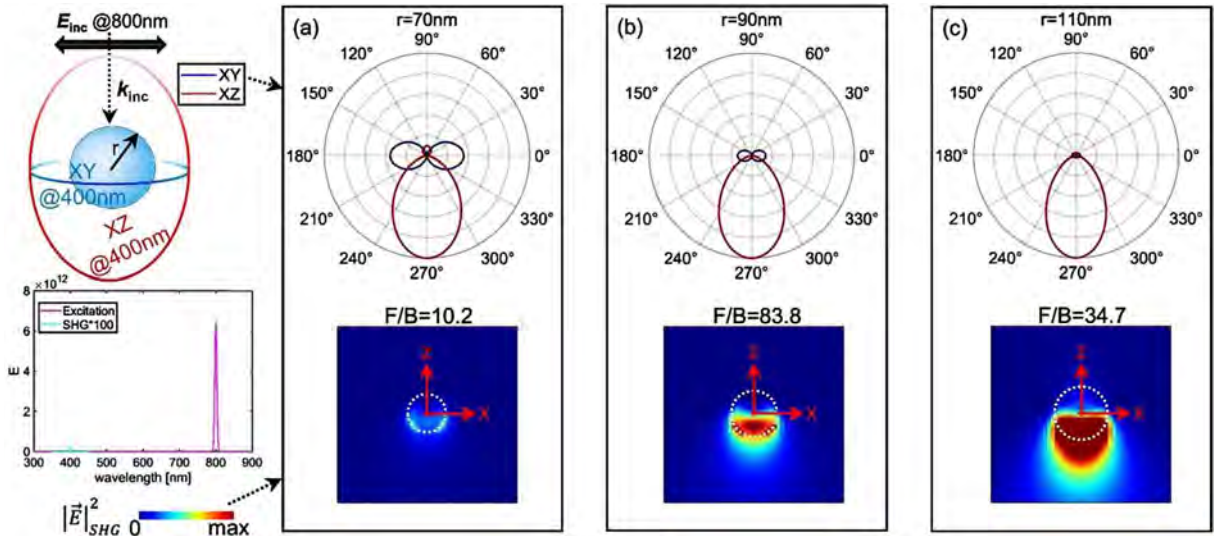

Figure 2. Second harmonic far-field radiation pattern in XY (blue) and XZ (red) planes, calculated for a nanosphere with radius (a) $r = 70$ nm, (b) $r = 90$ nm, and (c) $r = 110$ nm; each polar plot is normalized to the maximum forward (XZ) scattering. Below each polar plot, we show forward to backward (F/B) ratio, followed by the near-field distribution of electric field intensity at 400 nm, plotted in the xz-plane. Inset shows planes of the scattering geometry, the spectrum response result from a time monitor, and the electric field intensity color scale (equal for all nanospheres).

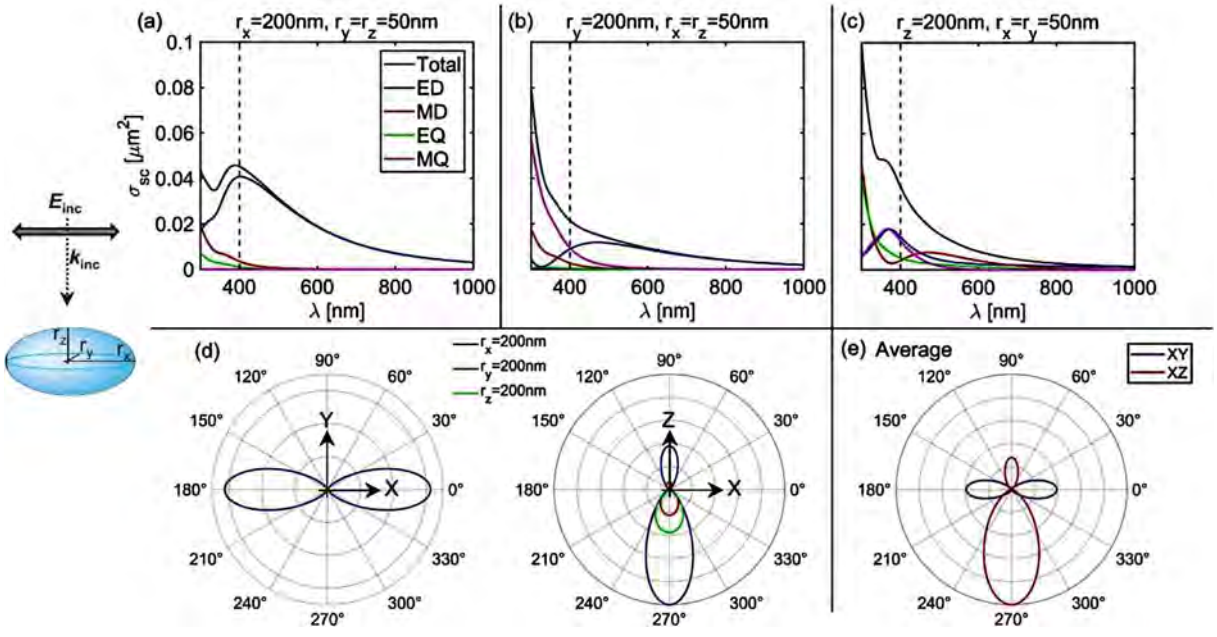

Figure 3. (a)–(c) Multipole decomposition in ZnO nanoellipsoids as a function of direction: (a) $r_x = 200$ nm, $r_y = r_z = 50$ nm, (b) $r_y = 200$ nm, $r_x = r_z = 50$ nm, (c) $r_z = 200$ nm, $r_x = r_y = 50$ nm. (d) XY and XZ scattering planes of the second harmonic for previous cases; blue, red, and green color define the long axis of the ellipsoid in the x-, y- and z-direction, respectively. All polar plots are normalized to the maximum forward scattering of the x-oriented ellipsoid. (e) Second harmonic emitted in XY and XZ direction, averaged over the three orientations, and normalized to the maximum scattering in the forward direction.

in-plane scattering is non-negligible, Figure 2a; F/B is 10.2. Increasing the radius to overlap ED and MD, F/B increases to 83.8, and the lateral scattering is much lower, Figure 2b. Finally, at the large radius of $r = 110$ nm, there is a strong forward and negligible lateral emission, Figure 2c, while F/B ratio drops to 34.7. These results show that even a simple nanosphere radius choice tailors the second harmonic field directivity in relation to the modes supported at this wavelength. While the directivity and F/B ratio depend on the nanosphere radius, the total scattered field at 400 nm is the highest for $r = 110$ nm in the forward direction of the XZ plane. Compared to this nanosphere,

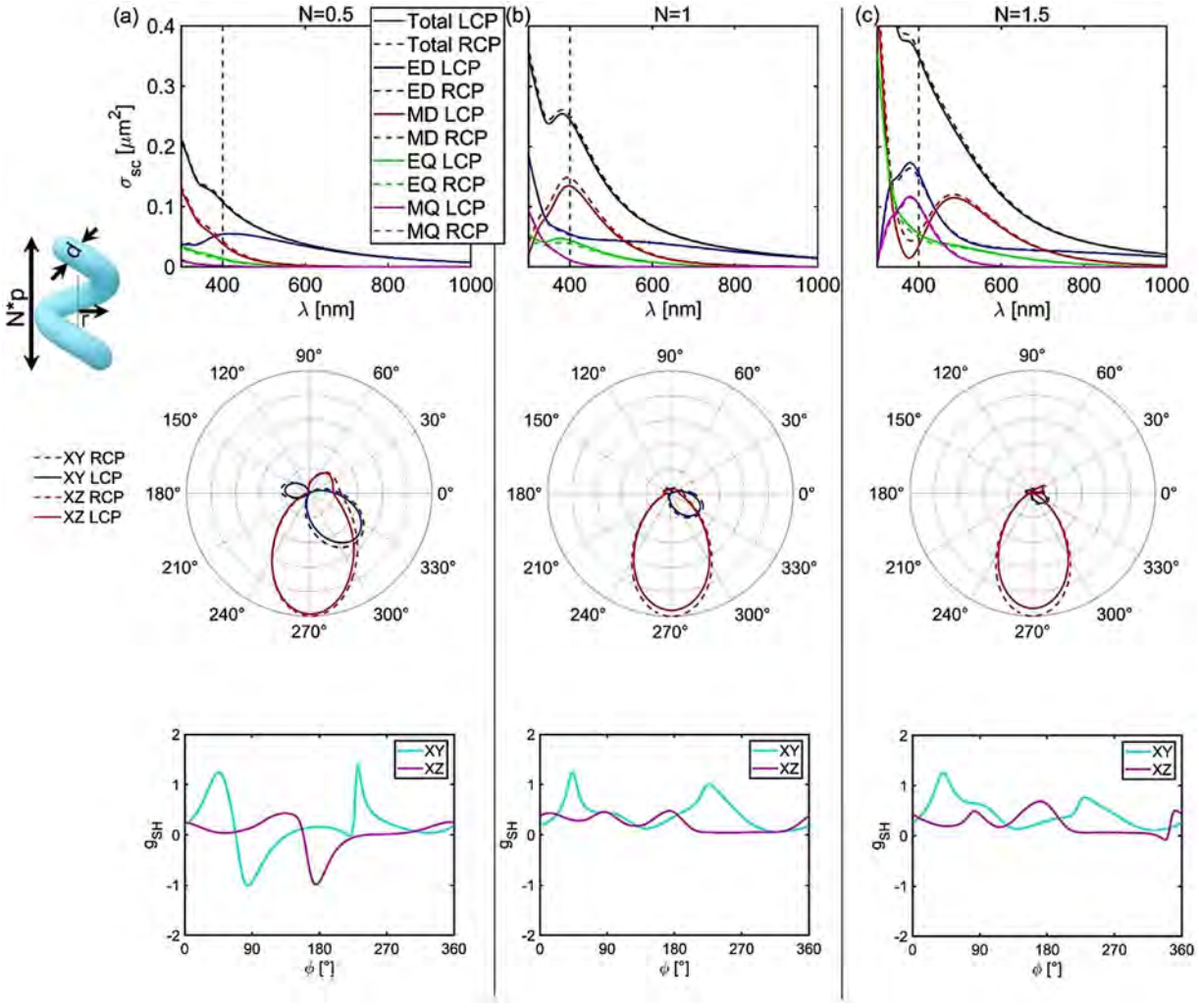

Figure 4. Multipole decomposition, second harmonic far-field distribution and nonlinear dissymmetry factor as a function of number of turns of a nanohelix. The inset shows the helix geometry, with linear and nonlinear results for (a) $N = 0.5$, (b) $N = 1$, and (c) $N = 1.5$. Geometric parameters of each helix are $p = 200$ nm, $d = 100$ nm, and $r = 50$ nm. All polar plots are normalized to the maximum forward scattering for RCP excitation.

nanospheres with $r = 90$ nm and $r = 70$ nm scatter 28% and 5% in the forward direction, respectively.

2.1 Influence of asymmetry

We next investigate how ellipsoid geometry influences radiated second harmonic fields. We define the ellipsoid with three radi ($r_{x,y,z}$), one of which is set to 200 nm, while the other two are set to 50 nm. The electric field is always linearly polarized in the x-direction, as in the inset of Figure 3. Figure 3a plots the ellipsoid oriented along x-direction ($r_x = 200$ nm); as expected, the strong ED governs the scattering. When electric field is polarized along shorter axis in the xy-plane, the multipolar analysis gives completely different response, with lower total scattering, Figure 3b. Finally, when long axis of the ellipsoid is parallel to the light propagation, ED and MQ have peaks close to 400 nm, Figure 3c. We next plot the XY and XZ second harmonic far-field distribution for the previous configurations, Figure 3d. x-oriented ellipsoid (long axis oriented in the x-direction) strongly emits in both XY and XZ directions; all polar plots are normalized to its maximum forward emission. y-oriented ellipsoid is the least efficient, while z-oriented ellipsoid has negligible backward scattering; these two ellipsoids have negligible lateral emission compared to the x-oriented one. In Figure 3e, we calculate the average XY and XZ emitted second harmonic for the three orientations. There is non-negligible backward and lateral scattering, but the overall far-field response is led by the behavior of the x-oriented ellipsoid. Understanding the contribution of each orientation to the total scattered field in both linear and nonlinear regime is important if elongated ZnO nanostructures are randomly dispersed in a solution [21].

2.2 Influence of chirality

Chirality is a fundamental property of our world; at the nanoscale, chiral objects differently interact with left and right circular polarizations (LCP and RCP, respectively). In nanostructured media, this property tailors linear

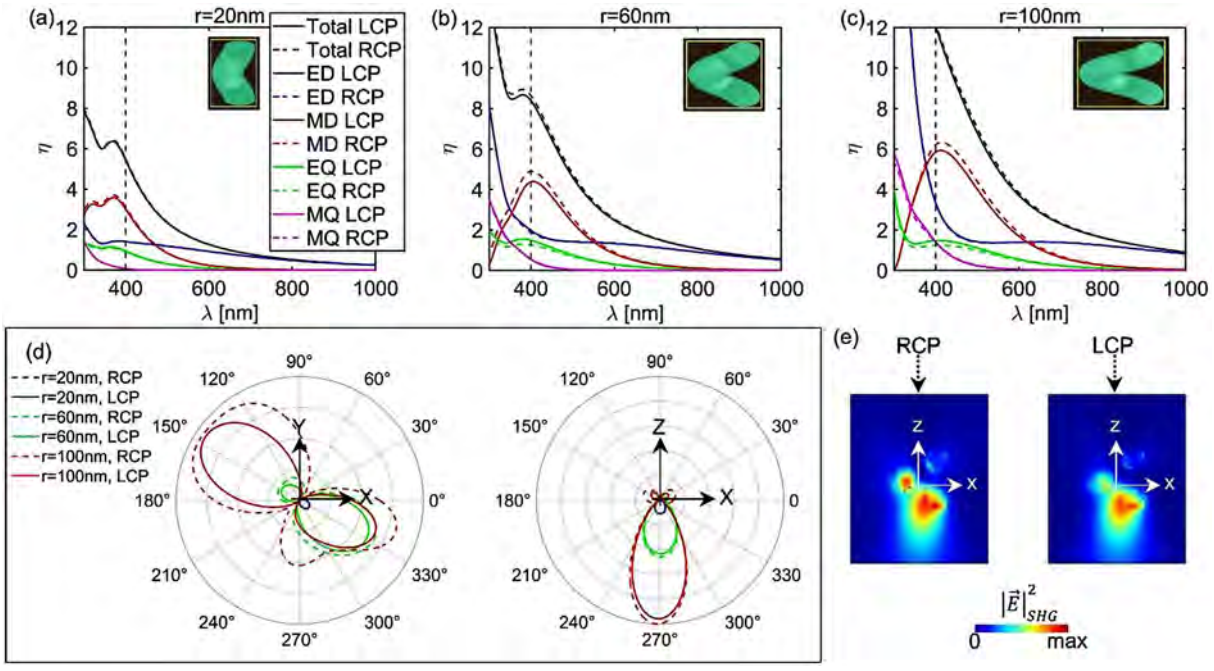

Figure 5. Multipole decomposition and second harmonic far-field distribution as a function of nanohelix loop radius; other geometric parameters of each helix are $p = 200$ nm, $d = 100$ nm, and $N = 1$, and multipole decomposition is done for (a) $r = 20$ nm, (b) $r = 60$ nm, and (c) $r = 100$ nm. (d) XY (left) and XZ (right) far-field distributions at 400 nm, for LCP and RCP excitations, and $r = 20$ nm (blue), $r = 60$ nm (green), and $r = 100$ nm (red). All polar plots are normalized to the maximum forward scattering for $r = 100$ nm and RCP excitation. (e) Electric field intensity at 400 nm in the xz-plane, when $r = 100$ nm nanohelix is excited from the top, at 800 nm, with RCP (left) and LCP (right).

[22–27] and nonlinear [28–30] optical response, leading to remarkable results towards applications in medicine and pharmaceuticals [31, 32]. We therefore investigate how transitioning to chiral shape changes the far-field distribution patter, and weather this pattern is able to "sense" chirality. We combine two TFSF sources so that they have polarizations perpendicular to each other, with a phase offset of $+90°$ or $-90°$, while having all the other properties equal; in the y-oriented source, $+90°$ ($-90°$) corresponds to RCP (LCP) incident polarization. A single helix is defined by material diameter d, helix pitch p, number of turns N, and loop radius r (calculated from the center to the middle of the material. We treat vertically aligned helix, important in many experimental configurations [33–35].

We first investigate how the number of turns influences lateral and forward scattering, Figure 4; constant geometric parameters are $p = 200$ nm, $r = 50$ nm, and $d = 100$ nm, and each polar plot is normalized to its own maximum forward scattering. When the helix does not have a complete turn, i.e. for $N = 0.5$, difference in the multipolar decomposition is extremely low between RCP and LCP excitations. MD emerges as the only mode with visible difference, and it is stronger for RCP excitation, Figure 4a. At 400 nm, this helix has strong lateral scattering, but, being the Kerker condition close to 400 nm, it has no backward scattering. For $N = 1$, in Figure 4b, difference for LCP and RCP excitation can be appreciated, especially for mode MD. Therefore, in polar plots at 400 nm, we observe difference in forward scattering, which is stronger for RCP excitation at 800 nm. As the number of turns increases, lateral scattering becomes negligible. Figure 4c shows that MD mode peak red shifts towards 500 nm for $N = 1.5$, but it still has different scattering efficiency between LCP and RCP at 400 nm. This mode then leads to observed chirality in the forward scattering at 400 nm. This is also confirmed by calculating the nonlinear scattered field dissymmetry factors at second harmonic: $g_{SH} = 2 \cdot (I_{RCP,SH} - I_{LCP,SH})/(I_{RCP,SH} + I_{LCP,SH})$, where $I_{RCP,SH}$ and $I_{LCP,SH}$ stand for scattered second harmonic intensity for RCP and LCP excitation, respectively; bottom panels of Figure 4 show g_{SH} as a function of polar angle φ.

We next investigate how the scattering efficiency depends on the loop radius, and how it influences radiation patterns at 400 nm. We keep the following parameters constant: $p = 200$ nm, $N = 1$, $d = 100$ nm, and we change the loop radius r. In Figure 4a–4c we plot the scattering efficiencies, as normalized to the geometric cross-section $(r + d/2)^2\pi$. For $r = 20$ nm, the nanostructure has the shape almost as a rod, and linear multipole decomposition gives extremely low chirality, Figure 5a. Widening the loop to $r = 60$ nm, MD mode peaks around 400 nm, and it has different scattering efficiency for RCP and LCP excitations, Figure 5b. This difference remains for $r = 100$ nm, with the overall scattering efficiency increase, Figure 5c. In Figure 5d we plot the radiation patterns at 400 nm, in XY plane (left) and XZ plane (right); we normalize all graphs to the maximum forward scattering for the most efficient helix, i.e. the one with $r = 100$ nm. Interestingly, this helix has many modes supported at 400 nm, and it provides strong laterally emitted second harmonic at this wavelength.

In all planes, all helices respond better to RCP incident polarization, and provide lateral scattering comparable to the forward scattering. Accordingly, near field generated around the helices depend on the excitation handedness, as shown in Figure 5e for $r = 100$ nm. Therefore, chirality tailors near fields and the far-field directivity at second harmonic wavelengths.

As nanohelices, too, are usually randomly oriented in a liquid, for a complete simulation of chirality, the orientational averaging must be performed, as experimentally shown in reference [36]; this procedure is the subject of future work. Apart from nanohelix geometry [37], a very recent work showed efficient linear chiral response in ZnO crystals synthesized using chiral methionine molecules as symmetry-breaking agents [38]: with chiral response peaking in the blue spectral range, chiral ZnO nanocrystals showed promise for improving surface reactions in photocatalysis. We believe it would be interesting to optimize geometries of such structures according to our simulations, and to measure their nonlinear response. Another interesting field are the cooperative effects in coupled nanostructures; i.e. chiral metamaterials were fabricated from different materials as vertically standing ensembles on substrates [22, 33]. In these cases, the total circular dichroism in the linear range was shown to reach remarkable values as there is no orientational averaging. Therefore, one could study how chirality at fundamental and second harmonic wavelengths tune the chirality at the emitted second harmonic. Moreover, chirality at the nanoscale can be treated even in achiral samples, where specific modes can lead to enhanced near-field chirality and so-called factor C [2, 39–42]. We predict that the discovered Kerker effect at the second harmonic wavelength can be further combined with the calculations of near-field chirality in solutions of chiral molecules coupled with achiral nanoparticles.

3 Conclusions

We have studied linear and nonlinear optical properties of nanostructures in water by means of FDTD simulations. Starting from the multipole decomposition in semiconductor nanospheres, we have introduced the nonlinear susceptibility. We then excited the nanostructures with strong electric field at 800 nm, and studied near- and far-field distributions emitted at second harmonic wavelength. For ZnO as a test material, nanosphere that supports the first Kerker condition around 400 nm leads to negligible backward scattering of the second harmonic. We further introduced asymmetry and chirality in the nanostructure geometry, and monitored its influence and the second harmonic far-field directivity and dependence on the polarization. We believe that our numerical approach could be a valuable tool for prediction and tailoring of far-field radiation pattern in nonlinear nanophotonics.

Acknowledgments

The authors thank the ENSEMBLE3 Project carried within the Teaming for Excellence Horizon 2020 program of the European Commission (GA No. 857543), and the International Research Agendas Program (MAB/2020/14) of the Foundation for Polish Science co-financed by the European Union under the European Regional Development Fund and Teaming Horizon 2020 program of the European Commission.

Funding

This research received no external funding.

Conflicts of Interest

The authors declare no conflict of interest.

Data availability statement

Data obtained in this work are not publicly available at this time but may be obtained from the authors upon reasonable request.

Author contribution statement

Conceptualization, E.P.; methodology, E.P. and C.S.; software, E.P. and C.S.; validation, writing – original draft preparation, E.P.; writing – review and editing, C.S.

References

1 Xu J., Wu Y., Zhang P., Wu Y., Vallée R.A.L., Wu S., Liu X. (2021) Resonant scattering manipulation of dielectric nanoparticles, *Adv. Opt. Mater.* **9**, 2100112.
2 Solomon M.L., Abendroth J.M., Poulikakos L.V., Hu J., Dionne J.A. (2020) Fluorescence-detected circular dichroism of a chiral molecular monolayer with dielectric metasurfaces, *J. Am. Chem. Soc.* **142**, 43, 18304–18309.
3 Kalinic B., Cesca T., Balasa I.G., Trevisani M., Jacassi A., Maier S. A., Sapienza R., Mattei G. (2023) Quasi-BIC modes in all-dielectric slotted nanoantennas for enhanced Er^{3+} emission, *ACS Photonics* **10**, 2, 534–543.
4 Shcherbakov M.R., Vabishchevich P.P., Shorokhov A.S., Chong K.E., Choi D., Staude I., Miroshnichenko A.E., Neshev D.N., Fedyanin A.A., Kivshar Y.S. (2015) Ultrafast all-optical switching with magnetic resonances in nonlinear dielectric nanostructures, *Nano Lett.* **15**, 6985–6990.
5 Carletti L., Locatelli A., Neshev D., De Angelis C. (2016) Shaping the radiation pattern of second-harmonic generation from algaas dielectric nanoantennas, *ACS Photonics* **3**, 8, 1500–1507.
6 Bahng J.H., Jahani S., Montjoy D.G., Yao T., Kotov N., Marandi A. (2020) Mie resonance engineering in meta-shell supraparticles for nanoscale nonlinear optics, *ACS Nano* **14**, 17203–17212.
7 Carletti L., Zilli A., Moia F., Toma A., Finazzi M., De Angelis C., Neshev D.N., Celebrano M. (2021) Steering and encoding the polarization of the second harmonic in the visible with a monolithic $LiNbO_3$ metasurface, *ACS Photonics* **8**, 731–737.
8 Lai Y.-Y., Lan Y.-P., Lu T.-C. (2013) Strong light–matter interaction in ZnO microcavities, *Light Sci. Appl.* **2**, e76.
9 Li H., Tang J., Lin F., Wang D., Fang D., Fang X., Liu W., Chen R., Wei Z. (2019) Improved optical property and lasing of ZnO nanowires by Ar plasma treatment, *Nanoscale Res. Lett.* **14**, 312.
10 Larciprete M.C., Centini M. (2015) Second harmonic generation from ZnO films and nanostructures, *Appl. Phys. Rev.* **2**, 031302.
11 Petronijevic E., Tomczyk M., Belardini A., Osewski P., Piotrowski P., Centini M., Leahu G., Li Voti R., Pawlak D.A., Sibilia C., Larciprete M.C. (2022) Surprising eutectics: enhanced properties of ZnO–$ZnWO_4$ from visible to MIR, *Adv. Mater.* **35**, 34, 2206005.
12 van Embden J., Gross S., Kittilstved K.R., Della Gaspera E. (2023) Colloidal approaches to zinc oxide nanocrystals, *Chem. Rev.* **123**, 1, 271–326.
13 Lumerical Solutions, Inc. Available at: http://www.lumerical.com/tcadproducts/fdtd/.
14 Aguilar O., de Castro S., Godoy M.P.F., Dias M.R.S. (2019) Optoelectronic characterization of $Zn_{1-x}Cd_xO$ thin films as an alternative to photonic crystals in organic solar cells, *Opt. Mater. Express* **9**, 3638–3648.

15 Hinamoto T., Fujii M. (2021) MENP: An open-source MATLAB implementation of multipole expansion for nanophotonics, *OSA Contin.* **4**, 5, 1640–1648.

16 Luk'yanchuk B.S., Voshchinnikov N.V., Paniagua-Domínguez R., Kuznetsov A.I. (2015) Optimum forward light scattering by spherical and spheroidal dielectric nanoparticles with high refractive index, *ACS Photonics* **2**, 7, 993–999.

17 Lamastra F.R., Grilli M.L., Leahu G., Belardini A., Li Voti R., Sibilia C., Salvatori D., Cacciotti I., Nanni F. (2017) Diatom frustules decorated with zinc oxide nanoparticles for enhanced optical properties, *Nanotechnology* **28**, 375704.

18 Lamastra F.R., Grilli M.L., Leahu G., Belardini A., Li Voti R., Sibilia C., Salvatori D., Cacciotti I., Nanni F. (2018) Photoacoustic spectroscopy investigation of zinc oxide/diatom frustules hybrid powders, *Int. J. Thermophys.* **39**, 110.

19 Osewski P., Belardini A., Petronijevic E., Centini M., Leahu G., Diduszko R., Pawlak D.A., Sibilia C. (2017) Self-phase-matched second-harmonic and white-light generation in a biaxial zinc tungstate single crystal, *Sci. Rep.* **7**, 45247.

20 Das S.K., Bock M., O'Neill C., Grunwald R., Lee K.M., Lee H.W., Lee S., Rotermund F. (2008) Efficient second harmonic generation in ZnO nanorod arrays with broadband ultrashort pulses, *Appl. Phys. Lett.* **93**, 181112.

21 Lee W., Yeop J., Heo J., Jin Yoon Y., Yi Park S., Jeong J., Seop Shin Y., Won Kim J., Gyeong An N., Suk Kim D., Park J., Young Kim J. (2020) High colloidal stability ZnO nanoparticles independent on solvent polarity and their application in polymer solar cells, *Sci. Rep.* **10**, 18055.

22 Kilic U., Hilfiker M., Ruder A., Feder R., Schubert E., Schubert M., Argyropoulos C. (2021) Broadband enhanced chirality with tunable response in hybrid plasmonic helical metamaterials, *Adv. Funct. Mater.* **31**, 2010329.

23 González-Rubio G., Mosquera J., Kumar V., Pedrazo-Tardajos A., Llombart P., Solís D.M., Lobato I., Noya E.G., Guerrero-Martínez A., Taboada J.M., Obelleiro F., MacDowell L.G., Bals S., Liz-Marzán L.M. (2020) Micelle-directed chiral seeded growth on anisotropic gold nanocrystals, *Science* **368**, 1472–1477.

24 Zhuo X., Mychinko M., Heyvaert W., Larios D., Obelleiro-Liz M., Taboada J.M., Bals S., Liz-Marzán L.M. (2022) Morphological and optical transitions during micelle-seeded chiral growth on gold nanorods, *ACS Nano* **16**, 19281–19292.

25 Leahu G., Petronijevic E., Li Voti R., Belardini A., Cesca T., Mattei G., Sibilia C. (2021) Diffracted beams from metasurfaces: high chiral detectivity by photothermal deflection technique, *Adv. Opt. Mater.* **9**, 21, 2100670.

26 Petronijevic E., Belardini A., Cesca T., Scian C., Mattei G., Sibilia C. (2021) Rich near-infrared chiral behavior in diffractive metasurfaces, *Phys. Rev. Appl.* **16**, 1, 014003.

27 Ali H., Petronijevic E., Pellegrini G., Sibilia C., Andreani L.C. (2023) Circular dichroism in a plasmonic array of elliptical nanoholes with square lattice, *Opt. Express* **31**, 9, 14196–14211.

28 Collins J.T., Rusimova K.R., Hooper D.C., Jeong H.-H., Ohnoutek L., Pradeux-Caggiano F., Verbiest T., Carberry D.R., Fisher P., Valev V.K. (2019) First observation of optical activity in hyper-Rayleigh scattering, *Phys. Rev. X* **9**, 1, 011024.

29 Ohnoutek L., Kim J.-Y., Lu J., Olohan B.J., Răsădean D.M., Pantoş G.D., Kotov N.A., Valev V.K. (2022) Third harmonic hyper-mie scattering from semiconductor nanohelices, *Nat. Photon.* **16**, 126–133.

30 Ohnoutek L., Jeong H.-H., Jones R.R., Sachs J., Olohan B.J., Răsădean D.M., Pantoş G.D., Andrews D.L., Valev V.K. (2021) Optical activity in third-harmonic Rayleigh scattering: a new route for measuring chirality, *Laser Photonic Rev.* **15**, 11, 2100235.

31 Hou K., Zhao J., Wang H., Li B., Li K., Shi X., Wan K., Ai J., Lv J., Wang D., Huang Q., Wang H., Cao Q., Liu S., Tang Z. (2020) Chiral gold nanoparticles enantioselectively rescue memory deficits in a mouse model of Alzheimer's disease, *Nat. Commun.* **11**, 4790.

32 Xu L., Wang X., Wang W., Sun M., Choi W.J., Kim J.Y., Hao C., Li S., Qu A., Lu M., Wu X. (2022) Enantiomer-dependent immunological response to chiral nanoparticles, *Nature* **601**, 366–373.

33 Passaseo A., Esposito M., Cuscunà M., Tasco V. (2017) Materials and 3D designs of helix nanostructures for chirality at optical frequencies, *Adv. Opt. Mater.* **5**, 1601079.

34 Petronijevic E., Belardini A., Leahu G., Li Voti R., Sibilia C. (2022) Nanostructured materials for circular dichroism and chirality at the nanoscale: towards unconventional characterization [Invited], *Opt. Mater. Express* **12**, 7, 2426–2937.

35 Jones R.R., Miksch C., Kwon H., Pothoven C., Rusimova K.R., Kamp M., Gong K., Zhang L., Batten T., Smith B., Silhanek A.V., Fischer P., Wolverson D., Valev V.K. (2023) Dense arrays of nanohelices: Raman scattering from achiral molecules reveals the near-field enhancements at chiral metasurfaces, *Adv. Mater.* **35**, 2209282.

36 Sachs J., Günther J., Mark A.G., Fischer P. (2020) Chiroptical spectroscopy of a freely diffusing single nanoparticle, *Nat. Commun.* **11**, 4513.

37 Gao P.X., Ding Y., Mai W., Hughes W.L., Lao C., Wang Z.L. (2005) Conversion of zinc oxide nanobelts into superlattice-structured nanohelices, *Science* **309**, 5741.

38 Ai M., Pan L., Shi C., Huang Z.-F., Zhang X., Mi W., Zou J.-J. (2023) Spin selection in atomic-level chiral metal oxide for photocatalysis, *Nat. Commun.* **14**, 4562.

39 Petronijevic E., Sibilia C. (2019) Enhanced near-field chirality in periodic arrays of Si nanowires for chiral sensing, *Molecules* **24**, 5, 853.

40 Petronijevic E., Sandoval E.M., Ramezani M., Ordóñez-Romero C. L., Noguez C., Bovino F.A., Sibilia C., Pirruccio G. (2019) Extended chiro-optical near-field response of achiral plasmonic lattices, *J. Phys. Chem. C* **123**, 38, 23620–23627.

41 Ye L., Li J., Richter F.U., Jahani Y., Lu R., Lee B.R., Tseng M.L., Altug H. (2023) Dielectric tetramer nanoresonators supporting strong superchiral fields for vibrational circular dichroism spectroscopy, *ACS Photonics* **10**, 12, 4377–4384.

42 Goerlitzer E.S.A., Zapata-Herrera M., Ponomareva E., Feller D., Garcia-Etxarri A., Karg M., Aizpurua J., Vogel N. (2023) Molecular-induced chirality transfer to plasmonic lattice modes, *ACS Photonics* **10**, 6, 1821–1831.

J. Eur. Opt. Society-Rapid Publ. 2024, **20**, 12

https://doi.org/10.1051/jeos/2024011
Available online at: https://jeos.edpsciences.org

Special Issue - Plasmonica 2023
Antonino Foti and Attilio Zilli (Guest editors)

Journal of the European Optical Society-Rapid Publications

RESEARCH ARTICLE

OPEN ACCESS

Towards the epitaxial growth of Au thin films on MgO substrates for plasmonic applications

Michele Celebrano[1], Matteo Savoini[2], Paolo Biagioni[1], Giuseppe Della Valle[1], Giovanni Pellegrini[3], Matteo Cantoni[1], Christian Rinaldi[1], Andrea Cattoni[1], Daniela Petti[1], Riccardo Bertacco[1], Lamberto Duò[1], and Marco Finazzi[1,*]

[1] Dipartimento di Fisica, Politecnico di Milano, Piazza Leonardo da Vinci 32, 20133, Milano, Italy
[2] Institute for Quantum Electronics, ETH Zürich, 8093, Zürich, Switzerland
[3] Department of Physics, University of Pavia, via Bassi 6, 27100, Pavia, Italy

Received 31 January 2024 / Accepted 16 March 2024

Abstract. Surface Plasmon Polaritons (SPPs) in Au thin films are nowadays intensively exploited for sensing applications that leverage the strong optical field confinement at the metal/dielectric interface and the easy functionalization of the Au surface. Moreover, Au thin films represent one of the common starting points for the top-down nanofabrication of plasmonic nanostructures supporting localized resonances. In this framework, strategies for the growth of high-quality Au films on transparent substrates are crucial and not yet fully established. In this study, we exploit MgO(001) substrates for the growth of thin (about 45 nm) Au films, also including an additional buffer layer of Fe. We successfully demonstrate Au samples with reduced roughness and presenting Low-Energy Electron Diffraction (LEED) features, indicating a high degree of crystalline ordering. This is supported by the experimental evidence of an increased (by almost a factor of 3) propagation length compared to a reference Au sample grown on standard glass slides, which is however still significantly lower than the one expected from first principles.

Keywords: Surface plasmon polaritons, Gold, Single crystals.

1 Introduction

Plasmonics investigates the properties of Surface Plasmon Polaritons (SPPs) [1, 2], which are coherent collective electron oscillations travelling together with an electromagnetic wave along the interface between a metal (e.g., Au, Ag) and a dielectric (e.g., glass, air). These surface plasmons can give rise to a wide array of remarkable optical phenomena, such as subwavelength confinement of light and enhanced light-matter interactions, offering the possibility to manipulate electromagnetic fields at the nanoscale. More specifically, by an appropriate choice of geometry and materials, one can tune the plasmonic resonances of nanostructures, enabling the possibility to engineer systems with tailored optical behaviors. These resonances, which can manifest either as surface plasmon resonances at extended metal/dielectric interfaces or as localized plasmon resonances in nanostructures, have found extensive application in a diverse range of fields, including sensing, imaging, energy harvesting, nanophotonics, and data communication [3–5].

Relevant parameters that ultimately define the performance of plasmonic assets consist in field enhancement, spectral selectivity, and SPP propagation length, which are in turn strongly affected by losses [2, 6]. The plasmon energy is in fact lost through different mechanisms, such as absorption, scattering by defects, and radiation leakage, the latter also present in smooth single-crystalline films. Understanding and managing these losses is pivotal in harnessing the full potential of plasmonic technologies.

At planar metal/dielectric interfaces, propagation of SPPs is characterized by a propagation length Λ, which, for a flat and thick film, is mainly determined by Ohmic losses in the metal. Other losses can be due to scattering from surface roughness, grain boundaries, and defects [7, 8]. A further channel is present only for thin films, namely radiation leakage at a second metal/dielectric interface [2, 9].

The propagation length of plasmon polaritons has been characterized on both polycrystalline [10] and single-crystal [10, 11] Au surfaces. In single crystalline thick gold flakes, the SPP propagation length Λ has been found to be as long as about 100 μm for an SPP energy of 1.55 eV and to rapidly decrease to about 1 μm at 2.33 eV, as a consequence

* Corresponding author: marco.finazzi@polimi.it

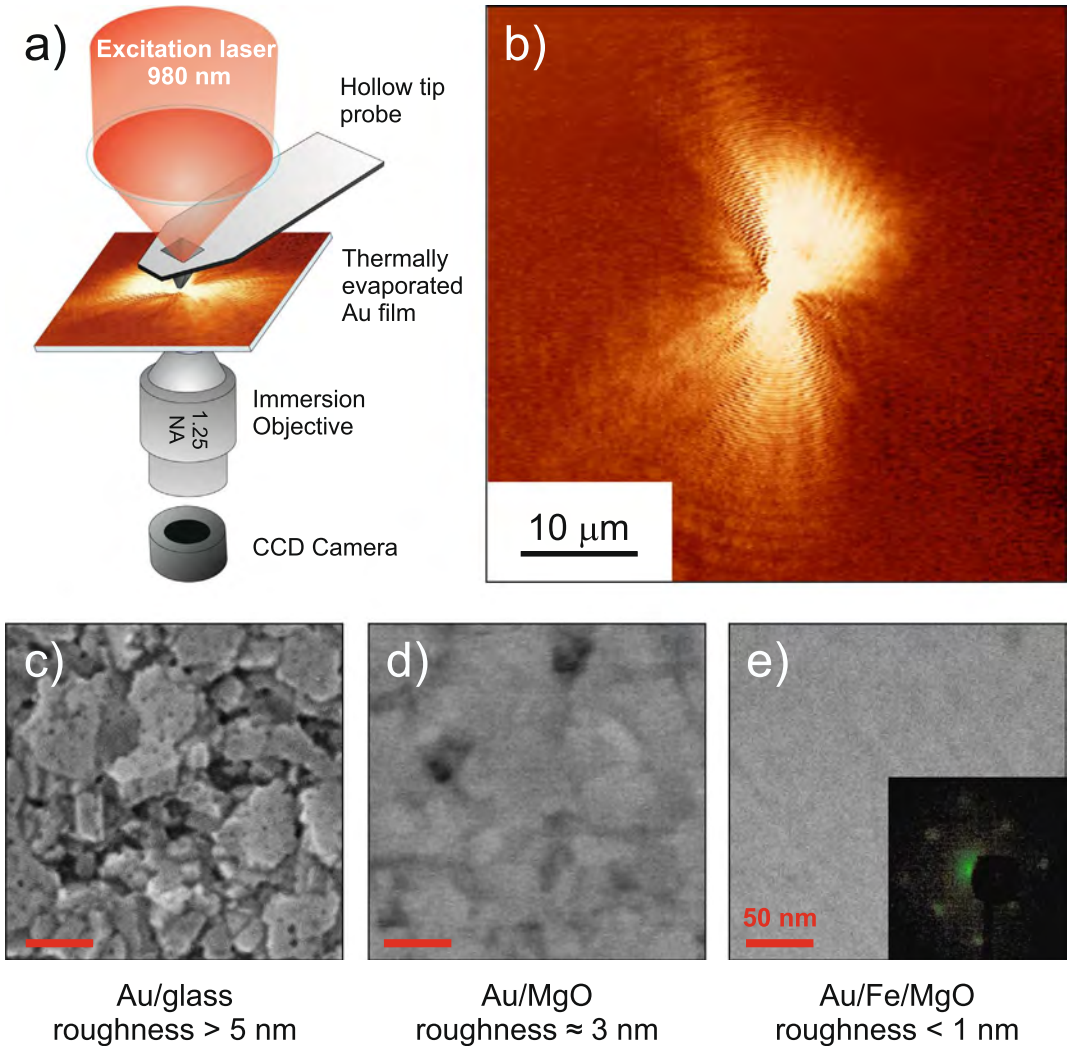

Fig. 1. a) Experimental setup: an SPP wave is launched by a hollow tip for near-field scanning optical microscopy in contact with the gold film. SPP propagation is imaged by collecting the light leaked into the substrate with a CCD camera placed in the focal plane of an oil immersion microscope objective (numerical aperture NA = 1.25). b) Example of an image collected by our experimental setup on the Au/Fe/MgO(001) sample. c–e) Scanning electron microscope images collected on Au/glass, Au/MgO(001), Au/Fe/MgO(001), respectively. Inset: LEED pattern collected on the Au/Fe/MgO(001) sample.

of the rapid increase in the Au resistivity with increasing SPP frequency [11]. The propagation length is found to be strongly damped in polycrystalline samples because of the scattering losses due to the surface roughness and crystal grain boundaries [10]. In practice, so far, single-crystal Au has been mainly studied in bulk (mm-thick) samples [10] and in chemically grown flakes [11], with the relevant exception of the demonstration of high-quality epitaxial thin films on mica substrates [12], which however suffer from a strong birefringence. Another advantage of single crystal Au films consists in the precise control over nanopatterning processes such as electron beam lithography or nanoimprint lithography, enabling the fabrication of high-definition ultrasmooth gold nanostructures with superior optical properties and reproducible nano-sized features over micrometre-length scales [13, 14].

2 Sample preparation and experimental setup

In this work we investigate a possible route to achieve high-quality (possibly single-crystalline) Au thin films by standard Molecular Beam Epitaxy (MBE) on transparent substrates and we experimentally probe the propagation length of SPPs in films characterized by different crystalline and morphological qualities. Surface plasmons are launched by retro-illuminating a hollow tip for near-field scanning optical microscopy in contact with the gold film, similarly to what reported in reference [15]. In this way, SPPs are excited thanks to the large wavevectors associated with the tail of the evanescent field emerging from the subwavelength aperture (diameter ≈ 100 nm). SPP propagation is then imaged at room temperature onto a CCD camera by collecting the light leaked into the transparent substrate

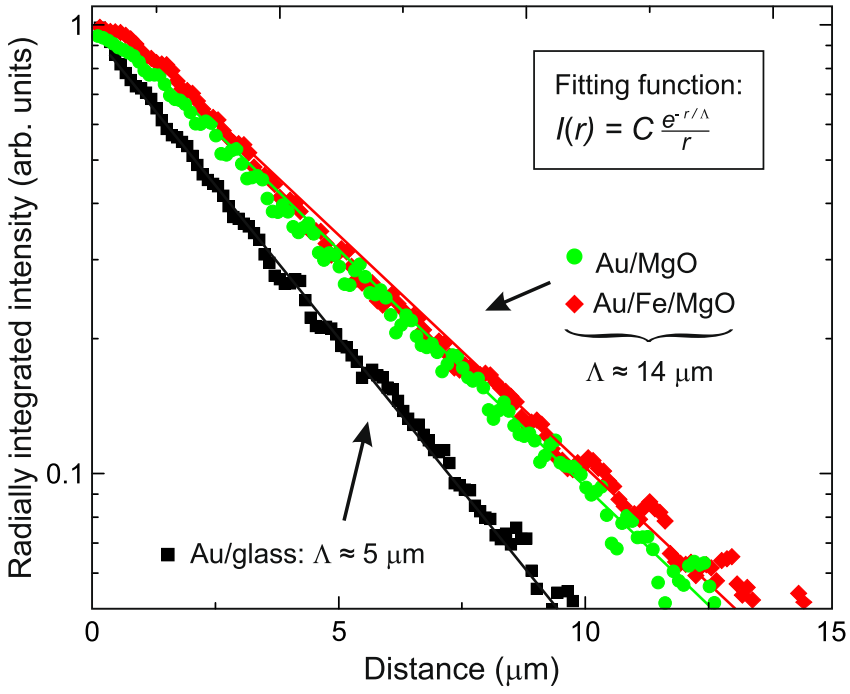

Fig. 2. Normalized radially integrated intensity of the light irradiated by the SPP wave as a function of the distance r from the tip apex. The values of the propagation length Λ obtained by interpolating the data with the function $I(r) = Ce^{-r/\Lambda}$ are reported for all the three investigated samples. The wavelength of light illuminating the tip is $\lambda = 980$ nm, corresponding to a plasmon energy of 1.26 eV.

with an oil immersion microscope objective, characterized by a numerical aperture equal to 1.25 (see Fig. 1a). A typical image measured by the camera is shown in Figure 1b. Extended lobes are seen to protrude from the central position where the tip is located and are visible only when the tip is in contact or next to contact with the Au film. Such lobes are characteristic of a two-dimensional dipole radiation pattern aligned with the linear polarization of the light illuminating the tip aperture [15]. Their shape is however uneven, which we attribute to the irregularities of the contact area between the rim of the tip aperture and the gold film. The concentric rings that can be viewed in Figure 1b are attributed to interference between the radiation leaked from the SPP wave and the light coming directly from the tip aperture, which is a common observation when near-field microscopy is used to image evanescent waves [16].

Gold films with a thickness of 45 ± 5 nm were deposited by MBE onto different substrates by evaporating pure (99.99%) gold pellets by using a Knudsen cell (base pressure during deposition lower than 10^{-9} mbar). The selected substrates were either fused-silica cover-slips or MgO(001) single crystals, the latter characterized by large (hundreds of nanometers wide) atomically-flat terraces. All substrates have been previously cleaned by sonication in isopropanol and then in deionized water. The deposition on MgO(001) crystals was always performed after the homoepitaxial growth of 10 nm of MgO at room temperature, with a rate of about 0.1 nm/min, followed by an annealing at 300 °C for 20 min, in order to create the best surface conditions for the following steps. Au was then either grown directly on MgO or after the evaporation of a 10 nm-thick Fe buffer at a rate of about 0.2 nm/min with the substrate kept at room temperature. The sample was then annealed at 500 °C for 20 min and subsequently flashed at 620 °C [17]. No post-growth annealing was performed on the Au/glass sample since it is well-known that a high-temperature annealing promotes the enucleation of islands, being the surface tension of silica much smaller than the one of the Au film ($\gamma_{\text{silica}} \approx 260$ erg/cm^2 *vs.* $\gamma_{\text{Au}} \approx 750$ erg/cm^2). Au films were deposited with very slow rates (0.1 and 0.5 nm/min) to favour a layer-by-layer growth. Because both rates gave the same structural quality, as checked by Low-Energy Electron Diffraction (LEED) (see Sect. 3), we eventually choose to deposit Au at the faster rate (0.5 nm/min) to reduce the deposition time and, consequently, film contamination (*in-situ* X-ray Photoemission Spectroscopy showed C and O contents below the detection limit). The substrate temperature was chosen to be 120 ± 5 °C because lower temperatures did not show any visible LEED pattern. In the case of the Au/MgO sample, a post-growth annealing at 320 °C for 20 min was performed to improve the film quality, while for the Au/Fe/MgO heterostructure, a post annealing showed no effect. While in the first case (Au/MgO) the quality of the Au film is known to be characterized by the facile nucleation of Au nanoparticles [18] and to be highly sensitive to the carbon content of the substrate [19], the use of an intermediate Fe buffer layer in the Au/Fe/MgO sample has been already shown to improve the crystal quality of the film [20]. A smeared low energy electron diffraction pattern

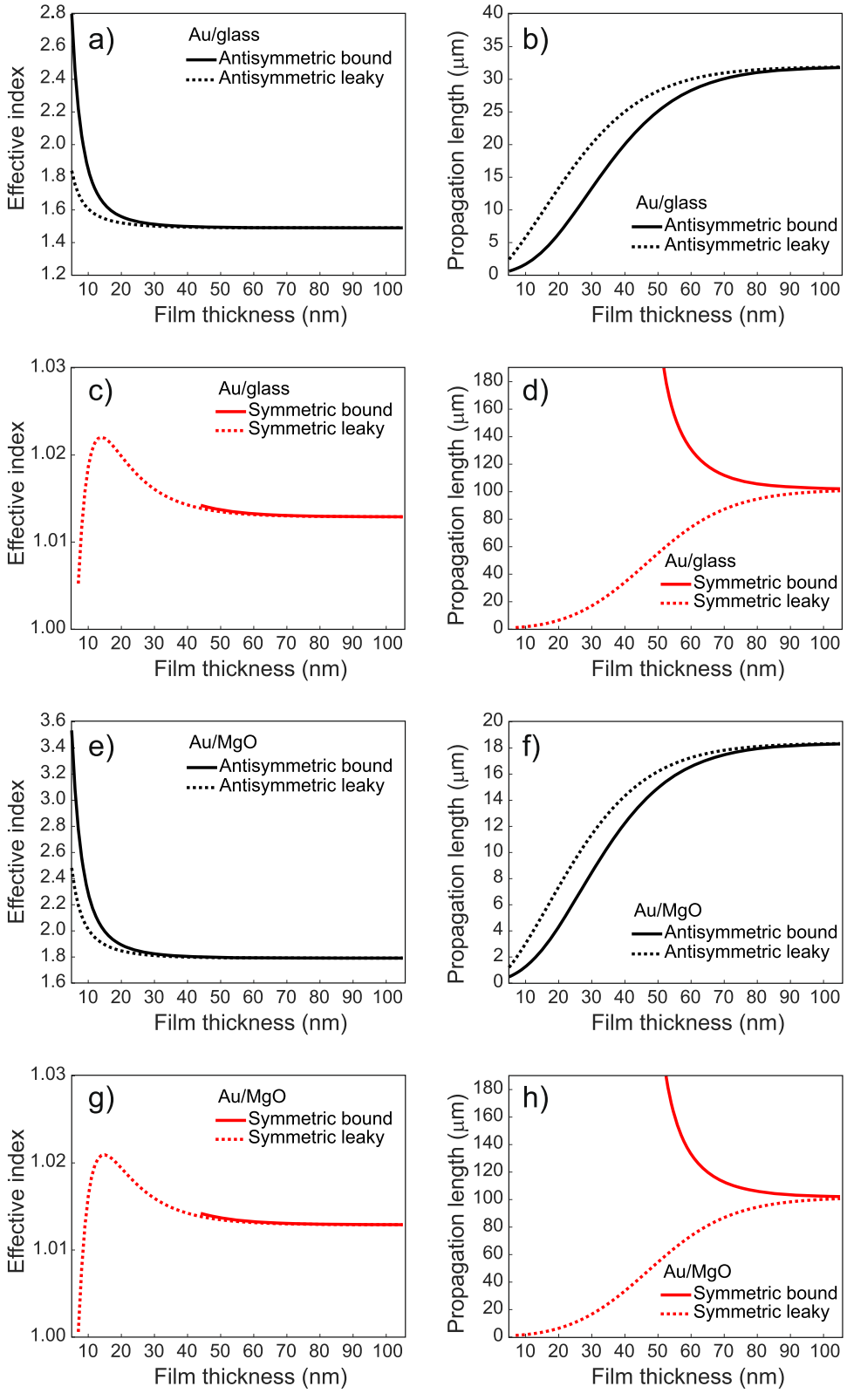

Fig. 3. Analytical results, following reference [6], for the effective index (i.e., the ratio between the free-space and the SPP wavelengths) and the propagation length ($1/e$ attenuation of the SPP intensity) of SPPs propagating in Au thin films on glass (panels a–d) or MgO (e–h). Red lines represent symmetric-like modes, black lines represent antisymmetric-like modes, solid lines refer to bound modes, dotted lines refer to leaky modes.

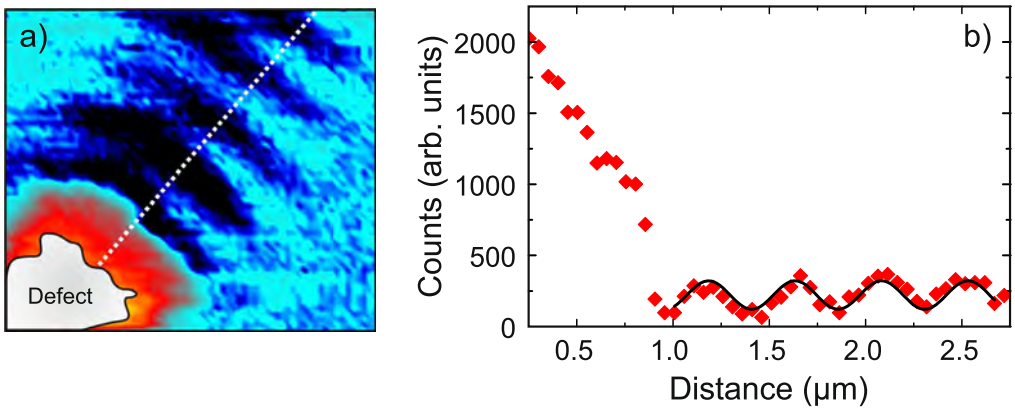

Fig. 4. a) Light collected by the CCD camera showing a stationary wave produced by the interference between the SPP wave excited by the tip (located above the top right corner of the image) and the one back reflected by a large defect on the surface of the Au/Fe/MgO(001) sample. b) Intensity profile (dots) and sinusoidal fitting (line) along the dashed line shown in panel a. From the period of the stationary wave, we obtain that a SPP with wavelength $\lambda_{SPP} = 896 \pm 1.5$ nm is excited by light impinging on the tip with $\lambda_{exc} = 880$ nm.

superimposed on an intense diffused background (see inset in Fig. 1e) is visible for Au/Fe/MgO, after a subsequent post-growth annealing at 390 °C, demonstrating that the insertion of the Fe buffer is indeed effective in improving the crystal quality of the gold layer. A smooth LEED pattern, with a very small contrast compared to the background, was also noticed on a Au/MgO sample with Au thickness of 10 nm. This denotes even in that case some trace of crystal order, which disappears at larger thicknesses. We are not in the position to assess whether such a post-growth annealing also determined interdiffusion between the Fe and the Au layers.

Scanning electron microscope images collected from the three samples are reported in Figures 1c–1e, which show the different morphology of the films. The root-mean square surface roughness was also characterized by atomic-force microscopy to be more than 5 nm, about 3 nm, and less than 1 nm for the Au/glass, Au/MgO, and Au/Fe/MgO samples, respectively.

3 Results and discussion

The normalized radially integrated intensity $I(r)$ of the light radiated by the SPP wave and collected by the camera is shown in Figure 2 for the three investigated samples as a function of the distance r from the tip apex. The three curves can be fitted with an exponential function of the form $I(r) = Ce^{-r/\Lambda}$, where C is a normalization constant and Λ is the SPP propagation length. The wavelength of the light illuminating the tip is $\lambda = 980$ nm, corresponding to a plasmon energy of 1.26 eV. As one can immediately notice, improving the morphology of the Au layer from Au/glass to both Au/MgO(001) and Au/Fe/MgO(001) results in a larger SPP propagation length. However, the additional improvement in the crystalline quality of the Au film achieved through the incorporation of the Fe buffer does not lead to an enhancement in the propagation length.

The value of Λ measured in our thin films is considerably smaller than the one reported for thick Au single crystals, which is about 100 μm for SPP waves excited by light with wavelength $\lambda = 800$ nm (plasmon energy = 1.55 eV) [11]. This observation may not come as a surprise, considering that a smaller propagation length for our samples is to be expected because of the larger radiation losses. As already discussed in the literature [9], the dispersion relations for waves guided by thin, lossy metal films on a substrate include two radiative (leaky) and two nonradiative (bound) modes. The solutions to the analytical problem for the Au/glass and Au/MgO systems can be computed numerically to extract the expected effective index and propagation length following reference [9], as plotted in Figure 3 (Au/Fe/MgO is not shown since the plasmon propagation length estimated for sample is not significantly affected by the extra Ohmic losses, which are negligible with respect to those due to radiation leakage). Leaky and bound modes can be further classified based on their symmetric-like or antisymmetric-like character, which is reminiscent of the symmetric (long-range) and antisymmetric (short-range) SPPs supported by a thin Au film in a symmetric environment [2].

With our experimental configuration, we expect to observe the radiation and decay of the symmetric leaky mode (dashed red lines in Fig. 3), which radiates into the substrates and is characterized by an effective index very close to 1 (see Figs 3c and 3g). On the contrary, the bound modes are not coupled with far field radiation propagating into the substrate and cannot be detected in our experimental configuration The predicted propagation lengths for such mode on 45-nm-thick Au layers is of the order of 40 μm (see Figs. 3d and 3h) and are very similar for the two considered substrates, meaning that the different propagation lengths that we observe in Figure 2 cannot be attributed to the refractive index of the substrates but are rather due to the different surface roughness and/or crystalline quality. To experimentally confirm that this is indeed

the mode we are observing, we look for a sample position in which a surface defect determines the occurrence of an SPP standing wave, as already done in the literature [15]. Figure 4a shows the stationary wave observed when the tip is positioned close to a large defect on top of the Au surface of the Au/Fe/MgO(001) sample. The stationary wave is produced by the interference between the SPP coming from the tip (which is located outside the image, above the top right corner) and the one reflected back by the defect. The half wavelength of the excited SPP can be determined by measuring the period of the stationary wave. We find an SPP wavelength that is about 1% larger than the free-space wavelength of the excitation laser (Fig. 4b). This corresponds to an effective refractive index of 0.98 ± 0.03, thus confirming that, within the error bars for the calibration of our imaging system, we are indeed observing the symmetric leaky mode, which is characterized by an effective refractive index of about 1.015 for a 40 nm-thick Au film. Note form Figures 4a and 4c that the effective indices of the antisymmetric modes are larger than 1.5, therefore the mode can be assigned without ambiguity.

4 Conclusion

In conclusion, we have investigated the propagation length of SPPs propagating at the air/Au interface of thin gold layers deposited onto different substrates and characterized by different morphological and crystalline qualities. The propagation length measured for Au thin films grown on MgO is almost three times larger compared to that of Au film grown on glass. Nevertheless, while we observed an augmented propagation length for samples with better quality, the propagation length reaches a maximum value notably lower (by almost a factor of 3) than the one anticipated by first principle calculations. It should be noticed that for such calculations we have used refractive index data from reference [21], which refers to a polycrystalline Au sample grown on glass that should represent a more disadvantageous situation compared to our high-quality films, both in terms of surface roughness and grain boundaries. It is also worth noting that the absence of any further improvement in the propagation length for the Au/Fe/MgO sample, despite the improved crystallinity, can hardly be attributed to the presence of the Fe layer, which is not predicted to increase the overall Ohmic losses for the symmetric leaky mode in the investigated wavelength range. The quantitative interpretation of our data, therefore, partially remains an open point that confirms the general difficulty in growing high-quality Au films for plasmonic applications and deserves further future investigations to proceed along the route opened by our approach.

Acknowledgments

The authors would like to thank Bert Hecht for insightful discussion.

Funding

This work was supported by Ministero dell'Università e della Ricerca (2017 MP7F8F, PRIN NOMEN).

Conflict of Interests

The authors declare that they have no competing interests to report.

Author contribution statement

Finazzi conceived the experiment. Celebrano and Savoini performed the experiments and analyzed the data. Biagioni, Della Valle and Pellegrini performed the numerical simulations. Cantoni, Rinaldi, Cantoni, Petti e Bertacco realized the samples, Duò coordinated the team.

Data availability statement

The data associated with this study is available upon request. Please contact the corresponding author to request access to the data.

References

1 Maier S.A., Brongersma M.L., Kik P.G., Meltzer S., Requicha A.A.G., Atwater H.A. (2001) Plasmonics – a route to nanoscale optical devices, *Adv. Mater.* **13**, 1501–1505.
2 Maier S.A. (2007) *Plasmonics: fundamentals and applications*, Springer, New York, NY.
3 Lal S., Link S., Halas N.J. (2007) Nano-optics from sensing to waveguiding, *Nat. Photonics* **1**, 641–648.
4 Anker J.N., Hall W.P., Lyandres O., Shah N.C., Zhao J., Van Duyne R.P. (2008) Biosensing with plasmonic nanosensors, *Nat. Mater.* **7**, 442–453.
5 Schuller J.A., Barnard E.S., Cai W., Chul Jun Y., White J.S., Brongersma M.L. (2010) Plasmonics for extreme light concentration and manipulation, *Nat. Mater.* **9**, 193–204.
6 Boltasseva A., Atwater H.A. (2011) Low-loss plasmonic metamaterials, *Science* **331**, 290–291.
7 Aspnes D.E., Kinsbron E., Bacon D.D. (1980) Optical properties of Au: sample effects, *Phys. Rev. B* **21**, 3290–3300.
8 Mills D.L. (1976) Attenuation of surface polaritons by surface roughness, *Phys. Rev. B* **12**, 5539.
9 Burke J.J., Stegeman G.I., Tamir T. (1986) Surface-polariton-like waves guided by thin, lossy metal films, *Phys. Rev. B* **33**, 5186–5201.
10 Kuttge M., Vesseur E.J.R., Verhoeven J., Lezec H.J., Atwater H.A., Polman A. (2008) Loss mechanisms of surface plasmon polaritons on gold probed by cathodoluminescence imaging spectroscopy, *Appl. Phys. Lett.* **93**, 113110.
11 Lebsir Y., Boroviks S., Thomaschewski M., Bozhevolnyi S.I., Zenin V.A. (2022) Ultimate limit for optical losses in gold, revealed by quantitative near-field microscopy, *Nano Lett.* **22**, 5759–5764.
12 Reddy H., Guler U., Kildishev A.V., Boltasseva A., Shalaev V.M. (2016) Temperature-dependent optical properties of gold thin films, *Opt. Mater. Express* **6**, 2776–2802.
13 Huang J.-S., Callegari V., Geisler P., Brüning C., Kern J., Prangsma J.C., Wu X., Feichtner T., Ziegler J., Weinmann P., Kamp M., Forchel A., Biagioni P., Sennhauser U., Hecht B. (2010) Atomically flat single-crystalline gold nanostructures for plasmonic nanocircuitry, *Nat. Commun.* **1**, 150.
14 Grayli S.V., Zhang X., MacNab F.C., Kamal S., Star D., Leach G.W. (2020) Scalable, green fabrication of single-crystal noble metal films and nanostructures for low-loss nanotechnology applications, *ACS Nano* **14**, 7581.
15 Hecht B., Bielefeldt H., Novotny L., Inouye Y., Pohl D.W. (1996) Local excitation, scattering, and interference of surface plasmons, *Phys. Rev. Lett.* **77**, 1889–1892.
16 Biagioni P., Della Valle G., Ornigotti M., Finazzi M., Duò L., Laporta P., Longhi S. (2008) Experimental demonstration of the optical Zeno effect by scanning tunneling optical microscopy, *Opt Exp.* **16**, 3762–3767.
17 Sicot M., Andrieu S., Tiusan C., Montaigne F., Bertran F. (2006) On the quality of molecular-beam epitaxy grown Fe/MgO and Co/MgO (001) interfaces, *J. Appl. Phys.* **99**, 08D301.

18 Benia H.M., Lin X., Gao H.-J., Nilius N., Freund H.-J. (2007) Nucleation and growth of gold on MgO thin films: a combined STM and luminescence study, *J. Phys. Chem. C* **111**, 10528.
19 Rickart M., Roos B.F.P., Mewes T., Jorzick J., Demokritov S.O., Hillenbrands B. (2001) Morphology of epitaxial metallic layers on MgO substrates: influence of submonolayer carbon contamination, *Surf. Sci.* **495**, 68–76.
20 Etienne P., Massies J., Lequien S., Cabanel R., Petroff F. (1991) Molecular beam epitaxial growth of Cr/Fe, Ag/Fe, Ag/Cr and Ag/Co superlattices on MgO (001) substrates, *J. Crystal Growth* **111**, 1003–1010.
21 Etchegoin P.G., Le Ru E.C., Meyer M. (2006) An analytic model for the optical properties of gold, *J. Chem. Phys.* **125**, 164705 .

J. Eur. Opt. Society-Rapid Publ. 2025, **21**, 44

https://doi.org/10.1051/jeos/2025039
Available online at: https://jeos.edpsciences.org

Journal of the European Optical Society-Rapid Publications

PLASMONICA Collection
Nicoletta Granchi and Antonino Foti (Guest Editors)

RESEARCH ARTICLE OPEN ACCESS

Photonic crystal-like scaling behavior of localized Anderson modes in hyperuniform disordered systems

Nicoletta Granchi[1,*], Gabriele Calusi[1], Camilla Gonzini[1], Matteo Lodde[2], Kris Stokkereit[3], Paul J. van Veldhoven[2], Andrea Fiore[2], Marian Florescu[4], and Francesca Intonti[1]

[1] Department of Physics and Astronomy, Via Sansone 1, Sesto Fiorentino 50019, Italy; and LENS, University of Florence, Via Nello Carrara 1, Sesto Fiorentino 50019, Italy
[2] Department of Applied Physics and Science Education, Eindhoven University of Technology, Groene Loper 19, 5612 Eindhoven, The Netherlands
[3] Advanced Technology Institute, University of Surrey, Guildford, Surrey, GU2 7XH, UK
[4] Optoelectronics Research Centre, University of Southampton, Building 46, University Road, Southampton SO17 1BJ, UK

Received 30 July 2025 / Accepted 6 September 2025

Abstract. Hyperuniform disordered structures have emerged as a promising photonic platform that bridges the benefits of ordered and disordered structures, offering isotropic photonic band gaps, high spectral mode density, and robustness to imperfections. In this work, we provide direct experimental evidence that Anderson-localized dielectric modes in such systems exhibit spectral scaling behavior analogous to that found in photonic crystals. By systematically varying the filling fraction and length scale of hyperuniform disordered dielectric structures, we observe predictable and rigid spectral shifts in localized mode resonances. Hyperspectral scanning near-field optical microscopy enables simultaneous access to spatial and spectral information, confirming that these modes retain their spatial profiles and localization across scale variations. Our results demonstrate that Anderson localization in hyperuniform disordered systems obeys conventional photonic scaling laws despite the absence of long-range periodicity, while maintaining unique advantages such as isotropy, disorder tolerance and large photonic bandgaps. These findings highlight the potential of hyperuniform disordered materials as scalable and flexible platforms for integrated photonics, cavity quantum electrodynamics, and broadband optical devices.

Keywords: Photonic-crystals, Anderson localization, Hyperuniform disorder, Near-field Scanning Probe Microscopy.

1 Introduction

Photonic structures engineered for precise control over light propagation have historically relied on periodicity to open photonic band gaps (PBGs) and confine electromagnetic modes [1–3]. While photonic crystals (PhCs) offer excellent confinement and spectral control, their performance can be hindered by low spatial and spectral density of states, inherent anisotropies and strict symmetry constraints [1–5]. In contrast, a special class of correlated disorder systems, hyperuniform disordered (HuD) photonic structures [6], filling the gap between perfect periodicity and complete randomness, have emerged as a compelling alternative offering both large, isotropic PBGs and high flexibility in device integration [7–11]. HuD structures are particularly attractive for applications where direction-independent light manipulation is crucial, such as photovoltaics, sensing, and light-emitting devices [12–21]. Among HuD systems, a peculiar role is played by stealthy HuD structures, characterized by both suppressed long-range density fluctuations and vanishing scattering in a defined range of spatial frequencies [7, 22, 23]. Formally, in reciprocal (Fourier) space, the hallmark of hyperuniformity corresponds to a vanishing structure factor $S(k)$ in the long wavelength limit. A stealthy hyperuniform system imposes an even stricter condition: $S(k) = 0$ for all $|k| < k_c$ for some positive cutoff wavevector k_c. This implies that the system is completely transparent (i.e., non-scattering) to long-wavelength Fourier components up to that threshold, hence the stealthy term. In the context of photonics, stealthy HuD systems have been shown to display large, complete PBG [9]. As previously demonstrated, this PBG results from interplay of hyperuniformity, short-range geometric order, and uniform local topology [9]; its generation is specifically linked to the Mie resonances [9, 24–27] of the individual

* Corresponding author: granchi@lens.unifi.it

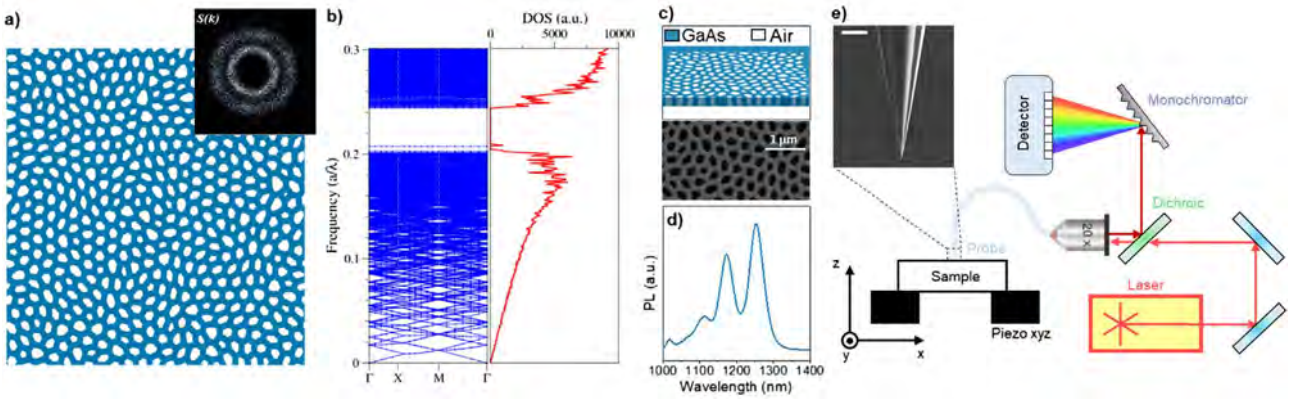

Fig. 1. a) HuD design with corresponding structure factor in the inset. b) Photonic band structure (left) and DOS (right) calculated using 500 k-points randomly distributed in the first Brillouin zone associated with the HuD supercell. c) Sketch of the patterned single membrane (top) and SEM detail of one of the fabricated samples (bottom). d) PL emission spectrum of the QDs embedded in the middle of the membrane. e) Sketch of hyperspectral SNOM setup used in illumination/collection configuration.

scattering centers within the structure, as it occurs when the scattered field is out of phase with the incident field, resulting in the absence of a propagation channel for light. This breakthrough in the field of photonics, by demonstrating that long-range periodicity is not necessary for the opening of a PBG, has showcased the potentiality of HuD systems. Moreover, it opened the path to exploring whether such systems could merge the benefits of structural disorder, such as isotropy and robustness, with the functional advantages of order, including coherent light control and bandgap formation [9, 15]. For instance, high-Q cavities and freeform waveguides have been demonstrated both theoretically and experimentally [17–20]. Moreover, a key indicator of the versatility of HuD photonic systems is their ability to host Anderson dielectric modes at the edges of the PBG [15, 16]. These modes, resulting from structural correlations rather than periodicity breaking, have been shown to exhibit high quality factors and small mode volumes in patterned semiconductor slabs, aspects typically associated with engineered cavities in PhCs. Remarkably, such modes have been found to be more robust to fabrication induced disorder than their periodic counterparts [15, 16].

A central question in the study of HuD photonic materials is the extent to which their optical modes can mimic those of PhCs, particularly in terms of mode scaling and predictability. The ability to control and tune the resonances of a photonic structure is a matter of crucial importance in the framework of light-matter interaction applications, where guaranteeing the spectral and spatial overlap between modes and quantum emitters is mandatory. While it has already been proven that an engineered cavity with resonance inside the PBG of a HuD network exhibits a systematic and predictable spectral shift as expected in correspondence of air or dielectric defects [18], Anderson localized modes arising at the PBG edges remain unexplored under this perspective. In this work, we provide direct experimental evidence that Anderson-localized dielectric modes in HuD networks on slab exhibit systematic spectral shifts when geometrical parameters such as the filling fraction and length scale are varied. This scaling behavior mirrors the conventional scaling laws of PhCs [4], where the photonic band structure rigidly shifts with the unit cell dimension and refractive index contrast. Our results were obtained through hyperspectral scanning near-field optical microscopy (SNOM), which provides spatially and spectrally resolved maps of the local density of optical states (DOS) with subwavelength resolution. The observation of rigid, predictable spectral tuning in correlated disordered systems further supports the notion that HuD materials, while carrying strategic advantages like isotropy and high spectral density, can replicate the functional capabilities of periodic architectures.

2 Material and methods

2.1 Theoretical design

The pattern, shown in Figure 1a, is constructed within periodic boundary conditions, using a square domain of side length L. A characteristic length scale $a = L/\sqrt{N}$ is then introduced in analogy with the PhCs lattice constant, ensuring a uniform point density of $1/a^2$, where N denotes the number of scattering centers within the supercell.

The 2D HuD network geometry was built according to the protocol reported in Ref. [9] and is defined as stealthy as shown in the inset of Figure 1a: the structure factor $S(k)$ is exactly zero for a discrete set of wavevectors around the origin [7–9]. While exhibiting the suppression of large-scale density fluctuations as in photonic crystals, the HuD's structure factor resembles the isotropy typical of random systems [6–8, 28, 29]. Through the supercell approach, it is then possible to calculate the 2D photonic bandstructure, showing a large and isotropic PBG (Fig. 1b); the right panel of Figure 1b shows the corresponding photonic Density of States (DOS) calculated using 500 randomly distributed points in the first Brillouin zone associated with the HuD supercell.

2.2 Sample fabrication

The fabricated devices are based on GaAs optically active slabs, incorporating high density of InAs quantum dots

(QDs) that emit between 1100 nm 1300 nm. A layer stack of a 250 nm-thick GaAs membrane on top of a 3 µm-thick AlGaAs sacrificial layer that separates the membrane from the GaAs substrate was used to manufacture one wafer. A layer of self-assembled InAs QDs was integrated in the center of the GaAs membrane on a different wafer that was generated with the same layer stack and nominal thicknesses. A molecular-beam epitaxy reactor was used for growth, and the growth parameters were adjusted to guarantee a QD density of 175 μm^{-2} [30]. The HuD geometry is patterned through electron-beam lithography, followed by reactive-ion etching and a selective removal of the AlGaAs sacrificial layer [15, 16, 18, 31, 32]. A sketch of the single membrane system is reported in Figure 1c, on top of a detailed view of one of the fabricated samples is presented in the scanning electron microscope (SEM) image, while the QDs photoluminescence (PL) emission spectrum is reported in Figure 1d. The two main peaks observed in the PL spectrum correspond to the ground and first excited state of the QDs emitting at room temperature. Each sample was fabricated by changing two structural parameters: 1) The characteristic length scale a = 340, 360 and 380 nm; and 2) The wall thickness $w = 0.415a$, $0.461a$ and $0.5a$, i.e. the thickness of the dielectric veins in the networks, that influences the filling fraction. The structural parameters were carefully chosen at the design stage to guarantee the matching between the resonant modes of the HuD geometry and the QDs emission range.

2.3 Experimental setup

To optically characterize the samples we employ a commercial SNOM (Twinsnom, Omicron) in illumination/collection configuration, as sketched in Figure 1e. The probe is a chemically etched dielectric fiber that, by raster scanning the sample at a fixed distance (few tens of nm) allows to reconstruct both topographic and optical maps. The sample is excited by a laser diode at 785 nm, and both the excitation and the signal collection occur through the tip; the collected signal is dispersed by a spectrometer and collected by a cooled InGaAs array. At every tip position, the entire spectrum of the sample is collected with a spectral resolution of 0.1 nm. The SNOM tip collecting area, which has a lateral size of about 250 nm, is the estimated spatial resolution of our system.

3 Results and discussion

As argued above, it has been demonstrated that HuD photonic systems support Anderson-localized modes near the edges of the PBG, closely analogous to the dielectric and air band edge modes observed in photonic crystals [9, 15]. These modes, arising due to multiple scattering and interference effects intrinsic to the short-range order of the HuD architecture, are typically localized around either high- or low-index regions, corresponding to dielectric-like or air-like behavior, respectively. In this work we focus on the dielectric modes of the HuD sample. To investigate the scaling behavior and spectral tunability of Anderson dielectric modes, we have conducted a systematic near-field optical characterization on the series of samples based on the same underlying stealthy HuD point pattern but with varying length scale and normalized wall thicknesses a and w (see Sect. 2). Each structure was probed using the SNOM Hyper-Spectral Imaging (HSI) technique, which allows simultaneous access to both spatial and spectral information with subwavelength resolution. In HSI a full spectrum is collected for any spatial pixel of the near-field map (corresponding to a specific tip position during the scan). This allows us to reconstruct hyperspectral maps that can either be filtered around a single wavelength, for example the central wavelength of a single peak, or around broad spectral interval. Figure 2 presents a direct comparison of the same Anderson-localized dielectric mode as it appears in three structures with the same a = 380 nm and varying the thickness of the dielectric veins. The SNOM PL intensity maps, filtered around the tuned resonant wavelength of the mode (respectively 1161.6, 1205.3 and 1245.8 nm), are reported in Figure 2a, revealing the spatial profile of the mode across all samples. Despite the variation in wall thickness, the mode exhibits a similar localized spatial distribution in each case, demonstrating its reproducibility and robustness to geometric scaling. The variation in wall thickness is visible in the corresponding SNOM topographies, reported in Figure 2b. Notably, changing w while keeping a constant (or the reverse) is analogous to changing the filling fraction of the photonic pattern. Figure 2c displays the corresponding PL spectra, acquired in the points of maximum intensity for each of the three measurements of Figure 2a. A systematic redshift of the resonance peaks of about 40 nm is observed as the wall thickness increases. This behavior is analogue in photonic crystals, where the mode resonant wavelengths of PhC cavities exhibit a redshift (blueshift) in correspondence of an increase (decrease) of dielectric material [4, 18]. In this regard, since in PhC the filling fraction is one of the parameters determining the optimal condition for high quality factors (Q) [33], we also evaluate the Q of the same mode in three different samples with three different values of w and report them in the right panel of Figure 2c; the values are obtained by fitting with a Lorentzian curve the peaks corresponding to the resonances. We observe that by decreasing the size of the air holes (i.e. increasing w), the Q-factor is increased, meaning that a smaller filling fraction is responsible for a more efficient confinement of light.

To complete this analysis, we fixed the normalized wall thickness at $w = 0.5a$ and systematically varied the absolute length scale a across multiple samples, focusing on the same Anderson dielectric mode. This approach isolates the effect of global length scale on the spectral position of the modes, in analogy with 2D photonic crystal on slab scaling laws where eigenfrequencies scale inversely with lattice periodicity. Figure 3a shows the PL spectra acquired from three structures with lattice constants a = 340, 360 and 380 nm all with the same relative wall thickness $w = 0.5a$. A clear and rigid red shift of the Anderson-localized modes is observed as a increases, consistent with the expected linear scaling of the photonic band structure. The resonance peaks shift by 40–50 nm over this range,

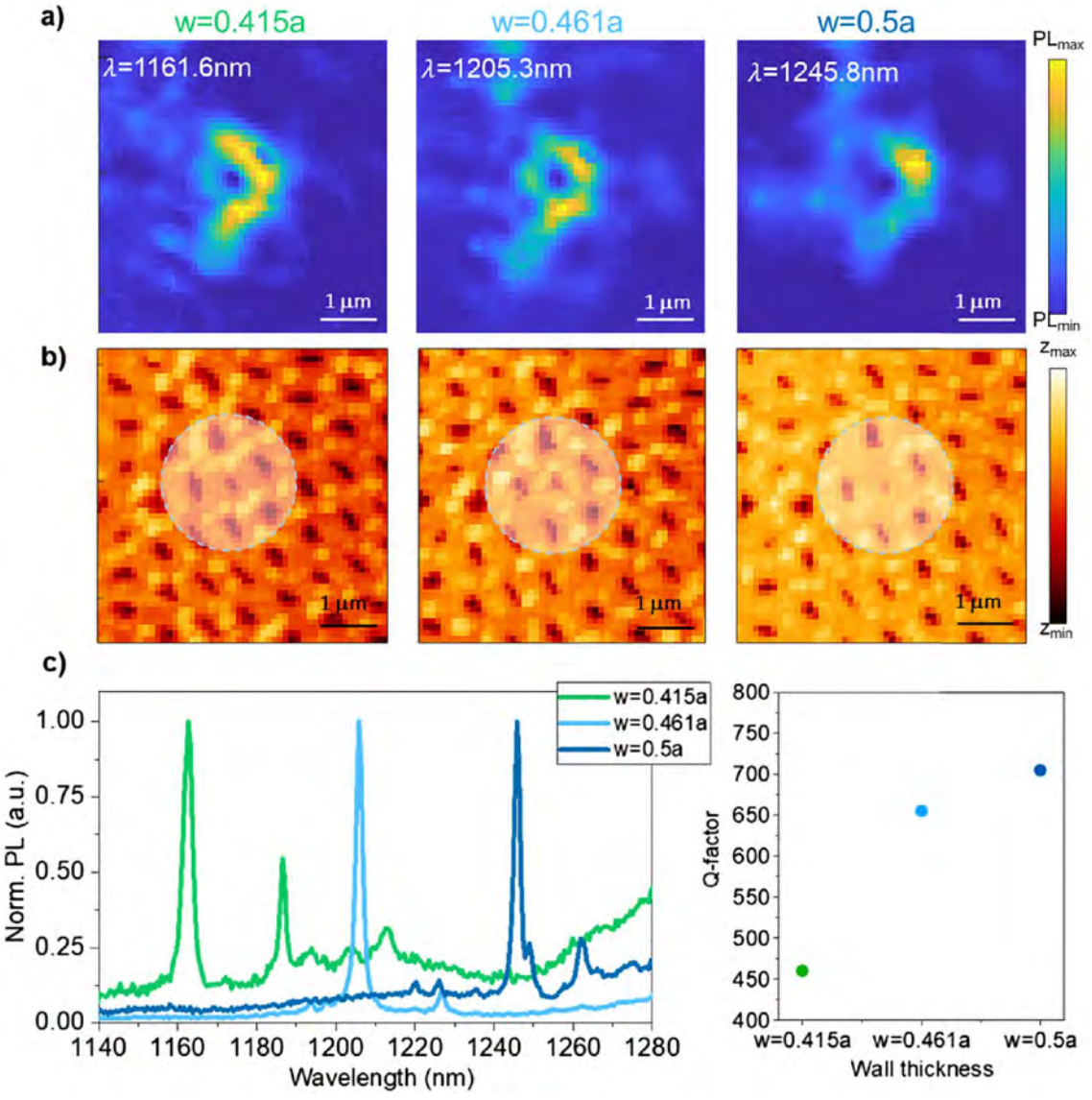

Fig. 2. a) PL SNOM maps of the an Anderson-localized mode in three HuD structures with increasing normalized wall thicknesses $w = 0.415a$, $0.461a$ and $0.5a$ ($a = 380$ nm), showing the same mode localization distribution across all three samples. The maps are filtered around the resonant wavelengths of respectively 1161.6, 1205.3 and 1245.8 nm. b) Corresponding SNOM topographies. c) PL spectra collected in the point of maximum intensity of the mode in each structure, showing a systematic red shift in resonance wavelength as wall thickness increases, in agreement with photonic crystal scaling laws. Right panel: experimental Q factors of the corresponding resonances for different values of w.

confirming that the localized modes respond predictably to changes in lattice scale, just as in periodic photonic crystals. The inset of Figure 3b shows a near-field PL map of the analyzed mode for $a = 360$ nm, showcasing the preserved spatial distribution even in the case of different length scales. The graph in Figure 3b summarizes the spectral position of Anderson mode detected in all samples as a function of length scale a and wall thickness w. Each set of data points, plotted for the three wall thicknesses follows a consistent monotonic trend, further reinforcing the conclusion that Anderson-localized modes in HuD structures follow conventional photonic scaling laws, despite the absence of long-range periodicity.

4 Conclusions

Our results provide direct and compelling experimental evidence that Anderson-localized dielectric modes in HuD photonic structures are both spatially robust and spectrally scalable, in close analogy with the behavior of modes in photonic crystals, despite the absence of long-range periodicity. Using hyperspectral near-field optical microscopy, we demonstrated that systematic variations in geometrical parameters lead to predictable and rigid spectral shifts of localized modes. These findings establish that HuD systems obey the same scaling laws traditionally associated with periodic photonic architecture.

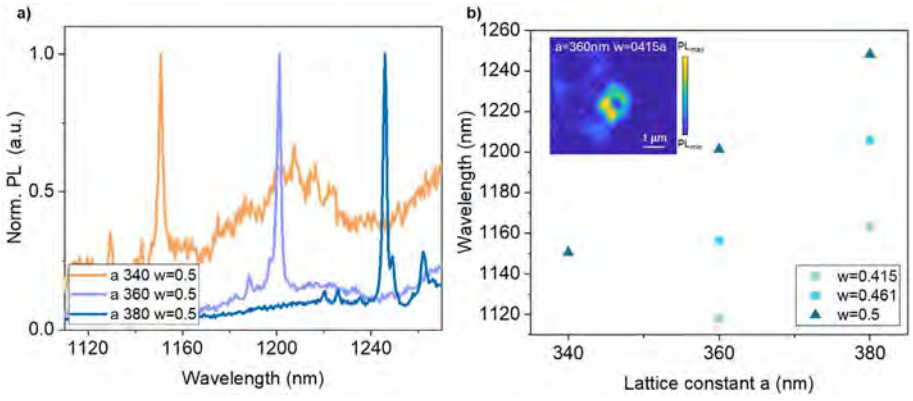

Fig. 3. a) SNOM PL spectra collected in the point of maximum intensity of the mode in each with fixed wall thickness $w = 0.5a$ and varying lattice constants $a = 340$ nm, 360 nm, 380 nm. b) Summary plot showing resonance wavelength versus length scale a for the three different wall thicknesses. The inset shows a SNOM PL map of the studied mode detected in a structure with $a = 360$ nm and $w = 0.415a$.

Importantly, this scaling behavior occurs in structures that retain the key advantages of disorder, such as isotropy, high modal density, and robustness to fabrication imperfections, features that are often unattainable in conventional photonic crystals. This comparison further validates that HuD materials can effectively emulate the spectral functionality of photonic crystals, while surpassing them in terms of design flexibility and direction-independent performance. By confirming that disorder is not always a constraint but can be a tunable photonic design parameter, this work opens a path toward a new class of scalable, disorder-enabled photonic devices, such as broadband emitters, isotropic filters, integrated light sources, and quantum photonic platforms. Our findings not only bridge the gap between order and disorder in nanophotonics but also offer a blueprint for leveraging structurally correlated disorder to engineer optical functionalities with a degree of control previously reserved for periodic systems.

Funding

This research has been cofunded by the European Union – NextGeneration EU, "Integrated infrastructure initiative in Photonic and Quantum Sciences" – I-PHOQS [IR0000016, ID D2B8D520, CUP B53C22001750006] and by Netherlands Organization for Scientific Research (NWO/OCW), as part of the Vrij Programma (Grant no. 680-92-18-04) grant and of the Zwaartekracht Research Center for Integrated Nanophotonics (Grant no. 024.002.033). M.F. acknowledges EPSRC (United Kingdom) support under Grant no. EP/Y016440/1 award and the use of the IRIDIS High Performance Computing Facility, and associated support services at the University of Southampton. C.G. and F.I. acknowledge funding from project CNR-FOE-LENS 2023.

Conflicts of interest

The authors have nothing to disclose.

Data availability statement

Data underlying the results presented in this paper are not publicly available at this time but may be obtained from the authors upon reasonable request.

Author contribution statement

Conceptualization, N.G, F.I. and M.F.; Methodology N.G, F.I., M.F. M.L, P.J.V; Software, M.F., K.S.; Investigation, N.G, G.C and C.G; Resources, A.F., M.F. and F.I.; Data Curation, N.G.; Writing – Original Draft Preparation, N.G.; Writing – Review & Editing, N.G, F.I., M.F., A.F.; Supervision, F.I.

References

1 Yablonovitch E, Photonic band-gap structures, *J. Opt. Soc. Am. B* **10**, 283–295 (1993). https://doi.org/10.1364/JOSAB.10.000283.
2 Akahane Y, Asano T, Song BS, Noda S, High-Q photonic nanocavity in a two-dimensional photonic crystal, *Nature* **425**, 944 (2003). https://doi.org/10.1038/nature02063.
3 Sekoguchi H, Takahashi Y, Asano T, Noda S. Photonic crystal nanocavity with a Q-factor of 9 million, *Opt. Express* **22**, 916 (2014). https://doi.org/10.1364/OE.22.000916.
4 Joannopoulos JD, Johnson SG, Winn JN, Meade RD, *Photonic crystals: molding the flow of light*, Second Edition (Princeton University Press, Princeton, New Jersey, 2011). ISBN 978-0-691-12456-8.
5 Chehadi Z, Montanari M, Granchi N, Modaresialam M, Koudia M, Abel M, Putero M, Grosso D, Intonti F, Abbarchi M, Soft nano-imprint lithography of rare-earth-doped light-emitting photonic metasurface, *Adv. Opt. Mat.* **10**(21), 2201618 (2022). https://doi.org/10.1002/adom.202201618.
6 Vynck K, Pierrat R, Carminati R, Froufe-Pérez LS, Scheffold F, Sapienza R, Vignolini S, Sáenz JJ, Light in correlated disordered media, *Rev. Mod. Phys.* **95**, 045003 (2023). https://doi.org/10.1103/RevModPhys.95.045003
7 Torquato S, Stillinger FH. Local density fluctuations, hyperuniformity, and order metrics *Phys. Rev. E* **68**, 041113 (2003). https://doi.org/10.1103/PhysRevE.68.041113.
8 Torquato S, Hyperuniform states of matter, *Phys. Reports* **745**, 1–95 (2018). https://doi.org/10.1016/j.physrep.2018.03.001.
9 Florescu M, Torquato S, Steinhardt PJ, Designer disordered materials with large, complete photonic band gaps, *PNAS* **106**, 20658 (2009). https://doi.org/10.1073/pnas.0907744106.
10 Froufe-Pérez LS, Engel M, Damasceno PF, Muller N, Haberko J, Glotzer SC, Scheffold F, Role of short-range order and hyperuniformity in the formation of band gaps in

disordered photonic materials, *Phys. Rev. Lett.* **117**, 053902 (2016). https://doi.org/10.1103/PhysRevLett.117.053902.
11 Froufe-Pérez LS, Engel M, Sáenz JJ, Scheffold F, Band gap formation and Anderson localization in disordered photonic materials with structural correlations, *PNAS* **114**(36), 9570–9574 (2017). https://doi.org/10.1073/pnas. 1705130114.
12 Degl'Innocenti R, Shah Y, Masini L, Ronzani A, Pitanti A, Ren Y, Jessop D, Tredicucci A, Beere HE, Ritchie DA, Hyperuniform disordered terahertz quantum cascade laser, *Sci. Rep.* **6**, 19325 (2016). https://doi.org/10.1038/srep19325.
13 Tavakoli N, Spalding R, Lambertz A, Koppejan P, Gkantzounis G, Wan C, Röhrich R, Kontoleta E, Koenderink AF, Sapienza R, Florescu M, Alarcon-Llado E, Over 65% sunlight absorption in a 1 μm Si slab with hyperuniform texture, *ACS Photon.* **9**(4), 1206–1217 (2022). https://doi.org/10.1021/acsphotonics.1c01668.
14 Aubry GJ, Froufe-Pérez LS, Kuhl U, Legrand O, Scheffold F, Mortessagne F, Experimental tuning of transport regimes in hyperuniform disordered photonic materials, *Phys. Rev. Lett.* **125**, 127402 (2020). https://doi.org/10.1103/PhysRevLett.125.127402.
15 Granchi N, Spalding R, Lodde M, Petruzzella M, Otten FW, Fiore A, Intonti F, Sapienza R, Florescu MGurioli M, Near-field investigation of luminescent hyperuniform disordered materials, *Adv. Optical Mater.* **10**, 2102565 (2022). https://doi.org/10.1002/adom.202102565.
16 Granchi N, Spalding R, Stokkerei K, Lodde M, Petruzzella M, Otten FV, Sapienza R, Fiore A, Florescu M, Intonti F, High spatial resolution imaging of light localization in hyperuniform disordered patterns of circular air pores in a dielectric slab, *Front. Photonics* **4**, 1199411 (2023). https://doi.org/10.3389/fphot.2023.1199411.
17 Amoah T, Florescu M, High-Q optical cavities in hyperuniform disordered materials, *Phys. Rev. B* **91**, 020201(R) (2015). https://doi.org/10.1103/PhysRevB.91.020201.
18 Granchi N, Lodde M, Stokkereit K, Spalding S, van Veldhoven PJ, Sapienza R, Fiore A, Gurioli M, Florescu M, Intonti F, Near-field imaging of optical nanocavities in hyperuniform disordered materials, *Phys.* Rev. B **107**. 064204 (2023). https://doi.org/10.1103/PhysRevB.107.064204.
19 Milošević MM, Man W, Nahal G, Steinhardt PJ, Torquato S, Chaikin PM, Amoah T, Bowen Y, Mullen RA, Florescu M, Hyperuniform disordered waveguides and devices for near infrared silicon photonics, *Sci Rep* **9**, 20338 (2019). https://doi.org/10.1038/s41598-019-56692-5.
20 Man W, Florescu M, Williamson EP, He Y, Hashemizad SR, Leung BYC, Liner DR, Torquato S, Chaikin PM, Steinhardt PJ, Isotropic band gaps and freeform waveguides observed in hyperuniform disordered photonic solids, *PNAS* **110**(40), 15886–15891 (2013). https://doi.org/10.1073/pnas.1307879110.
21 Froufe-Pérez LS, Aubry GJ, Scheffold F, Magkiriadou S, Bandgap fluctuations and robustness in two-dimensional hyperuniform dielectric materials, *Opt. Express* **31**, 18509–18515 (2023). https://doi.org/10.1364/OE.484232.
22 Leseur O, Pierrat R, Carminati R, High-density hyperuniform materials can be transparent, *Optica* **3**, 763 (2016). https://doi.org/10.1364/OPTICA.3.000763.
23 Kim J, Torquato S, Extraordinary optical and transport properties of disordered stealthy hyperuniform two-phase media, *J. Phys Condens. Matter* **36**, 225701 (2024). https://doi.org/10.1088/1361-648X/ad2802.
24 Kuznetsov AI, Miroshnichenko AE, Fu YH, Zhang J, Luk'yanchuk B, Magnetic light, *Sci. Rep.* **2**, 492 (2012). https://doi.org/10.1038/srep00492.
25 Liu W, Kivshar YS, Generalized Kerker effects in nanophotonics and meta-optics, *Opt. Express* **26**, 13085–13105 (2018). https://doi.org/10.1364/OE.26.013085.
26 Granchi N, Fagiani L, Salvalaglio M, Barri C, Ristori A, Montanari M, Gurioli M, Abbarchi M, Voigt A, Vincenti MA, Intonti F, Bollani M, Engineering and detection of light scattering directionalities in dewetted nanoresonators through dark-field scanning microscopy, *Opt. Express* **31**, 9007 (2023). https://doi.org/10.1364/OE.481971.
27 Fagiani L, Granchi L, Zilli A, Barri C, Rusconi F, Montanari M, Mafakheri E, Celebrano M, Bouabdellaoui M, Abbarchi M, Intonti F, Khursheed A, Biagioni P, Finazzi M, Vincenti MA, Bollani M, Linear and nonlinear optical properties of dewetted SiGe islands, *Opt. Mater. X* **13**, 100116 (2022). https://doi.org/10.1016/j.omx.2021.100116.
28 Wiersma DS, Disordered photonics, *Nat. Photonics* **7**, 188–196 (2013). https://doi.org/10.1038/nphoton.2013.29.
29 Granchi N, Intonti F, Florescu M, García PD, Gurioli M, Arregui G, Q-Factor optimization of modes in ordered and disordered photonic systems using non-Hermitian Perturbation Theory, *ACS Photon.* **10**(8), 2808–2815 (2023). https://doi.org/10.1021/acsphotonics.3c00510.
30 Lodde M, van Veldhoven RPJ, Verhagen E, Fiore A, The effect of In(Ga)As/GaAs quantum dots on the optical loss of photonic crystal cavities, *J. Appl. Phys.* **135**(6), 063103 (2024). https://doi.org/10.1063/5.0189904.
31 Intonti F, Caselli N, Vignolini S, Riboli F, Kumar S, Rastelli A, Schmidt OG, Francardi M, Gerardino A, Balet LP, Li LH, Fiore A, Gurioli M, Spectral tuning and near-field imaging of photonic crystal microcavities, *Phys Rev. B* **78**, 041401 (2008). https://doi.org/10.1103/PhysRevB.78.041401.
32 Francardi M, Balet L, Gerardino A, Monat C, Zinoni C, Li LH, Alloing B, Le Thomas N, Houdré R, Fiore A, Quantum dot photonic crystal nanocavities at 1300 nm for telecom-wavelength single-photon sources, *Phys. Status Solidi C* **3**, 3693 (2006). https://doi.org/10.1002/pssc.200671612.
33 Englund D, Fushman I, Vuckovic J, General recipe for designing photonic crystal cavities, *Opt. Express* **13**, 5961–5975 (2005). https://doi.org/10.1364/OPEX.13.005961.

J. Eur. Opt. Society-Rapid Publ. 2024, **20**, 14

https://doi.org/10.1051/jeos/2024012
Available online at: https://jeos.edpsciences.org

Journal of the European Optical Society-Rapid Publications

Special Issue - Plasmonica 2023
Antonino Foti and Attilio Zilli (Guest editors)

SHORT COMMUNICATION OPEN ACCESS

Germanium Fabry-Perot nanoresonators investigated by cathodoluminescence spectroscopy

Sandro Mignuzzi[1], Xiaofei Wu[2], Bert Hecht[2], Jacopo Frigerio[3], Giovanni Isella[3], Michele Celebrano[4], Marco Finazzi[4], Riccardo Sapienza[1], and Paolo Biagioni[4,*]

[1] Blackett Laboratory, Department of Physics, Imperial College London, Prince Consort Rd, London SW7 2BW, United Kingdom
[2] Nano-optics and Biophotonics Group, Experimental Physics 5, Institute of Physics, University of Würzburg, Am Hubland, 97074 Würzburg, Germany
[3] L-NESS, Dipartimento di Fisica, Politecnico di Milano, Polo di Como, Via Anzani 42, 22100 Como, Italy
[4] Dipartimento di Fisica, Politecnico di Milano, Piazza Leonardo da Vinci 32, 20133 Milano, Italy

Received 11 January 2024 / Accepted 16 March 2024

Abstract. We report on the experimental investigation, by means of spatially-resolved cathodoluminescence spectroscopy, of rectangular all-dielectric Ge nanoantennas sustaining Fabry-Perot resonances. The combination of spatial and spectral resolution allows us to directly image the standing-wave pattern of the local density of optical states inside the nanoantennas, which is the fingerprint of the resonant Purcell contribution to the overall emission enhancement previously reported in the literature for the same structures. Our results confirm that the emission properties of Ge nanostructures can be effectively tuned by engineering the local density of optical states and that cathodoluminescence provides valuable information to experimentally address such modulation in their emission properties.

Keywords: Dielectric nanoantennas, Cathodoluminesce spectroscopy, Germanium.

All-dielectric nanoresonators operating in the visible and near-infrared spectral range have become a crucial ingredient for the enhancement of light-matter interactions at the nanoscale, since they combine a large local density of optical states with negligible absorption losses [1–3]. High-index, undoped semiconducting materials have been employed to realize dielectric nanoantennas, often in the form of individual disks or cylinders that support a rich variety of Mie resonances [4–8]. Many other geometries have also been explored, such as disk dimers [9–11], hollow structures [7, 12, 13], nanowires [14], or nanoscale truncated waveguides supporting Fabry-Perot resonances [15–18].

The optical characterization of individual dielectric nanoantennas typically relies on confocal microscopy, exploiting either elastic scattering [4, 14, 16], photoluminescence from the antenna material [15], nonlinear effects [5–7, 10], or the coupling with photon emitters [7, 9, 11, 19]. However, diffraction-limited optical techniques do not allow resolving the spatial features of the resonant field distribution inside the dielectric nanoantennas. To this aim, both near-field microscopy [18, 20, 21] and scanning-electron cathodoluminescence microscopy [22–24] have been applied. Specifically, apertureless near-field microscopy is mostly sensitive to the out-of-plane component (along the tip axis) of the local electric field outside the nanoantenna, which is efficiently scattered by the tip, while cathodoluminescence relies on the broadband generation of photons when a fast electron impinges onto a surface. Such an interaction can be effectively described as giving rise to a point-like emitting dipole, which makes spatially-resolved cathodoluminescence the ideal tool to experimentally address the local density of photonic states inside the nanoantenna [25–27].

Ge nanoantennas fabricated on Si in the form of rectangular nanoscale waveguide resonators already demonstrated an almost 30-fold enhancement in the collected spontaneous emission per unit volume compared to a continuous Ge film [15]. The Purcell contribution (reduction of the excited-state lifetime) to such enhancement, in particular, was analyzed with finite-difference time-domain simulations and attributed to the presence of Fabry-Perot resonances for the fundamental transverse-electric (TE) and transverse-magnetic (TM) modes supported by the nanoantennas. Yet, only indirect evidence was provided about this explanation, *i.e.* the measured enhancement of the Ge direct-gap emission as a function of the antenna length.

* Corresponding author: paolo.biagioni@polimi.it

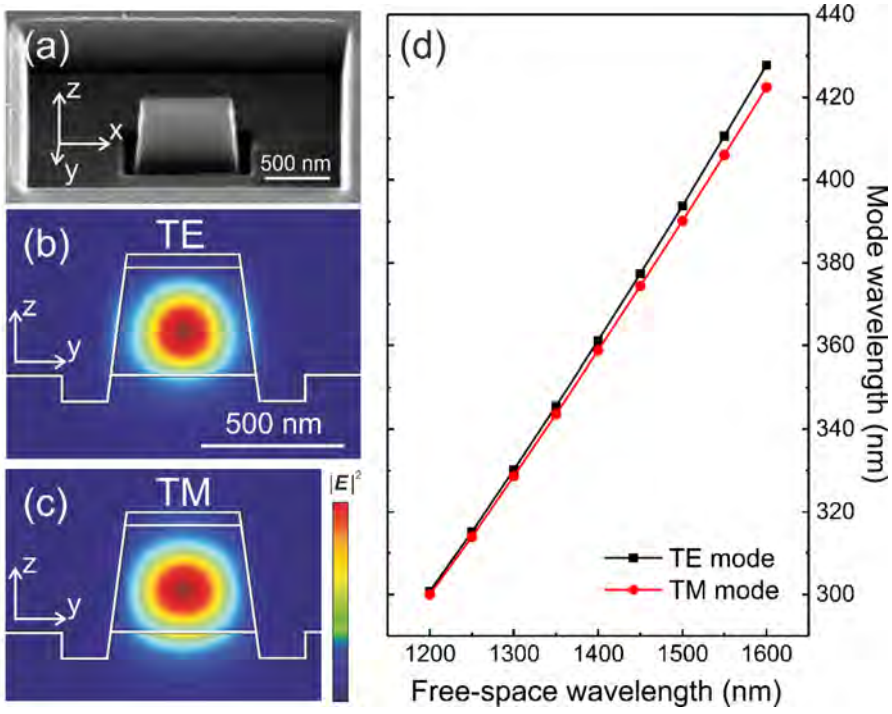

Fig. 1. Investigated Ge nanoantennas: (a) representative scanning electron microscopy image; (b, c) intensity profile of the fundamental TE and TM modes, respectively, simulated employing the mode source in the FDTD Ansys Lumerical software; (d) dispersion relations (mode wavelength as a function of the free-space wavelength) for the fundamental TE and TM modes.

In this work, we provide direct evidence of Fabry-Perot standing waves in such Ge nanoantennas exploiting cathodoluminescence microscopy. By doing so, we demonstrate that a standing wave is indeed clearly visible along the nanoresonator when the resonance conditions are met. The effective index of the mode and its associated wavelength, as extracted from the experimental maps, are in very good agreement with the numerical predictions and confirm that the field enhancement in the investigated nanostructures can be partially attributed to Fabry-Perot resonances of the truncated waveguide.

The sample under investigation was fabricated by focused ion-beam milling employing Ga ions, starting from a 400-nm-thick heavily-doped Ge film grown on a standard Si(001) wafer by low-energy plasma-enhanced chemical vapor deposition (doping concentration around 10^{19} cm^{-3}) [28]. Each antenna can be described as a truncated waveguide with a fixed cross-section of about 400 × 400 nm^2 and varying length. A representative scanning electron microscopy image shown in Figure 1a points out that the actual nanostructure geometry presents tilted side walls and a slight undercut into the Si substrate around the milled antenna. All these features are accounted for in the numerical simulations. Moreover, the antenna is covered with a 50-nm-thick silicon oxide film, which is functional to increase the quality of the ion-beam milling, as discussed in references [15].

The cross section of the nanoresonator is designed so that only two almost-degenerate fundamental modes are sustained, with a dominant TE and TM character, respectively. Their intensity profiles on a plane coinciding with the transverse cross section of the antenna, simulated with the mode solver of the FDTD Ansys Lumerical software, are shown in Figures 1b and 1c, along with their dispersion relations (*i.e.* mode wavelength as a function of the free-space wavelength, see Fig. 1d).

In the setup employed for this work, cathodoluminescence is excited by a 30-keV electron beam inside a scanning electron microscope and is collected by a parabolic mirror (0.98 numerical aperture) that collimates the emitted radiation and redirects it through an optical collection system directly onto an InGaAs spectrometer, without the use of any optical fiber [23]. The experimental analysis is performed on the total intensity impinging onto the detector, with no sensitivity to the polarization state of the emitted light. We focus our analysis on an individual nanoantenna with a length of 1400 nm, as shown in the top-view scanning electron microscopy image of Figure 2a. The cathodoluminescence spectrum is acquired as a function of the position of the electron beam along the main antenna axis. The resulting two-dimensional map, representing the collected intensity as a function of the wavelength and the beam position, is reported in Figure 2b. A quick inspection of the map clearly reveals that, for specific wavelengths, a standing-wave pattern is visible inside the nanoantenna, which points to the occurrence of Fabry-Perot resonances modulating the local density of optical states available for the radiative decay of the emission dipoles. Such resonances are generated by the constructive interference of the two degenerate guided modes bouncing back and forth inside the truncated waveguide, thanks to the reflectivity of the end facets. They occur for antenna lengths that are equal

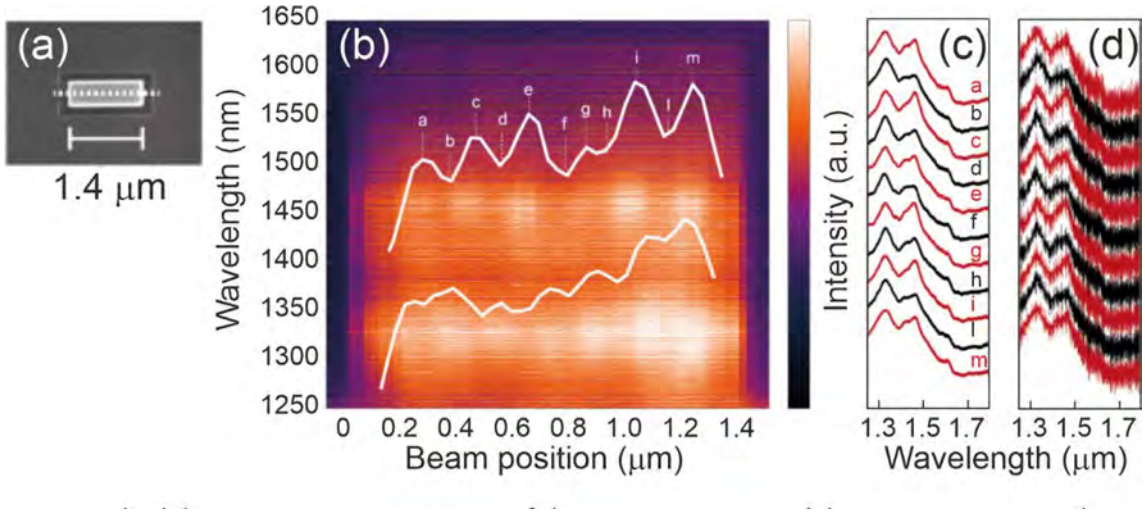

Fig. 2. Cathodoluminescence investigation of the Ge nanoantenna: (a) top-view scanning electron microscopy images of the investigated nanoantenna (the dashed line represents the trajectory of the scanning electron beam during the acquisition of the cathodoluminescence spectra); (b) two-dimensional map (emission wavelength as a function of the electron beam position along the antenna axis) from the cathodoluminescence investigation, with solid white lines representing the intensity profile integrated over a wavelength range of about 50 nm around each resonance; (c) smoothened cathodoluminescence spectra acquired at specific positions (marked with letters a-m on panel b) along the antenna axis, after vertical translation for sake of readability; (d) raw data for the smoothened cathodoluminescence spectra of panel c.

to a multiple of half the mode wavelength. In practice, the transition dipole generated by the keV electrons impinging onto the antenna can radiatively decay into the Fabry-Perot modes of the nanocavity. This mechanism determines a spatially-dependent decay rate, which reflects in the collected intensity signal. By averaging the spatially- and frequency-resolved signal over a wavelength range of about 50 nm around the two resonant wavelengths observed experimentally in Figure 2b, the white solid lines superimposed to the map are obtained, which allow for a more quantitative analysis of the phenomenon.

Evidence for the observed resonances is also provided by individual cathodoluminescence spectra in Figures 2c and 2d, which are acquired at specific locations along the antenna axis, as marked by the letters a–m in Figure 2b. Two peaks around 1330 nm and 1460 nm are clearly visible, corresponding to the central wavelengths of the standing-wave patterns in the map of Figure 2b.

To analyze and interpret the experimental findings, let us recall that the fundamental TE and TM modes in the truncated Ge waveguide are practically degenerate. As a result, they possess roughly the same mode wavelength, while higher order modes are not supported by the small cross section of the waveguide [15]. We expect that the standing-wave patterns imaged by the cathodoluminescence setup present a well-defined spatial periodicity of half the mode wavelength at the specific resonance frequency. Such a spatial periodicity can be easily evaluated by measuring the approximate distance between the outer intensity peaks in the standing-wave pattern and dividing by the number of the periods. By doing so, we find mode wavelengths of about 335 nm and 390 nm for the two resonance peaks. These experimental results are in excellent agreement with the simulations reported in Figure 1d, which predict mode wavelengths of about 338 nm and 380 nm for the same free-space wavelengths of 1330 nm and 1460 nm, respectively. Interestingly, the non-trivial lineshapes of the two main peaks in Figures 2c and 2d might be a hint of the non-perfect degeneracy of the TE and TM modes involved in the resonant emission process. It should also be noted, for sake of completeness, that for the two investigated resonances we observe 6 and 7 intensity maxima inside the antenna, *i.e.* we have evidence for Fabry-Perot modes in which the cavity length is 6 or 7 times the half mode wavelength, respectively. This would point to an expected cavity length of about 1350 nm sustaining such resonances. Indeed, the estimate of a nominal length of 1400 nm for the footprint of the investigated nanostructure does not take into account the presence of tilted side walls for the reflecting end facets, which results in a shorter effective length as demonstrated experimentally.

In conclusion, we employed spatially-resolved cathodoluminescence spectroscopy in a scanning electron microscope coupled to an optical spectrograph to provide direct experimental evidence of the presence of Fabry-Perot resonances in rectangular Ge nanoantennas. The investigation allows imaging the standing-wave pattern of the local density of optical states inside the nanoantenna and confirms that cathodoluminescence represents a key asset in the engineering of nanophotonic devices and in the experimental assessment of their performance. Perspective combinations of this technique with electron energy-loss spectroscopy might further enrich the information, leveraging the possibility to discriminate between local density of states and radiative local density of states and possibly also between TE and TM modes [29].

Funding

Funding from *Fondazione Cariplo* under the project "Nano antennas of germanium for advanced photonics (NANOGAP)" (project number 2010-0632) is gratefully acknowledged.

Conflicts of Interest

The authors declare that they have no competing interests to report.

Data availability statement

The data associated with this study is available upon request. Please contact the corresponding author to request access to the data.

Author contribution statement

All authors actively contributed to the design of the experiment, the discussion of the results, and the preparation of the manuscript. S.M. and R.S. performed the cathodoluminescence measurements. X.W., B.H., J.F., and G.I. performed the growth and nanofabrication of the Ge nanoantenna. M.C., M.F., and P.B. performed the numerical modeling.

References

1 Decker M., Staude I. (2016) Resonant dielectric nanostructures: a low-loss platform for functional nanophotonics, *J. Opt.* **18**, 103001.
2 Kuznetsov A.I., Miroshnichenko A.E., Brongersma M.L., Kivshar Y. S., Luk'yanchuk B. (2016) Optically resonant dielectric nanostructures, *Science* **354**, aag2472.
3 Alhalabya H., Zaraket H., Principe M. (2021) Enhanced photoluminescence with dielectric nanostructures: a review, *Results Opt.* **3**, 100073.
4 Staude I., Miroshnichenko A.E., Decker M., Fofang N.T., Liu S., Gonzales E., Dominguez J., Luk T.S., Neshev D.N., Brener I., Kivshar Y. (2013) Tailoring directional scattering through magnetic and electric resonances in subwavelength silicon nanodisks, *ACS Nano* **7**, 7824–7832.
5 Gili V.F., Carletti L., Locatelli A., Rocco D., Finazzi M., Ghirardini L., Favero I., Gomez C., Lemaître A., Celebrano M., De Angelis C., Leo G. (2016) Monolithic AlGaAs second-harmonic nanoantennas, *Opt. Exp.* **24**, 15965–15971.
6 Grinblat G., Li Y., Nielsen M.P., Oulton R.F., Maier S.A. (2017) Efficient third harmonic generation and nonlinear subwavelength imaging at a higher-order anapole mode in a single germanium nanodisk, *ACS Nano* **11**, 953–960.
7 Cambiasso J., Grinblat G., Li Y., Rakovich A., Cortés E., Maier S.A. (2017) Bridging the gap between dielectric nanophotonics and the visible regime with effectively lossless gallium phosphide antennas, *Nano Lett.* **17**, 1219–1225.
8 Capretti A., Lesage A., Gregorkiewicz T. (2017) Integrating quantum dots and dielectric Mie resonators: a hierarchical metamaterial inheriting the best of both, *ACS Photonics* **4**, 2187–2196.
9 Regmi R., Berthelot J., Winkler P.M., Mivelle M., Proust J., Bedu F., Ozerov I., Begou T., Lumeau J., Rigneault H., García-Parajó M.F., Bidault S., Wenger J., Bonod N. (2016) All-dielectric silicon nanogap antennas to enhance the fluorescence of single molecules, *Nano Lett.* **16**8, 5143–5151.
10 Carletti L., Rocco D., Locatelli A., De Angelis C., Gili V.F., Ravaro M., Favero I., Leo G., Finazzi M., Ghirardini L., Celebrano M., Marino G., Zayats A.V. (2017) Controlling second-harmonic generation at the nanoscale with monolithic AlGaAs-on-AlOx antennas, *Nanotechnology* **28**, 114005.
11 Sortino L., Zotev P.G., Phillips C.L., Brash A.J., Cambiasso J., Marensi E., Fox A.M., Maier S.A., Sapienza R., Tartakovskii A.I. (2021) Bright single photon emitters with enhanced quantum efficiency in a two-dimensional semiconductor coupled with dielectric nano-antennas, *Nature Comm.* **12**, 6063.
12 Yang Y., Zenin V.A., Bozhevolnyi S.I. (2018) Anapole-assisted strong field enhancement in individual all-dielectric nanostructures, *ACS Photonics* **5**, 1960–1966.
13 Mignuzzi S., Vezzoli S., Horsley S.A., Barnes W.L., Maier S.A., Sapienza R. (2019) Nanoscale design of the local density of optical states, *Nano Lett.* **19**, 1613–1617.
14 Cao L., Fan P., Barnard E.S., Brown A.M., Brongersma M.L. (2010) Tuning the color of silicon nanostructures, *Nano Lett.* **10**, 2649–2654.
15 Celebrano M., Baselli M., Bollani M., Frigerio J., Bahgat Shehata A., Della Frera A., Tosi A., Farina A., Pezzoli F., Osmond J., Wu X., Hecht B., Sordan R., Chrastina D., Isella G., Duò L., Finazzi M., Biagioni P. (2015) Emission engineering in germanium nanoresonators, *ACS Photonics* **2**, 53–59.
16 Ee H.S., Kang J.H., Brongersma M.L., Seo M.K. (2015) Shape-dependent light scattering properties of subwavelength silicon nanoblocks, *Nano Lett.* **15**, 1759–1765.
17 Landreman P.E., Chalabi H., Park J., Brongersma M.L. (2016) Fabry-Perot description for Mie resonances of rectangular dielectric nanowire optical resonators, *Opt. Exp.* **24**, 29760–29772.
18 Frolov A.Y., Verellen N., Li J., Zheng X., Paddubrouskaya H., Denkova D., Shcherbakov M.R., Vandenbosch G.A.E., Panov V.I., Van Dorpe P., Fedyanin A.A., Moshchalkov V.V. (2017) Near-field mapping of optical Fabry-Perot modes in all-dielectric nanoantennas, *Nano Lett.* **17**, 7629–7637.
19 Córdova-Castro R.M., van Dam B., Lauri A., Maier S.A., Sapienza R., De Wilde Y., Izeddin I., Krachmalnicoff V. (2024) Single-emitter super-resolved imaging of radiative decay rate enhancement in dielectric gap nanoantennas, *Light Sci. App.* **13**, 7.
20 Bakker R.M., Permyakov D., Yu Y.F., Markovich D., Paniagua-Domínguez R., Gonzaga L., Samusev A., Kivshar Y., Luk'yanchuk B., Kuznetsov A.I. (2015) Magnetic and electric hotspots with silicon nanodimers, *Nano Lett.* **15**, 2137–2142.
21 Granchi N., Montanari M., Ristori A., Khoury M., Bouabdellaoui M., Barri C., Fagiani L., Gurioli M., Bollani M., Abbarchi M., Intonti F. (2021) Near-field hyper-spectral imaging of resonant Mie modes in a dielectric island, *APL Photonics* **6**, 126102.
22 Mignuzzi S., Mota M., Coenen T., Li Y., Mihai A.P., Petrov P.K., Oulton R.F.M., Maier S.A., Sapienza R. (2018) Energy-momentum cathodoluminescence spectroscopy of dielectric nanostructures, *ACS Photonics* **5**, 1381–1387.
23 Sapienza R., Coenen T., Renger J., Kuttge M., van Hulst N.F., Polman A. (2012) Deep-subwavelength imaging of the modal dispersion of light, *Nat. Mat.* **11**, 781–787.
24 Dang Z., Chen Y., Fang Z. (2023) Cathodoluminescence nanoscopy: state of the art and beyond, *ACS Nano* **17**, 24431–24448.
25 Coenen T., van de Groep J., Polman A. (2013) Resonant modes of single silicon nanocavities excited by electron irradiation, *ACS Nano.* **7**, 1689–1698.
26 Polman A., Kociak M., García de Abajo F.J. (2019) Electron-beam spectroscopy for nanophotonics, *Nat. Mat.* **18**, 1158–1171.
27 Dong Z., Mahfoud Z., Paniagua-Domínguez R., Wang H., Fernández-Domínguez A.I., Gorelik S., Ha S.T., Tjiptoharsono F., Kuznetsov A. I., Bosman M., Yang J.K.W. (2022) Nanoscale mapping of optically inaccessible bound-states-in-the-continuum, *Light Sci. App.* **11**, 20.
28 Frigerio J., Ballabio A., Isella G., Sakat E., Pellegrini G., Biagioni P., Bollani M., Napolitani E., Manganelli C., Virgilio M., Grupp A., Fischer M.P., Brida D., Gallacher K., Paul D.J., Baldassarre L., Calvani P., Giliberti V., Nucara A., Ortolani M. (2016) Tunability of the dielectric function of heavily doped germanium thin films for mid-infrared plasmonics, *Phys. Rev. B* **94**, 085202.
29 Auad Y., Hamon C., Tencé M., Lourenço-Martins H., Mkhitaryan V., Stéphan O., Garcia de Abajo F.J., Tizei L.H., Kociak M. (2022) Unveiling the coupling of single metallic nanoparticles to whispering-gallery microcavities, *Nano Lett.* **22**, 319–327.

J. Eur. Opt. Society-Rapid Publ. 2024, **20**, 20

https://doi.org/10.1051/jeos/2024016
Available online at: https://jeos.edpsciences.org

Special Issue - Plasmonica 2023
Antonino Foti and Attilio Zilli (Guest editors)

Journal of the European Optical Society-Rapid Publications

SHORT COMMUNICATION OPEN ACCESS

Photo-acoustic technique with widely tuneable laser: Metasurface circular dichroism response

Claudia Skubisz[1], Emilija Petronijevic[1,*], Grigore Leahu[1], Tiziana Cesca[2], Carlo Scian[2], Giovanni Mattei[2], Concita Sibilia[1], and Alessandro Belardini[1]

[1] Department SBAI, Sapienza University of Rome, Via Antonio Scarpa 14-16, 00161 Rome, Italy
[2] Department of Physics and Astronomy, University of Padova, Via Marzolo 8, I-35131 Padova, Italy

Received 1 March 2024 / Accepted 3 April 2024

Abstract. Chirality, an intrinsic property of certain entities in the universe, is characterized by the absence of mirror symmetry. Understanding chirality is crucial as it influences molecular interactions and properties. Circular dichroism (CD), measured using circularly polarized light, is a standard technique for probing chirality, but its sensitivity is often limited. Here, we explore extrinsic chirality (i.e. a property arising from asymmetric achiral materials when observed from out of normal incidence directions), using photo-acoustic spectroscopy (PAS). PAS allows direct measurement of local absorption, by monitoring the heat produced and transferred to the surrounding air, regardless the transmitted, reflected, and scattered light that flows away from the sample. In conventional techniques, the CD is usually measured by taking into account only the extinction as transmitted (or reflected) light. In this study, we introduce a new PAS setup that employs an oblique-incidence laser to study extrinsic chirality in silver-coated self-assembled metasurfaces. Our experimental results reveal intriguing CD trends dependent on the angle of incidence and wavelength, indicative of extrinsic chirality. This study expands the application of PAS, enabling simultaneous analysis of multiple wavelengths and providing valuable insights into chiral metasurfaces.

Keywords: Nanostructures, Extrinsic chirality, Photo-acoustic spectroscopy, Circular dichroism.

1 Introduction

Chirality is a fundamental property of some components of our universe, characterized by the absence of specular symmetry in an object [1]. A chiral object and its mirror image are called enantiomers and although they have the same physical constituents, this lack of specular symmetry influences the interaction of the enantiomer with the external world. Chirality is a common property of many molecules [2]. Circularly polarized light is conventionally used to probe the chirality of the sample; left and right circular polarizations (LCP and RCP, respectively) are absorbed differently, and this difference is defined as Circular Dichroism (CD) [3]. However, since the natural CD of chiral molecules is extremely low, conventional CD techniques are bulky and have low sensitivity. Fortunately, nanostructures can be designed to boost CD signal of chiral molecules [4, 5]. To obtain CD, nanostructures do not need to be chiral themselves: instead, chirality can be induced by combining the asymmetry of the sample and the optical set-up. This property is called extrinsic chirality and it is obtained by breaking the symmetry of the light-sample interaction by forming a non-planar triad of vectors between the light wave-vector, the normal of the sample's surface, and the vector of the sample's asymmetry [6, 7]. In reference [8], the chiral optical response was induced in 2-D mirror-symmetric nanostructures (trimers) by chosen heterogeneous material composition which breaks the symmetry of the system. In references [9, 10] similar geometries, but with magnetic materials allows the magnetic control of the induced CD. In our previous works, we measured extrinsic chirality with different conventional techniques such as extinction [11] and reflection [12]. However, to directly measure the absorption response, unconventional photothermal techniques can be applied [13–18].

Photo-acoustic spectroscopy (PAS) is a photothermal technique that exploits the interaction between an incident light beam and matter, inducing a non-radiative de-excitation process that generates heat [19]. When the light intensity is modulated over time, a sample confined in a sealed chamber filled with air undergoes alternating cycles of heating and cooling, resulting in air pressure variations. These fluctuations produce an acoustic signal, which is then converted into an electrical signal through a

* Corresponding author: emilija.petronijevic@uniroma1.it

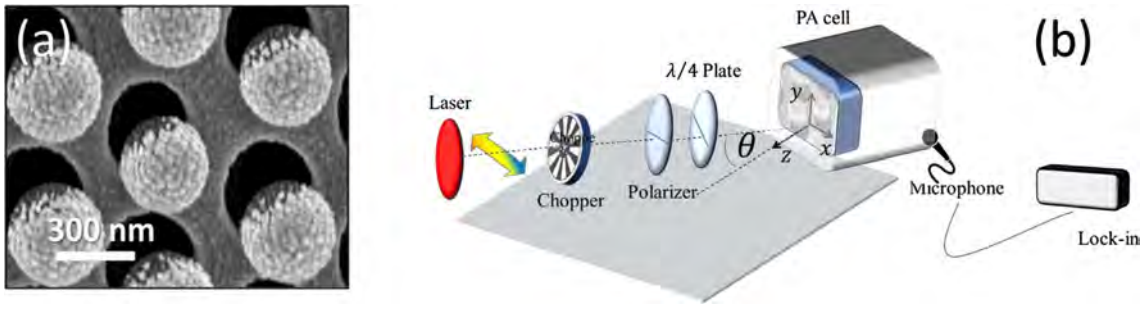

Fig. 1. (a) SEM image of the realized sample. (b) Schematic of the experimental set-up

sensitive microphone coupled with a lock-in amplifier. This approach enables direct measurement of local absorption, thereby detecting effects that might otherwise be obscured by other scattering-dependent techniques, such as the extinction measurements performed in transmission [8] or in reflection [19], were the far field signal can be related with the local absorption in a non trivial way, as described, for example, in reference [20]. To characterize CD, we previously used only single laser wavelengths to precisely define the incident polarization (LCP or RCP), and have high enough incident power with respect to usual lamp light.

In this study, we introduce a new PAS set-up, based on a widely tunable near-infrared laser excitation under oblique incidence. We use it to measure the absorption and the extrinsic chirality of low-cost self-assembled metasurfaces asymmetrically covered by silver. PAS applied at multiple wavelengths highlights the presence of extrinsic chirality, in good agreement with previous theoretical predictions.

2 Results and discussion

In Figure 1a, the scanning electron microscopy (SEM) image of the investigated sample is shown. The experimental arrangement utilized for the measurements (see Fig. 1b) comprises a laser that covers a spectral range from 680 nm to 1000 nm. The light emitted by the source undergoes modulation via a mechanical chopper operating at a fixed frequency of 81 Hz. Prior to reaching the sample housed within the photo-acoustic cell, the light beam traverses a polarizer and a quarter-wave plate. This setup allows for controlled polarization of the incident light. The photo-acoustic cell, where the sample is placed, is equipped with a rotating stage enabling examination of the sample at various angles of incidence (θ) relative to the normal surface.

For our specific study, the incidence angles employed span in the range of $\theta = \pm 30°$. The impinging light has a spot diameter of 1.2 mm and is polarized either with linear horizontal polarization (p-pol.) or RCP and LCP. The signal detected by the microphone preamplifier is fed into a lock-in amplifier, which analyzes the signal in correlation with the modulation frequency of the light source. To minimize the influence of scattered light on the microphone's signal reception from the sample, a narrow-diameter – labyrinthine tunnel is employed.

The primary component of the photo-acoustic cell is a movable quartz cylinder with two optically polished faces. By adjusting the position of this cylinder along the z-axis, the distance between the sample surface and the window can be optimized, thereby minimizing the cell volume to enhance signal detection. Simultaneously, transmitted light exits the cell through the quartz cylinder, contributing to noise reduction in the signal. The metasurface investigated consists of hexagonal unit cells with a pitch of 518 nm, containing polystyrene (PS) nanospheres measuring approximately 370 nm in diameter. The whole metasurface has a size of around 5 × 5 mm and was fabricated by nanosphere lithography [12, 13] onto a 0.3 mm glass substrate, and coated with a 55 nm thick layer of metallic silver (Ag) through thermal evaporation at a tilt angle of 45° relative to the sample surface. Due to the non-close packing arrangement of the 2D array, the metallic layer deposition resulted in the creation of a metallic grid on the substrate surface. The sample orientation in the PAS cell is fixed to follow the rules of extrinsic chirality: the projection of the Ag evaporation onto the sample surface is perpendicular to the plane of incidence.

Figure 2 illustrates the trends of the PAS signal for three different values of the angle $\theta = 0°$, $\theta = +15°$, and $\theta = -15°$. It can be observed how the absorption levels of the sample, at various angles of incidence, present linearly decreasing trends as the value of the wavelength increases. The absorption for a zero angle is very similar for different polarizations and slightly decreases with increasing wavelengths. The absorption levels for angles of $+15°$ and $-15°$ exhibit larger oscillations and present a pronounced difference between circular polarizations. Several significant findings emerge from the obtained results. Firstly, CD measurements conducted with respect to the angle of incidence reveal intriguing trends. Figure 3 shows that for wavelengths longer than 800 nm, the CD gradually increases from 0% at normal incidence, to positive values for positive angles of incidence, and changing to negative values as the incidence angles become more negative. This phenomenon, indicative of a sign reversal, is a characteristic feature of extrinsic chirality. Moreover, an interesting observation is noted concerning wavelengths at 800 nm in Figure 3, where all CD trends converge to a value of 0%, suggesting a unique behavior of the sample at this specific wavelength. For wavelengths shorter than 800 nm the process is reversed. Additionally, the sample demonstrates a remarkable rapid variation in CD across a broad range of angles. This dynamic response

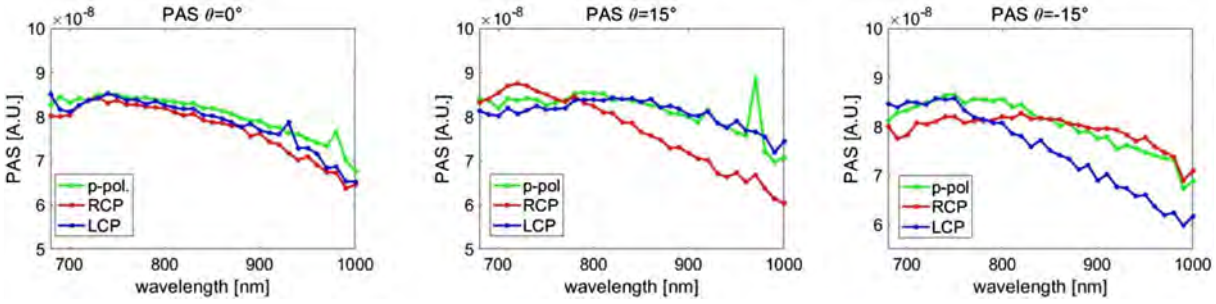

Fig. 2. Absorption level trends of the sample for various angles of incidence θ.

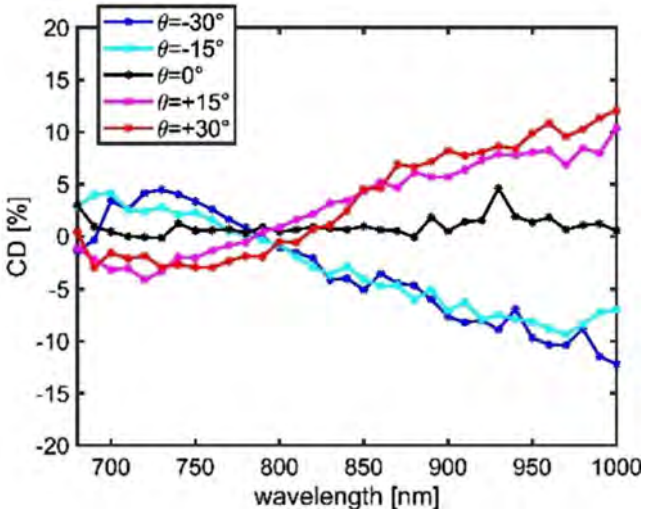

Fig. 3. CD dependence on the angle of incidence for the sample.

underscores the intricate nature of the sample's chirality under varying conditions of angle of incidence.

3 Conclusions

In conclusion, in this work, we have presented the CD behavior of metasurfaces made of polystyrene nanospheres asymmetrically coated with Ag. The metasurface was created by nanosphere lithography on soda-lime glass substrates and inclined evaporation of the metal. An extrinsic chiral response is detected as CD dependence on the angle of incidence of the input beam and the maximum CD is observed for a θ angle of incidence equal to 30°.

Although photo-acoustic has been a widely used technique in the past, it is important to point out that its application was generally limited to the selection of a single color. However, through the use of current technique, we are now able to significantly extend the potential of photo-acoustic, allowing the analysis and selection of multiple wavelengths simultaneously.

Acknowledgments

A.B. acknowledges LASAFEM Sapienza Università di Roma Infrastructure Project No. MA31715C8215A268 and Sapienza Large Research Project 2022 No. RG1221816B6FA2E9. E.P. acknowledges the RTDa–PON "ricerca e innovazione" 2014–2020 for financial and mobility support. We acknowledge M. Magi for technical support. T.C. acknowledges the financial support of the Physics and Astronomy Department through the project PRD-BIRD2022-Cesca. C. Skubisz ackowledges PNRR MUR project PE0000023-NQSTI.

Funding

This research received no external funding.

Conflicts of interest

The authors declare no conflict of interest.

Data availability statement

Data obtained in this work are not publicly available at this time but may be obtained from the authors upon reasonable request.

Author contribution statement

Conceptualization, E.P. and A.B.; methodology, E.P., G.L., A.B., and C. Sibilia; software, C. Skubisz and A.B.; fabrication, T.C, C. Scian and G. Mattei; measurements, E. P. and C. Skubisz; validation, A.B.; writing – original draft preparation, C. Skubisz; writing – review and editing, E.P. and A.B.

References

1 Kelvin L. (1894) *The molecular tactics of a crystal*, Clarendon Press, Oxford.
2 Hutt A.J., Tan S.C. (1996) Drug chirality and its clinical significance, *Drugs* **52**, 1–12.
3 Goerlitzer E.S.A., Puri A.S., Moses J.J., Poulikakos L.V., Vogel N. (2021) The beginner's guide to chiral plasmonics: mostly harmless theory and the design of large-area substrates, *Adv. Optical Mater.* **9**, 2100378.
4 Zhao Y., Askarpour A.N., Sun L., Shi J., Li X., Alù A. (2017) Chirality detection of enantiomers using twisted optical metamaterials, *Nat. Commun.* **8**, 14180.
5 Solomon M.L., Abendroth J.M., Poulikakos L.V., Hu J., Dionne J.A. (2020) Fluorescence-detected circular dichroism of a chiral molecular monolayer with dielectric metasurfaces, *J. Am. Chem. Soc.* **142**, 18304–18309.
6 Plum E., Liu X.-X., Fedotov V.A., Chen Y., Tsai D.P., Zheludev N.I. (2009) Metamaterials: optical activity without chirality, *Phys. Rev. Lett.* **102**, 113902.

7 De Leon I., Horton M.J., Schulz S.A., Upham J., Banzer P., Boyd R.W. (2015) Strong, spectrally-tunable chirality in diffractive metasurfaces, *Sci. Rep.* **5**, 13034.

8 Banzer P., Woźniak P., Mick U., De Leon I., Boyd R.W. (2016) Chiral optical response of planar and symmetric nanotrimers enabled by heteromaterial selection, *Nat Commun* **7**, 13117.

9 Zubritskaya I., Maccaferri N.Inchausti Ezeiza X., Vavassori P., Dmitrie A. (2018) Magnetic control of the chiroptical plasmonic surfaces, *Nano Lett.* **18**, 1, 302–307.

10 Petrucci G., Gabbani A., Faniayeu I., Pedrueza-Villalmanzo E., Cucinotta G., Atzori M., Dmitriev A., Pineider F. (21 June 2021,) Macroscopic magneto-chiroptical metasurfaces, *Appl. Phys. Lett.* **118**, 25, 251108.

11 Petronijevic E., Belardini A., Cesca T., Scian C., Mattei G., Sibilia C. (2021) Rich near-infrared chiral behavior in diffractive metasurfaces, *Phys. Rev. Applied* **16**, 014003.

12 Petronijevic E., Belardini A., Leahu G., Hakkarainen T., Piton M.R., Koivusalo E., Sibilia C. (2021) Broadband optical spin dependent reflection in self-assembled GaAs-based nanowires asymmetrically hybridized with Au, *Sci Rep.* **11**, 4316.

13 Spaeth P., Adhikari S., Le L., Jollans T., Pud S., Albrecht W., Bauer T., Caldarola M., Kuipers L., Orrit M. (2019) Circular dichroism measurement of single metal nanoparticles using photothermal imaging, *Nano Lett.* **19**, 12, 8934–8940.

14 Spaeth P., Adhikari S., Dieter Baaske M., Pud S., Ton J., Orrit M. (2021) Photothermal circular dichroism of single nanoparticles rejecting linear dichroism by dual modulation, *ACS Nano* **15**, 10, 16277–16285.

15 Leahu G., Petronijevic E., Li Voti R., Belardini A., Cesca T., Mattei G., Sibilia C. (2021) Diffracted beams from metasurfaces: high chiral detectivity by photothermal deflection technique, *Adv. Optical Mater.* **9**, 2100670.

16 Petronijevic E., Leahu G., Li Voti R., Belardini A., Scian C., Michieli N., Cesca T., Mattei G., Sibilia C. (2019) Photoacoustic detection of chirality in metal-polystyrene metasurfaces, *Appl. Phys. Lett.* **114**, 053101.

17 Leahu G., Petronijevic E., Belardini A., Centini M., Sibilia C., Hakkarainen T., Koivusalo E., Rizzo Piton M., Suomalainen S., Guina M. (2017) Evidence of optical circular dichroism in GaAs-based nanowires partially covered with gold, *Adv. Opt. Mater.* **5**, 1601063.

18 Petronijevic E., Leahu G., Belardini A., Centini M., Li Voti R., Hakkarainen T., Koivusalo E., Guina M., Sibilia C. (2018) Resonant absorption in GaAs-based nanowires by means of photo-acoustic spectroscopy, *Int. J. Thermophys.* **39**, 45.

19 Belardini A., Centini M., Leahu G., Hooper D.C., Li Voti R., Fazio E., Haus J.W., Sarangan A., Valev V.K., Sibilia C. (2016) Chiral light intrinsically couples to extrinsic/pseudo-chiral metasurfaces made of tilted gold nanowires, *Sci. Rep.* **6**, 31796.

20 Najafabadi A.F., Pakizeh T. (2017) Analytical chiroptics of the 2D and 3D nanoantennas, *ACS Photonics* **4**, 6, 1447–1452.

J. Eur. Opt. Society-Rapid Publ. 2025, **21**, 49

https://doi.org/10.1051/jeos/2025048
Available online at: https://jeos.edpsciences.org

Journal of the European Optical Society-Rapid Publications

PLASMONICA Collection
Nicoletta Granchi and Antonino Foti (Guest Editors)

SHORT COMMUNICATION OPEN ACCESS

Photo-acoustic spectroscopy detects nanostructures against resonant and absorbing substrates

Emilija Petronijevic[1,*], Hanan Ali[2], Sonia Freddi[3], Luca Anzi[4], Roman Sordan[4], Monica Bollani[3], Lucio Claudio Andreani[2], and Alessandro Belardini[1]

[1] Sapienza University of Rome, Department SBAI, Rome, 00161, Italy
[2] Physics Department "A. Volta", University of Pavia, via Bassi 6, Pavia 27100, Italy
[3] Institute of Photonic and Nanotechnology (IFN) – Consiglio Nazionale delle Ricerche (CNR), LNESS Laboratory, Como, Italy
[4] Department of Physics, Politecnico di Milano, Milano, Italy

Received 6 October 2025 / Accepted 20 November 2025

Abstract. Photo-acoustic spectroscopy is a powerful photo-thermal method for scattering-free, contactless and non-destructive measurements of absorption. In plasmonics and nano-photonics, it allows for characterization of light-matter interactions leading to non-radiative relaxation processes, which generate heat. Here, we address the issue of detecting absorption signal of periodically nanostructured layer of gold, sitting on a commercial, absorbing substrate. The nanostructured plasmonic layer alone exhibits resonant peaks in the near-infrared range due to a 2D array of elliptical nanoholes in Au. The substrate itself has cavity interference resonances in the same range, due to a layer of Si_3N_4 on Si wafer. Conventional optical techniques are influenced by scattering, which complicates the characterization of the nanostructures' absorption against the properties of the substrate. We apply photo-acoustic technique with a widely tunable laser source to measure the absorption spectra of these geometries, as well as on an Au-covered substrate without nanoholes and on a bare Si substrate. A microscope enabled us to differentiate the nanohole response from its surroundings, while the tunable modulation frequency allowed for studying different absorption depths. Complementary optical simulations reveal the spatial distribution of absorption, in good agreement with experimental results. A major potential of the proposed approach lies in monitoring and discriminating nanoscale structural changes in thin absorbing layers against the strongly absorbing substrate background, which is of great importance in situations involving sensing of low quantity of absorbing material placed on commercial wafers. Moreover, besides resonant plasmonic effects, this photo-acoustic set-up and modelling can be further adapted to study light coupling with plasmonic nanohole arrays in terms of incident light angle of incidence and polarization.

Keywords: Photo-acoustic spectroscopy, Plasmonics, Nanohole, Absorption.

Introduction

Absorbing materials convert absorbed electromagnetic wave energy into heat via non-radiative deexcitation, giving rise to photo-thermal effect. Photo-thermal techniques such as photo-acoustic [1–5], thermal lens [6–8] and photo- deflection [9] spectroscopies study various consequences of absorption-induced heating, allowing for non-destructive, contactless, sensitive and non-invasive characterization of optical and thermal properties of matter. In particular, photo-acoustic effect emerges when a material absorbs a modulated electromagnetic wave, heats up and cools down in cycles, and, consequently, creates a pressure wave, i.e., acoustic signal [10]. When the absorbing medium is closed in a photo-acoustic cell, the acoustic signal phase and amplitude can be caught by a microphone at the modulation frequency, without any direct influence of the scattered light. This potentially allows for direct, scattering-free, sensitive, and low-cost measurement of spectral absorption properties of thin films and nanostructured surfaces, of great importance in modern plasmonics and nano-photonics.

Photo-acoustic spectroscopy (PAS) is efficiently applied to study optical properties of plasmonic nanostructures on transparent glass substrates: in ref. [11] it revealed plasmon-mediated absorption in a 2D array of nanoholes in Au, while in ref. [11] we reported on extrinsic chiral behavior of asymmetric Ag semishells. Issues arise in more complex environments – when nanostructures are grown on strongly absorbing or resonant substrates, where the resonant absorption of a thin nanostructured layer can be masked by the strong background PAS signal arising from the substrate. We previously solved this issue by increasing

* Corresponding author: emilija.petronijevic@uniroma1.it

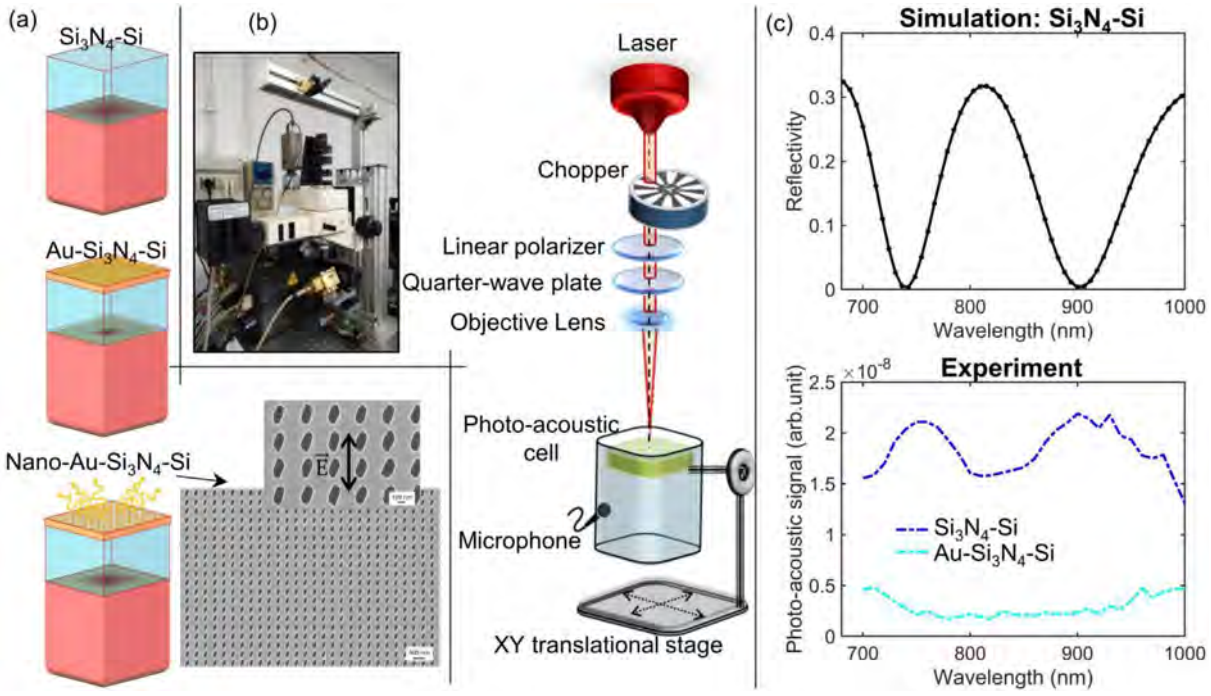

Figure 1. (a) Samples investigated are Si_3N_4–Si (Si substrate with 1,022 Si_3N_4), Au–Si_3N_4–Si (60 nm Au on the top of Si_3N_4–Si), and Nano-Au–Si_3N_4–Si (elliptical nanohole array fabricated in Au on Si_3N_4–Si). (b) Photo-acoustic spectroscopy set-up, enriched with a microscope, allows for independent tuning of parameters: polarization, power, modulation frequency, excitation beam diameter and position; inset: photograph of the set-up. (c) Simulations and raw PAS amplitude spectra measured at 81 Hz for Si_3N_4–Si and Au–Si_3N_4–Si: measured absorption peaks well agree with the calculated reflectivity dips.

the light modulation frequency f, as the thermal diffusion length scales with $1/\sqrt{f}$: contribution of the nanostructured upper part of the sample to the PAS absorption signal increases with the increase of f. In ref. [13] we studied ~5 μm tall GaAs nanowires grown on Si, which couple light to strongly absorbing, resonant leaky waveguide modes. These modes were detected by increasing f from 25 Hz to 225 Hz. However, the overall PAS amplitude decreases with the increase of f [14, 15], hence modern PAS set-ups require the power tunability of the excitation light beam.

In this work, we explore the potential of widely tunable PAS to study the absorption properties of plasmonic nanostructures on absorbing and strongly resonant substrates. First, we consider a commercial Si–Si_3N_4 substrate, where ~1 μm of Si_3N_4 forms a cavity with interference resonances in the near-infrared range. Next, we investigate the same substrate covered by a layer of Au, which dramatically decreases the absorption. Finally, we pattern Au into a 2D array of nanoholes and analyze the absorption differences with respect to the substrate exploiting PAS microscopy. We further employ optical numerical simulations to relate the electromagnetic behavior to the measured photo-thermal properties.

Material and methods

Figure 1a shows sketches of the three samples investigated. The first sample is a commercial substrate where Si is covered with 1,022 nm of Si_3N_4, i.e., Si_3N_4–Si, deposited by plasma enhanced chemical vapour deposition. The second sample has 60 nm of Au on the top of Si_3N_4–Si, i.e., Au–Si_3N_4–Si. The nanostructured sample, Nano-Au–Si_3N_4–Si, is a 100 × 100 μm^2 area of elliptical nanoholes in Au, fabricated by electron beam lithography (EBL). In detail, a negative resist (AN 7520.07) has been spincoated on a Si_3N_4–Si substrate, and elliptical nanoholes have been patterned, with a periodicity of 400 nm. After development, 60 nm of Au has evaporated. A thin layer of Ti (5 nm) was used for better adhesion of Au to Si_3N_4. After the lift-off process, performed in acetone for 60 h, the 2D array has been characterized by Scanning electron microscope (SEM), which a representative image can be seen in the inset; the black arrow represents the incidence polarization of the excitation under normal incidence. Figure 1b shows the photo-acoustic set-up positioned on a translation stage under normal incidence. It allows for tunable wavelength in the (680–1,000) nm range (including tunable power), tunable chopper frequency (up to 1,600Hz), and the precise adjustment of the laser position and focus by a microscope, as shown in the inset. In this work, the light is focused to 70 μm diameter. To gain "optical" insight into the absorption distribution in the investigated geometries, we further employ a commercial 3D electromagnetic solver based on finite-difference-time domain by Lumerical [16]. Nanoholes are modelled by including their ellipticity (major and minor axes diameters of 280 nm and 140 nm), and an in-plane tilt of 20°. Figure 1c shows great agreement between the

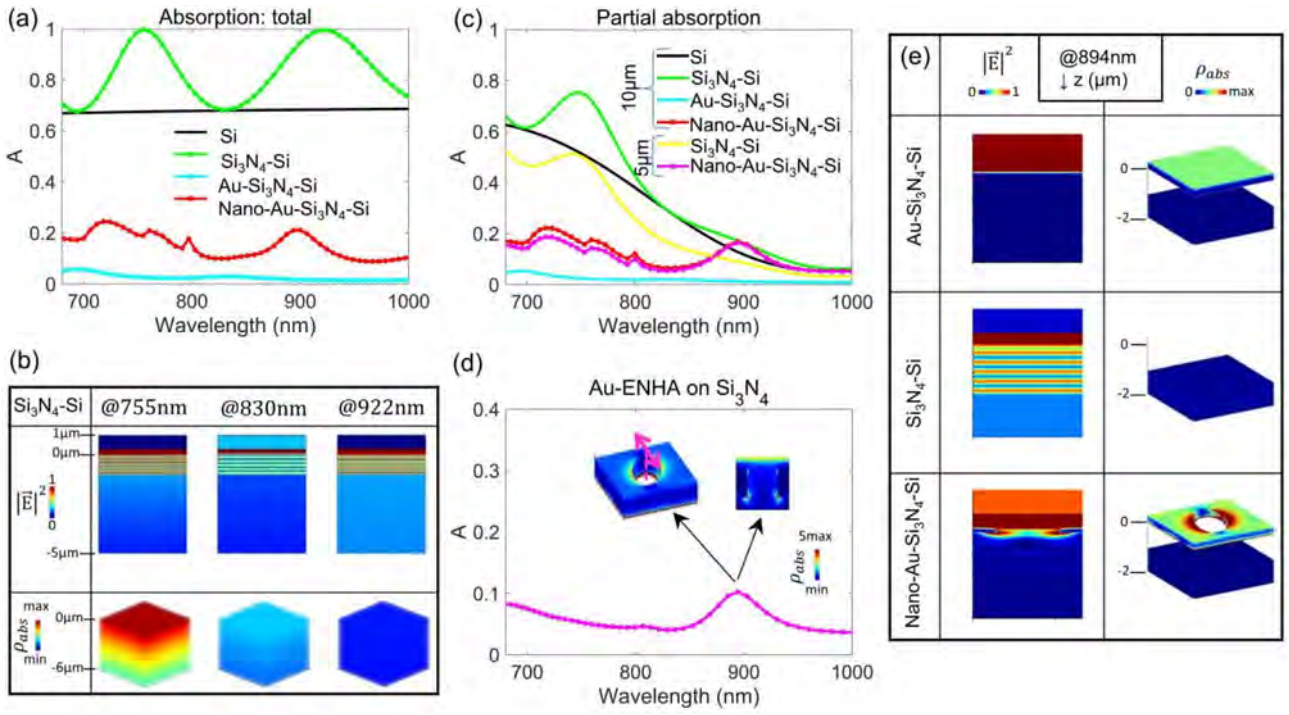

Figure 2. (a) Total absorption calculated as 1-reflectivity shows resonant modes in Si_3N_4–Si and overall lower absorption in the nanostructured sample. (b) Distribution of electric field intensity and absorption density in Si_3N_4–Si strongly depends on Si behavior at cavity resonant wavelengths. (c) Partial absorption is calculated by integrating absorption density over first 5 μm or 10 μm of Si in Si and Si_3N_4–Si, and adding the Au part for Au–Si_3N_4–Si and Nano-Au–Si_3N_4–Si. (d) Total absorption of Au ENHA on Si_3N_4 shows resonant absorption peak at 894 nm. (e) Electric field intensity and absorption density in the first 2 μm of depth of the three samples.

reflectivity dips of the simulated Si_3N_4–Si with the PAS absorption peaks measured in the same sample. These initial measurements were performed at 81 Hz, and the raw PAS amplitude was normalized to the incident laser power. In comparison, the Au–Si_3N_4–Si sample showed very low absorption, as expected due to its high reflectivity. For further normalization, we also measured PAS signal from 600 μm Si wafer.

Results and discussion

Where does the absorption take place at different wavelengths in geometries using Si_3N_4–Si as a substrate? As none of the incident power gets transmitted by our samples in the (680–1,000) nm investigated wavelength range, we first calculate the total absorption as 1-reflectivity. Figure 2a shows the resonant absorption peaks in the Si_3N_4–Si compared to a bare Si substrate, Nano-Au–Si_3N_4–Si overall absorbs less than Si_3N_4–Si due to large scattering. As expected, with respect to Au–Si_3N_4–Si the nanostructuring leads to the absorption enhancement. Figure 2b shows the confinement of the electric field intensity and absorption density at absorption peaks and dip wavelengths in Si_3N_4–Si; 0 μm is the upper boundary of Si_3N_4, while the excitation comes from the top with the source position at 300 nm. At the two absorption peak wavelengths, electric field is strongly confined in Si_3N_4, and reflection is suppressed. However, the Si absorption depth increases more than 5 times from 755 nm to 922 nm, leading to very different absorption density distribution in the first 5 μm of propagation. We further integrate the absorption density over the volumes including first 10 μm or 5 μm of Si below Si_3N_4, including the nanostructured Au on the top, Figure 3c. Around 900 nm, the absorption of Nano-Au–Si_3N_4–Si does not depend on the volume of Si included, suggesting that the total absorbed signal comes from the nanostructured part involving 5/60 nm of Ti/Au. In this range, Nano-Au–Si_3N_4–Si has a absorption higher than its substrate for 5 μm of depth. To check the influence of the Si_3N_4–Si background, we next investigate the optical properties of the elliptic nanohole array (ENHA) of the same geometric parameters on Si_3N_4, Figure 2d. At 894 nm, there is plasmonic resonant absorption peak resulting in confinement of the field between the ENHA and the substrate. We next visualize the electromagnetic distribution in the three samples at this wavelength, in the space from 1 μm above until 1 μm below Si_3N_4 layer, Figure 2e. Au–Si_3N_4–Si has negligible absorption on the Au border, while Si_3N_4–Si requires larger distances to absorb the wave. Finally, Nano-Au–Si_3N_4–Si confines the field on the plasmonic part, leading to an enhanced absorption [17].

We next employ PAS to characterize absorption in Si, Si_3N_4–Si and Nano-Au–Si_3N_4–Si at 54 Hz and 408 Hz.

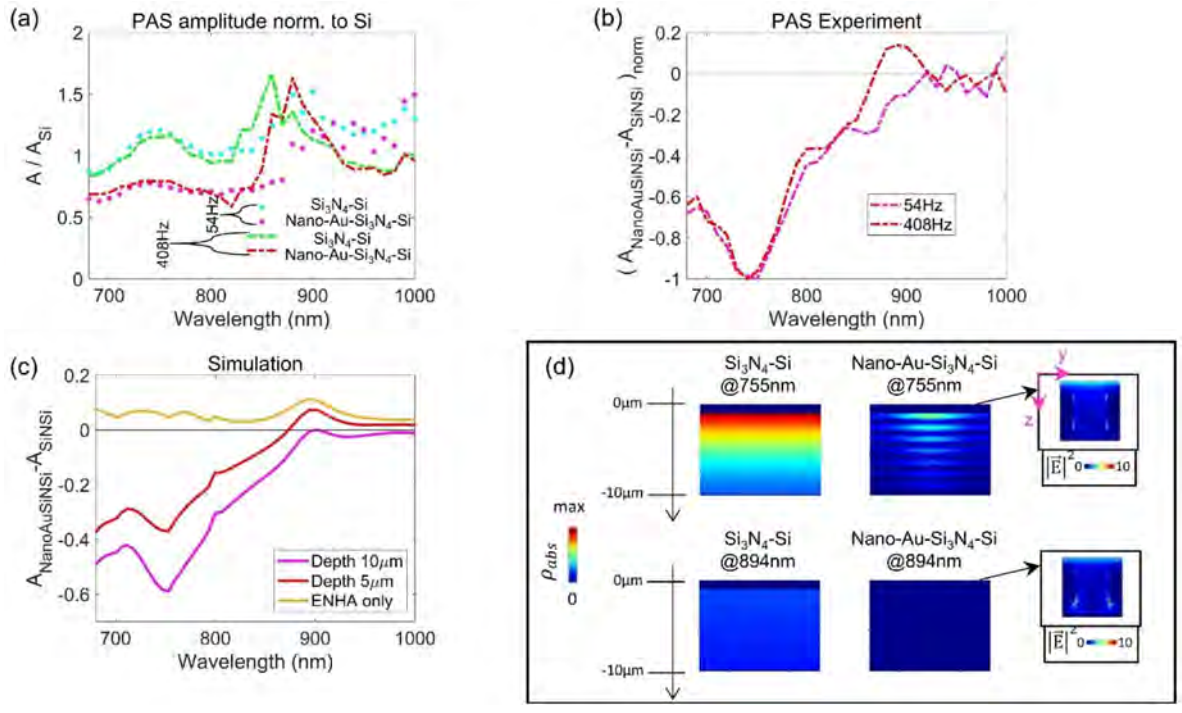

Figure 3. (a) Photo-acoustic spectra of Si_3N_4–Si and Nano-Au–Si_3N_4–Si at 54 Hz and 408 Hz, normalized to the bare Si spectra obtained at the same frequencies. (b) Experimental absorption difference between Nano-Au–Si_3N_4–Si and Si_3N_4–Si, normalized to maximum, at 54 Hz and 408 Hz. (c) Simulations of absorption differences between Nano-Au–Si_3N_4–Si and Si_3N_4–Si, where the partical absorption was integrated in over 10 μm or 5 μm of Si depth and including the upper plasmonic layers for the nanostructured sample. (d) Absorption confinement differences between Nano-Au–Si_3N_4–Si and the substrate over first 10 μm of depth, at the absorption difference dip at 755 nm and peak at 894 nm. Insets plot the electric field intensity around nanohole.

Figure 3a shows PAS signals normalized to Si at the corresponding wavelengths. For Si_3N_4–Si, at both modulation frequencies absorption peaks with respect to Si following cavity resonant behavior. At 54 Hz, Nano-Au–Si_3N_4–Si is lower than the Si_3N_4–Si at almost all wavelengths. At 408 Hz, however, absorption is greater than that of Si and Si_3N_4–Si around 900 nm. We further focus on the absorption difference between the nanostructure and its substrate. Figure 3b plots spectra of PAS signal difference between Nano-Au–Si_3N_4–Si and Si_3N_4–Si, normalized to its maximum: $(A_{NanoAuSi3N4Si}–A_{Si3N4Si})_{norm} = (A_{NanoAuSi3N4Si}–A_{Si3N4Si}) \;/\; |max(A_{NanoAuSi3N4Si}–A_{Si3N4Si})|$. Although PAS signal strongly decreases in amplitude from 54 Hz to 408 Hz, and the total absorption of Nano-Au–Si_3N_4–Si around 900 nm is less than 20%, PAS is able to monitor spectral behavior of this difference. Optical simulations of this difference show great agreement with PAS when the partial absorption includes first 5 μm of Si below Si_3N_4 in both samples, Figure 3c. We finally plot the absorption density yz cross-section from the top until 10 μm of depth, Figure 3d. At 755 nm, strong substrate resonance leads to larger absorption with respect to Nano-Au–Si_3N_4–Si, while the absorption of the latter comes from both nanostructured part on the top, and Si, as seen from the periodic pattern decreasing in intensity. At 894 nm, all of the nanostructured absorption is confined in the plasmonic array, overcoming the Si absorption in the Si_3N_4–Si case.

Conclusion

We have employed photo-acoustic spectroscopy and optical simulations to study absorption properties of nanostructures standing on resonant and absorbing substrates. Photo-acoustic signals were studied at low and high modulation frequencies to enhance the nanostructured layer contribution to the total PAS signal. Numerical investigation of absorption density at different substrate depths shows the importance of knowing the substrate behavior in detail, before the PAS modulation frequency gets tuned to access upper volumes of the sample. The differences between the nanostructured part and the substrate in the experiment agrees well with the absorption simulations in 5–10 μm. Further modelling of thermal responses, including different thermal boundaries, would be required to directly connect f with thermal diffusion length in nanostructured sample. In conclusion, PAS with multiple tunable parameters and a microscope can be used to study absorption in arrays of elliptical nanoholes, theoretically proposed for strong planar chirality [18, 19].

Acknowledgments

Alessandro Belardini and Emilija Petronijevic acknowledge LASAFEM Sapienza Università di Roma Infrastructure Project 2017 n. MA31715C8215A268 and PRIN 2022 PNRR Project INSPIRE n. P2022LETN5 founded by the European

Union – NextGenerationEU. Emilija Petronijevic acknowledges Sapienza Università di Roma project "Progetti di Ricerca Medi 2023 – n. protocollo RM123188F1CB517D" for supporting the collaboration. Sonia Freddi and Monica Bollani acknowledge Polifab, the micro and nanofabrication facility of Politecnico di Milano, for supporting the devices nanofabrication. L.A. acknowledges MUSA – Multilayered Urban Sustainability Action project, funded by the European Union – NextGenerationEU.

Funding

This research received no external funding.

Conflicts of interest

The authors have nothing to disclose.

Data availability statement

Data obtained in this work are not publicly available at this time but may be obtained from the authors upon reasonable request.

Author contribution statement

Conceptualization, E.P., L.C.A. and H.A.; Methodology, M.B., L. C.A. and A.B.; Software, E.P. and S.F.; Validation, A.B., L.C.A., M.B.; Formal Analysis, E.P. and L.C.A.; Investigation, E.P., H.A., S.F., L.A., R.S.; Resources, A.B.; Data Curation, E.P. and S.F.; Writing – Original Draft Preparation, E. P.; Writing – Review & Editing, A.B., S.F., M.B., L.A. and R.S.; Visualization, E.P. and S.F.; Supervision, M.B., R.S., L.C.A. and A.B.

References

1 Park T, Kim J, Ko R, Yoo H, Light in, sound keys out: photoacoustic PUFs from stochastic nanocomposites, Nat. Commun. 16, 7323 (2025). https://doi.org/10.1038/s41467–025-62747–1.
2 Park B, Oh D, Kim J, Kim C, Functional photoacoustic imaging: from nano- and micro- to macro-scale, Nano Converg. 10, 29 (2023). https://doi.org/10.1186/s40580–023-00377–3.
3 Zelewski SJ, Zhou Z, Li F, Kang X, Meng Y, Ho JC, Kudrawiec R. Optical properties of In2xGa2–2xO3 nanowires revealed by photoacoustic spectroscopy, ACS Appl. Mater Interfaces. 11(21), 19260–19266 (2019). https://doi.org/10.1021/acsami.9b00756.
4 González-Borrero PP, Sato F, Medina AN, Baesso ML, Bento AC, Baldissera G, Persson C, Niklasson GA, Granqvist CG, Ferreira da Silva A, Optical band-gap determination of nanostructured WO3 film, Appl. Phys. Lett. 96, 061909 (2010). https://doi.org/10.1063/1.3313945.
5 Fogaça LZ, Jean César Marinozi Vicentini JC, De Freitas CF, Braga TL, Da Silva FA, De Souza M, Baesso ML, Caetano W, Batistela VR, Scaliante MHNO, Nanocomposites of Nb2O5 and ZnO with reduced graphene oxide for heterogeneous photocatalysis of dyes, Catal. Commun. 185, 106799, 1566–7367 (2023). https://doi.org/10.1016/j.catcom.2023.106799.
6 Swapna M.S, Sankararaman S, Korte D, Thermal lens and photoacoustics as potential tools for nanomaterial characterization: a review, J. Mater. Sci. 59, 10140–10168 (2024). https://doi.org/10.1007/s10853–024-09773–4.
7 Spaeth P, Adhikari S, Le L, Jollans T, Pud S, Albrecht W, Bauer T, Caldarola M, Kuipers L, Orrit M, Circular dichroism measurement of single metal nanoparticles using photothermal imaging, Nano Lett. 19(12), 8934–8940 (2019). https://doi.org/10.1021/acs.nanolett.9b03853.
8 Spaeth P, Adhikari S, Dieter Baaske M, Pud S, Ton J, Orrit M, Photothermal circular dichroism of single nanoparticles rejecting linear dichroism by dual modulation, ACS Nano 15(10), 16277–16285 (2021). https://doi.org/10.1021/acsnano.1c05374.
9 Leahu G, Petronijevic E, Li Voti R, Belardini A, Cesca T, Mattei G, Sibilia C, Diffracted beams from metasurfaces: high chiral detectivity by photothermal deflection technique, Adv. Optical Mater. 9, 2100670 (2021). https://doi.org/10.1002/adom.202100670.
10 Galovic SP, Djordjevic KLj, Nesic MV, Popovic MN, Markushev DD, Markushev DK, Todorovic DM, Time-domain minimum-volume cell photoacoustic of thin semiconductor layer. I. Theory, J. Appl. Phys. 133, 245701 (2023). https://doi.org/10.1063/5.0152519.
11 Petronijevic E, Leahu G, Mussi V, Sibilia C, Bovino AF, Photoacoustic technique for the characterization of plasmonic properties of 2D periodic arrays of gold nanoholes, AIP Adv. 7(2), 025210 (2017). https://doi.org/10.1063/1.4977545.
12 Skubisz C, Petronijevic E, Leahu G, Cesca T, Scian C, Mattei G, Sibilia C, Belardini A, Photo-acoustic technique with widely tuneable laser: metasurface circular dichroism response, J. Eur. Opt. Soc.-Rapid Publ. 20, 1 (2024). https://doi.org/10.1051/jeos/2024016.
13 Petronijevic E, Leahu G, Belardini A, Centini M, Li Voti R, Hakkarainen T, Koivusalo E, Guina M, Sibilia C, Resonant absorption in GaAs-based nanowires by means of photoacoustic spectroscopy, Int. J. Thermophys. 39, 45 (2018). https://doi.org/10.1007/s10765–018-2365–4.
14 Markushev DD; Ordonez-Miranda J, Rabasović MD, Galović S, Todorović DM, Bialkowski SE, Effect of the absorption coefficient of aluminium plates on their thermoelastic bending in photoacoustic experiments, J. Appl. Phys. 117, 245309 (2015). https://doi.org/10.1063/1.4922718.
15 Petronijevic E, Leahu G, Skubisz C, Li Voti R, Sibilia C, Belardini A, Listening to nanostructures' absorption with many degrees of freedom: widely tunable photo-acoustic characterization, Eur. Phys. J. Plus. 140(7), 140–613 (2025). https://doi.org/10.1140/epjp/s13360–025-06578–5.
16 Lumerical Solutions, Inc. http://www.lumerical.com/tcad-products/fdtd/.
17 Spevak IS, Nikitin AY, Bezuglyi EV, Levchenko A, Kats, AV, Resonantly suppressed transmission and anomalously enhanced light absorption in periodically modulated ultrathin metal films, Phys. Rev. B. 79, 161406 (2009). https://doi.org/10.1103/PhysRevB.79.161406.
18 Lin Z-H, Zhang J, Huang J-S, Plasmonic elliptical nanoholes for chiroptical analysis and enantioselective optical trapping, Nanoscale. 13(20), 9185–9192 (2021). https://doi.org/10.1039/D0NR09080H.
19 Ali H, Petronijevic E, Pellegrini G, Sibilia C, Andreani L C, Circular dichroism in a plasmonic array of elliptical nanoholes with square lattice, Opt. Express. 31(9), 14196–14211 (2023). https://doi.org/10.1364/OE.485324.

J. Eur. Opt. Society-Rapid Publ. 2024, **20**, 15
© The Author(s), published by EDP Sciences, 2024
https://doi.org/10.1051/jeos/2024015
Available online at: https://jeos.edpsciences.org

Special Issue - Plasmonica 2023
Antonino Foti and Attilio Zilli (Guest editors)

Journal of the European Optical Society-Rapid Publications

RESEARCH ARTICLE OPEN ACCESS

Polarization-resolved surface-enhanced infrared spectra with nanosensors based on self-organized gold nanorods

Raffaella Polito[1,*], S. Sotgiu[1], F. Sohrabi[2], G. Ferrando[3], F. Berkmann[1], M. E. Temperini[1,2], V. Giliberti[2], F. Buatier de Mongeot[3], M. Ortolani[1], L. Baldassarre[1], and M.C. Giordano[3]

[1] Department of Physics, Sapienza University of Rome, P.le A. Moro 2, I-00185 Rome, Italy
[2] Center for Life Nano-Science, Istituto Italiano di Tecnologia, Viale Regina Elena 291, I-00161 Rome, Italy
[3] Dipartimento di Fisica, Università degli Studi di Genova, Via Dodecaneso 33, I-16146 Genova, Italy

Received 31 January 2024 / Accepted 28 March 2024

Abstract. Biosensors are becoming ubiquitous in the study of biomolecules, as, by modifying shape size and environment of metallic nanostructures it is now possible to engineer the field so to monitor subtle transient changes in molecular conformation at the level of a single biolayer. In this paper, we present a first step towards a polarization-resolved study of light-induced conformational changes of transmembrane proteins. We exploit a platform of self-organized gold nanorods on SiO_2 substrates to enhance the infrared reflection absorption spectroscopy and to perform difference spectroscopy (*i.e.*, spectrum under visible light ON minus spectrum under visible light OFF) on a light-sensitive transmembrane protein with simultaneous visible light illumination from the backside of the chip. The broad size distribution of nanorods allows us to probe with high sensitivity the modifications of the vibrational peaks over the entire fingerprint region. We show that it is possible to identify dissimilarities in the difference spectra, which in turn implies that we are monitoring over a broadband spectrum not only the chemical bonds with the dipole moment aligned orthogonally to our substrate/nanorod surface but also those with different orientation.

Keywords: Self-organized nanoantennas, IR sensing, IRRAS, Near-field IR nanospectroscopy.

1 Introduction

Biosensors for the detection and the study of thin biolayers hold great promise for applications in biotechnology, medical research, clinical diagnostics, and pharmaceutical sciences [1–4]. A great scientific and technological challenge is to design a biosensor capable of monitoring real-time functional modifications of an extremely low number of proteins triggered by external perturbations that could allow a deep understanding of protein conformational changes underlaying the biological functional reaction steps [5, 6].

Of particular interest is the study of transmembrane proteins, *i.e.*, proteins spanning across the cell membrane that are often targeted for drug delivery [7].

With its high accuracy in monitoring frequency-dependent modification in chemical bonds, mid-Infrared (mid-IR) spectroscopy (2–20 μm in wavelength) is the technique of choice for characterizing transient protein conformational changes [8, 9]. The poor sensitivity of mid-IR spectroscopy however can be a limiting factor for its use to study a single biolayer. Several approaches have been developed to overcome the limit of sensitivity, such as Infrared Reflection Absorption Spectroscopy (IRRAS) that is a well-established tool for measuring thin biolayers deposited on metal substrates, thanks to its high surface sensitivity [10, 11]. However, at grazing incident angle of IR radiation only the Transverse Magnetic (TM) modes of the Electric field (E) are sustained by a continuous metal surface due to the surface selection rule [12]. Therefore, only the protein dipole moments parallel to the surface normal can be excited, while information about the perpendicular ones is prevented. In order to monitor conformational changes and orientation of protein thin layers with both polarizations (TM and Transverse Electric (TE)), one has to resort to different strategies such as the use of Bloch Surface Waves [13] and/or of plasmonic nanoantennas. Notably, nanoantennas can be designed to excite plasmonic resonances with both TM- and TE-polarized light by changing the relative orientation of the nanoantennas with the E [14, 15].

Usually, in order to achieve a high sensitivity, nanoantennas are designed with high quality factors [16–19], leading to sharp resonances. Therefore, the overlap of the antenna modes with the resonant vibrational modes of

* Corresponding author: raffaella.polito@uniroma1.it

interest can only occur on a small frequency range and not in the entire "fingerprint region" (2–20 μm, 500–5000 cm^{-1}) that should instead be investigated, to monitor the complex functional mechanism of proteins. One possibility to overcome this obstacle is to design and perform subsequent experiments with several platforms of nanorods of different size with shortcomings in terms of both fabrication difficulties as well as sample and time consumption [20–23].

Here we propose a novel large-area platform for perspective polarization-resolved biosensor based on randomly sized self-organized gold nanorods deposited on nanopatterned glass templates and measured in reflection at grazing angles for the study of light-induced conformational changes of transmembrane proteins. We characterize the broad distribution of hotspots within a large sample area with IR nanospectroscopy and we perform a proof of principle experiment on Bacteriorhodopsin (BR) [24, 25]. With this easy-to-use platform, one can illuminate from the backside with visible radiation to induce the protein conformational change while monitoring the IR spectrum over the entire fingerprint region with high sensitivity, in principle down to the single biolayer.

In particular, we show that with our nanorod platform we find two distinct difference absorption spectra for incoming TM- or TE-polarized light, enabling polarization-resolved IRRAS spectroscopy over a broadband frequency range on biomolecules at variance with the current approaches in literature.

2 Results and discussion

2.1 Morphological and far-field optical characterization of nanorod array platforms

Based on a previously developed design for surface enhanced spectroscopies [26–28], we designed and produced a plasmonic platform for Surface-Enhanced Infrared Absorption Spectroscopy (SEIRA) consisting of anisotropic arrays of randomly sized gold nanorods deposited on rippled glass templates [29–31] by glancing angle thermal deposition at 70°. Figures 1a and 1c present a visible image of the sample that is homogeneous over large area (cm^2 scale), and the sketch of its ripple cross section. Morphological characterization of these self-organized arrays was performed by means of Scanning Electron Microscopy (SEM, Fig. 1b) and Atomic Force Microscopy (AFM, Fig. 1d), confirming the anisotropic ordering of the arrays along the axis defined as x, and the random distribution of the nanorods length between hundreds of nanometres and 3–4 μm. The profile analysis of the AFM topography images shows a Root Mean Square (RMS) roughness of 24 nm and a pattern periodicity (lateral distance between two nanorods) of 174 nm.

The nanorod platform is designed to perform an IRRAS experiment while exciting the sample deposited on it from the backside with visible light. We have thus characterized the transmission of the platform in far-field in both the visible (VIS) and IR regions (see Fig. 1e for a sketch of the optical setup) of the spectra. The data in Figures 1f and 1g show transmittance values above 0.8 when E is polarized perpendicular to the long nanorod axis. Transmittance settles to values above 0.6 for the other polarization ensuring that unpolarized visible light will efficiently reach the protein monolayer also with backside illumination since we expect to have a random orientation of the membrane patches within the sample. The mid-IR transmittance decrease to 0.30–0.60 between 3 and 5 μm (3300–2000 cm^{-1}) due to absorption in SiO_2. In more detail the drop at around 3300 cm^{-1} corresponds to the O-H stretching mode of silanol groups (Si-OH) of the soda lime substrate. The transmittance vanishes for wavelengths greater than 5 μm as the substrate is completely opaque and it can be characterized only in reflectance mode.

2.2 Far-field polarization dependent IRRAS spectra

We have studied the polarization response of our nanorod platform down to the mid-IR range by means of IRRAS spectroscopy (see sketched in Fig. 2a). There are four possible configurations in which one can impinge with linearly polarized radiation on our sample, depicted in Figure 2c, two with TM (green and orange curves) and two with TE (blue and pink curves) polarization.

For each polarization, the data are collected rotating the sample by 90° in order to have: (1) TE polarization and E oriented parallel (TE-Long axis, blue curve) or perpendicular (TE-Short axis, pink curve) to main axis of the nanorods; (2) TM polarization and E whose in-plane component is oriented parallel (TM-Long axis, orange curve) or perpendicular (TM-Short axis, green curve) to the main axis of nanorods. Figure 2b reports a representative SEM image of the nanorod platform with the direction of E vector drawn when it is perpendicular or parallel to the main axis of nanorods for both TE and TM polarization, in the latter case considering the in-plane component of the E only.

In all curves the transverse (TO) and longitudinal optical (LO) phonons of SiO_2 are visible between 1000 and 1200 cm^{-1}. One might notice that LO phonons are not visible in normal incidence IR spectra for the transverse nature of electromagnetic waves, but become visible for grazing angle incidence [32]. For spectra taken with TM polarization we mostly see the phonons of the SiO_2 substrate, and no difference is found when rotating the samples, *i.e.*, by having the in-plane component of the E parallel or perpendicular to the nanorods. We ascribe this to the high incidence angle of 80° that leads to a very small in-plane component of the E impinging.

With TE polarization not only we find an overall higher reflectance but one can notice a strong modification of the phonon visibility on the relative direction of the E and the long axis of the nanorods: indeed, when the incident E is parallel to the main axis of nanorods, a reduction of the visibility of the LO phonon mode of SiO_2 is found and we interpret this as an indirect proof that a plasmonic resonance is sustained by our nanorods.

2.3 Near-field optical characterization of nanorod array platform

Since the main application, that can be foreseen for this kind of plasmonic devices, is to use them for enhanced

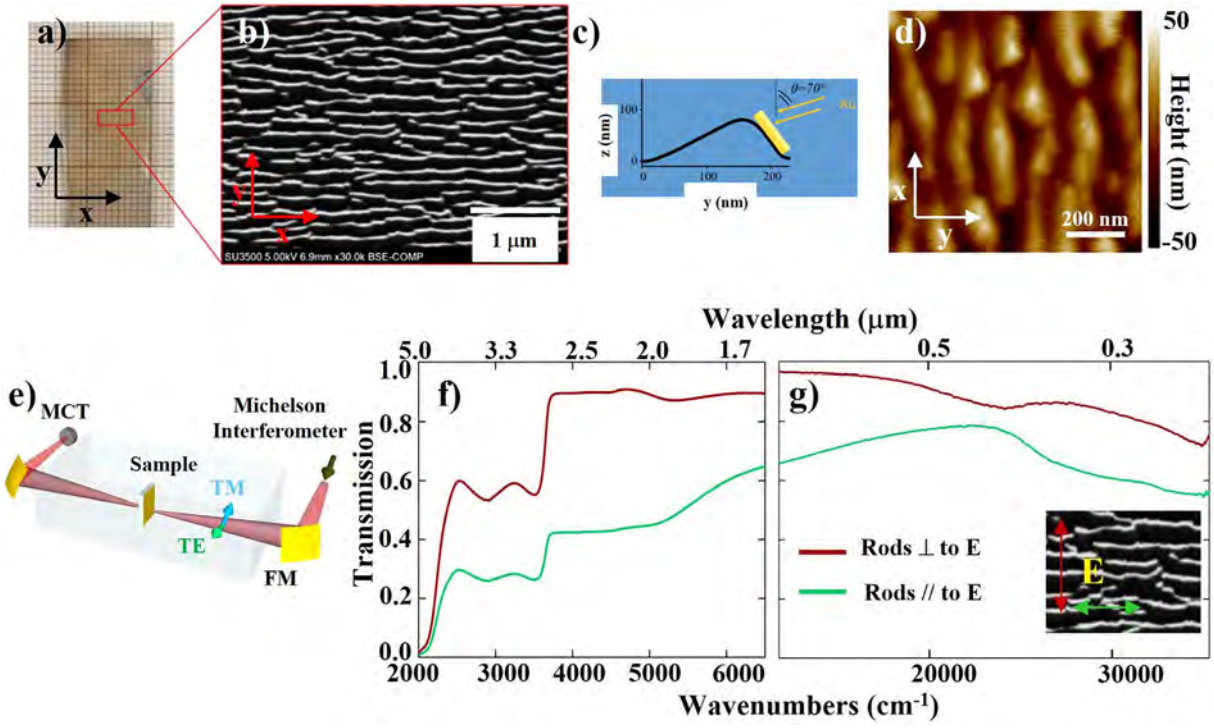

Fig. 1. (a) Visible image of the large-area nanorod platform showing the partial transparency of the sample. The sample is placed on a sheet of graph paper in order to highlight the spatial dimensions. (b) Representative SEM image. (c) Sketch of the ripple cross section for the nanorod platform. (d) AFM topography image of the nanorod platform. Note the disordered, although strongly anisotropic, arrangement of the gold nanorod array. (e) Sketch of the optical setup used to perform IR spectroscopy in transmission mode: the incoming IR radiation is focused by a parabolic mirror (FM) onto the sample. The radiation is linearly polarized by a wire-grid polarizer (the directions of E vector for both TE- and TM-polarized light are indicated by arrows in Figure). After the interaction with the sample, the IR radiation is focused onto an HgCdTe (MCT) photovoltaic detector. (f, g) Dichroic transmittance in the IR (f) and VIS (g) range for the two possible polarizations, *i.e.*, with E parallel or perpendicular to the main axis of nanorods.

spectroscopy, we performed near-field optical imaging to characterize the distribution of the hotspots and their dependence on the polarization of the impinging E. Therefore, we relied on photo-thermal induced resonance IR nanospectroscopy also called AFM-IR (see sketched in Fig. 3a) [33]. The IR intensity is acquired by monitoring the wavelength-dependent sample thermal expansion induced by the absorption of a mid-IR laser through the readout of the cantilever oscillation amplitude of an AFM. The AFM-IR signal can be modelled as:

$$\text{Photoexpansion signal}\,(x, y, \lambda) \propto \alpha(x, y, \lambda) \times V_{\text{exc}} \times I_{\text{laser}}$$

where $\alpha(x, y, \lambda)$ is the sample absorption coefficient, V_{exc} is the sample volume probed by IR radiation, I_{laser} is the IR radiation intensity [34, 35]. We have acquired the AFM-IR spectra of the nanorod platform with TE- and TM-polarized light impinging with an angle of 70° with respect to the sample surface normal. Figure 3b top, reports the AFM-IR spectra acquired positioning the AFM tip on top of a nanorod with TE polarization for both experimental configurations: when the main axis of nanorods is parallel to E (blue curve, TE-Long axis) and perpendicular to E (pink curve, TE-Short axis). The latter curve (TE-Short axis) shows two bands at 1080 and 1250 cm^{-1} related to the TO and LO phonons excitation. The blue curve (TE-Long axis) shows a suppression of the LO modes similarly to what seen in far-field because of the screening of free carriers excited along the rods. Figure 3b bottom, reports the AFM-IR spectra acquired with TM polarization when the main axis of nanorods is parallel to E (orange curve, TM-Long axis) and perpendicular to E (green curve, TM-Short axis). Also for TM polarization, the AFM-IR absorption spectra display the two bands at 1080 and 1200 cm^{-1} related to the TO and LO phonons excitation of SiO_2, mirroring the far-field IRRAS reflectance spectra (Fig. 2c).

AFM height maps and IR maps for TM and TE polarizations of a representative sample area of 3 × 3 μm^2 are reported in Figures 3c and 3d and Figures 3e and 3f, respectively. The IR maps are acquired by scanning the AFM tip on the sample area at fixed wavelength λ = 6.2 µm (1600 cm^{-1}). Figures 3g and 3h report the infusion maps of AFM height maps and IR maps for both polarizations in which the purple regions are the locations with higher IR absorption. For getting precise correlated maps, the drift is taken into consideration. We can notice that depending on the local configuration of the nanorods we get in the same sample region hotspots in slightly different regions, showing however that high IR intensity can be found in several spots, allowing us to average in a far-field sensing experiment over several of them, for both TE- and

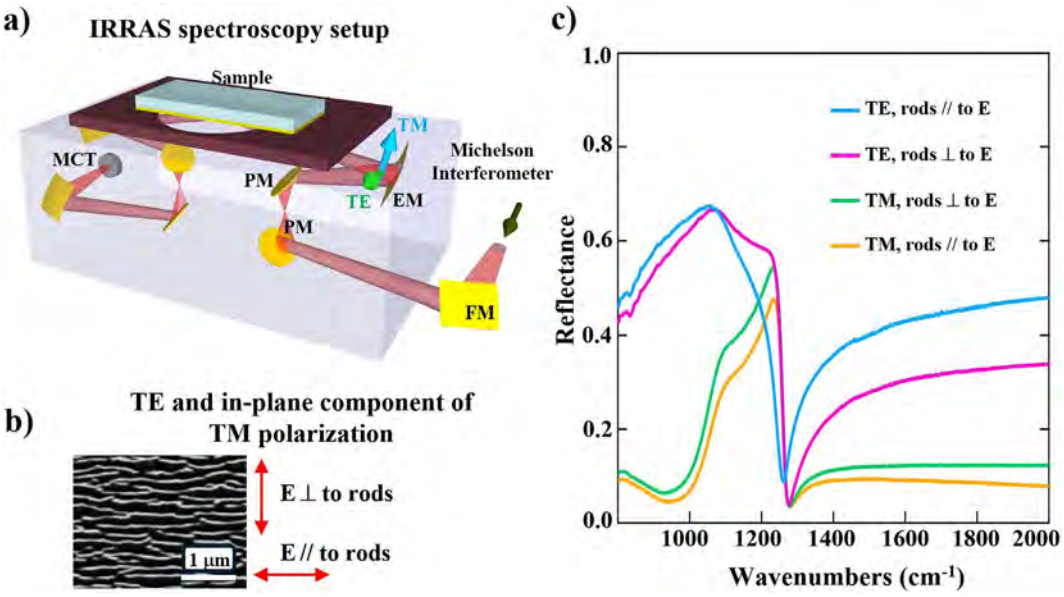

Fig. 2. (a) Sketch of the optical setup used to perform IRRAS spectroscopy: the incoming IR radiation, reflected by a parabolic mirror (FM) and two plane mirrors (PM), is focused by an elliptic mirror (EM) on the nanorod platform positioned in the upper part of the sample compartment. The radiation impinges with a grazing angle of 80° and it is linearly polarized by a wire-grid polarizer (the directions of E vector for both TE- and TM-polarized light are indicated by arrows in Figure). The outgoing IR radiation is focused finally onto an MCT photovoltaic detector through a specular mirror system. (b) Representative SEM image of the nanorod platform with the direction of E vector drawn when it is perpendicular or parallel to the main axis of nanorods, depending on the relative in-plane orientation of our sample and the E polarization. (c) IRRAS reflectance spectra of our sample when the main axis of nanorods is parallel to E using TE- (blue curve) and TM-polarized light (orange curve) and when the main axis of nanorods is perpendicular to E (pink curve and green curve for TE- and TM-polarized light, respectively).

TM-polarized light. Figure A1 in Appendix reports infusion maps acquired at other fixed wavelength with both polarizations and both relative orientations of E and the main axis of the nanorods.

2.4 Application to bacteriorhodopsin thin biolayers: SEIRA spectroscopy

To verify that our nanorod platform is suitable for SEIRA spectroscopy to detect very thin biolayers, we drop cast a suspension of cell membranes containing the light-sensitive transmembrane protein Bacteriorhodopsin (BR). The thickness of BR film is on average less than a hundred of nanometers and it is measured by AFM analysis. We acquired IRRAS reflectance spectra of BR film with both polarizations and in the two possible relative orientation between the main axis of nanorods and the direction of E, *i.e.*, parallel, or perpendicular (Fig. 4a). All IRRAS reflectance spectra are normalized for the IRRAS spectra acquired on the bare nanorod platform without BR proteins on top ($R_{\mathrm{IRRAS}} = I_{\mathrm{BR}}/I_{\mathrm{sub.bare}}$ with I_{BR} and $I_{\mathrm{sub.bare}}$ the spectrum of nanorods with and without BR on top, respectively) as reported by Greenler [36]. In case of a thin biolayer cast on a continuous metal surface, according to IRRAS spectroscopy theory, no reflection band related to protein should be visible in case of TE polarization. We find instead that our TE spectra (blue and pink curves in Fig. 4a) show the amide bands of proteins, the amide I band around 1660 cm^{-1} related to the C=O stretching mode and the amide II band around 1540 cm^{-1} due to the N-H bending mode of the peptide bonds [8]. When there is a plasmonic resonance excitation (TE-Long-axis, blue curve) the amide bands are less pronounced, while for TE-Short axis (pink curve) the features are stronger. We expect the nanorods to produce intense hotspots at their end for TE-Long axis. For TE-Short axis we can instead expect a smaller in-plane contribution of the E, but given their broad length distribution, an in-plane component of the field can be present, and since the volumes probed between parallel nanorods are several orders of magnitude larger than the small in-gap volume (see Figs. 3c and 3d), the overall signal IR signal averaged over a large area can be stronger.

We can suggest that given the morphological complexity of our nanorod platform and a non-negligible phase shift in the E close to the nanorod surface there will be a non-zero in-plane E intensity for TE polarization, for E parallel to both short axis and long axis.

For TM polarization (orange and green curves in Fig. 4a) we find that the most prominent feature is the amide I band, as expected since the C=O bond of the BR protein is aligned perpendicularly to the substrate/nanorod surface, while the amide II (the N-H bending mode is inversely aligned parallel to the substrate/nanorod surface) shows up as a weak dip in the reflectance spectra. This originates from two different factors: a thickness of about 100 nm on the biolayer film (only on a single protein monolayer the amide II band would become negligible) and a contribution of the nanorods that provide weak in-plane E [37, 38].

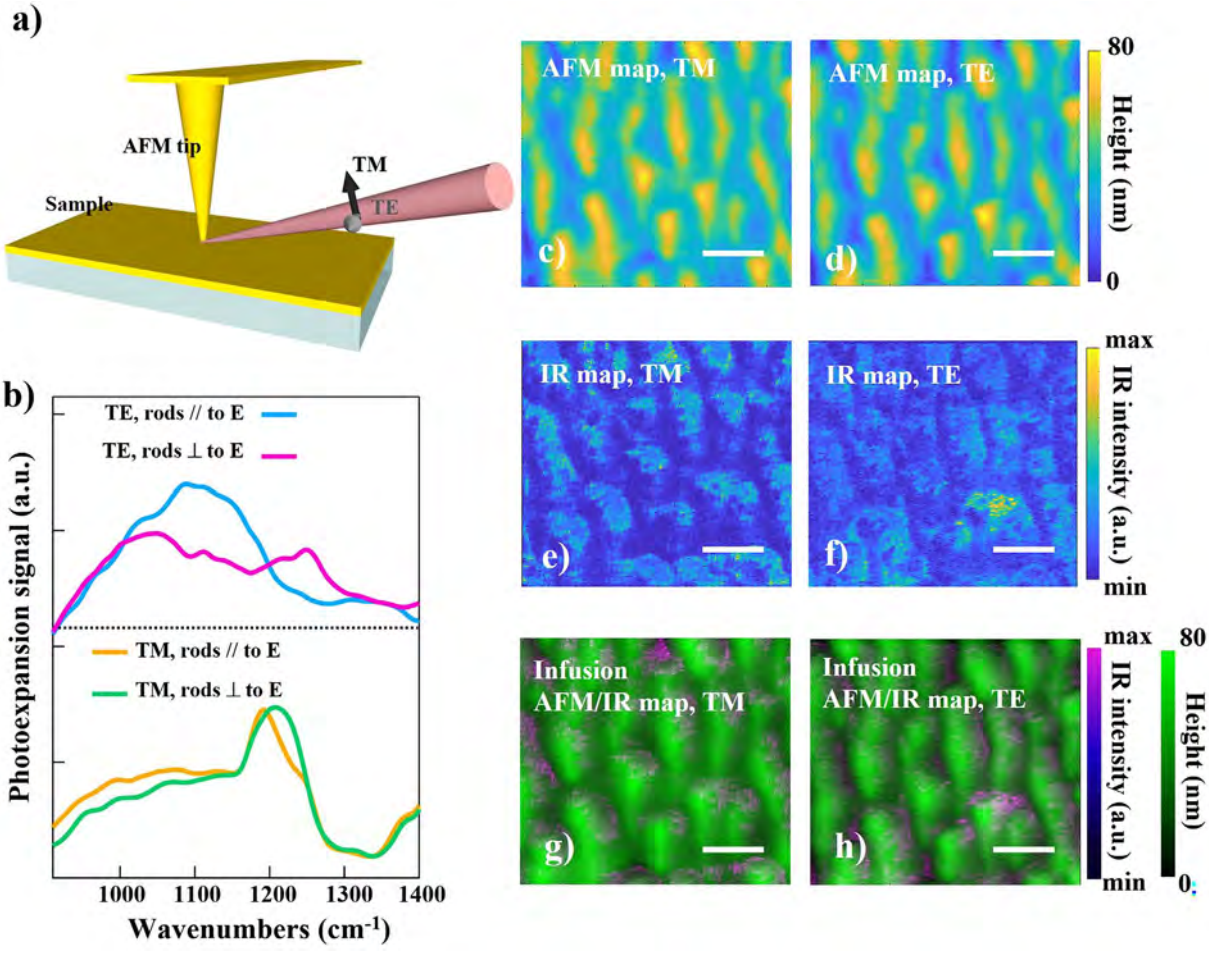

Fig. 3. (a) Sketch of AFM-IR setup with an oblique incidence of IR radiation of 70° with respect to the sample surface normal. (b) Top, AFM-IR absorption spectra in TE polarization with E parallel (blue curve, TE-Long axis) and perpendicular (pink curve, TE-Short axis) to the main axis of the nanorods. Bottom, same of top for TM polarization: orange curve and green curve for TM-Long axis and TM-Short axis, respectively. (c, d) AFM height maps for TM (c) and TE (d) polarizations and (e, f) IR maps at 1600 cm^{-1} ($\lambda = 6.2$ μm) for TM (short-axis) (e) and TE (long-axis) (f) polarizations. In order to acquire these maps, we have covered the nanorods with a thin polymer layer. (g, h) Infusion maps of AFM height maps and IR maps for TM (g) and TE (h) polarizations. It is possible to identify regions with higher IR intensity for both polarizations of the impinging radiation. For all maps the scale bar is 200 nm.

2.5 Application to bacteriorhodopsin thin biolayers: difference IRRAS spectroscopy

BR is a transmembrane protein sensitive to green visible light. Following light absorption, BR can move protons across the cell membrane thanks to a very fast retinal photo-isomerization and to a slower cyclic sequence of conformational changes of the protein backbone (also referred to as a "photocycle") [24, 25]. To isolate the extremely small ($\leq 10^{-3}$) light-induced changes in IR absorption, difference spectroscopy schemes (visible light ON minus visible light OFF) are employed typically on re-hydrated thick films or on liquid suspensions containing large numbers of proteins due to the poor sensitivity of IR spectroscopy [9, 39]. Here we were able to monitor the polarization-resolved light-induced conformational changes of a reduced number of BR proteins forming a film of thickness of less than a hundred of nanometers, by using the combination of our plasmonic platform with the difference IRRAS spectroscopy. To start the BR photocycle, the sample is illuminated with a LED emitting at 565 nm from the backside of the platform exploiting its transparency. In Figure 4c, the IRRAS difference spectra are reported, the blue curve in TE polarization and the orange curve in TM polarization with the E component parallel to the main axis of nanorods, *i.e.*, the two configurations in which a plasmonic behavior of our platform is expected. The grey curve in Figure 4c is the difference spectrum acquired on a 2-μm thick film of BR proteins deposited on a CaF_2 window in transmission mode used as a benchmark. In this case we expect to have a more or less isotropic orientation of the BR helices. In the IRRAS difference spectra, positive and negative peaks related to light-induced conformational changes of BR proteins are clearly identified. If comparing the difference spectra collected in TE and TM polarizations one can note several differences. In the spectral region of the amide I

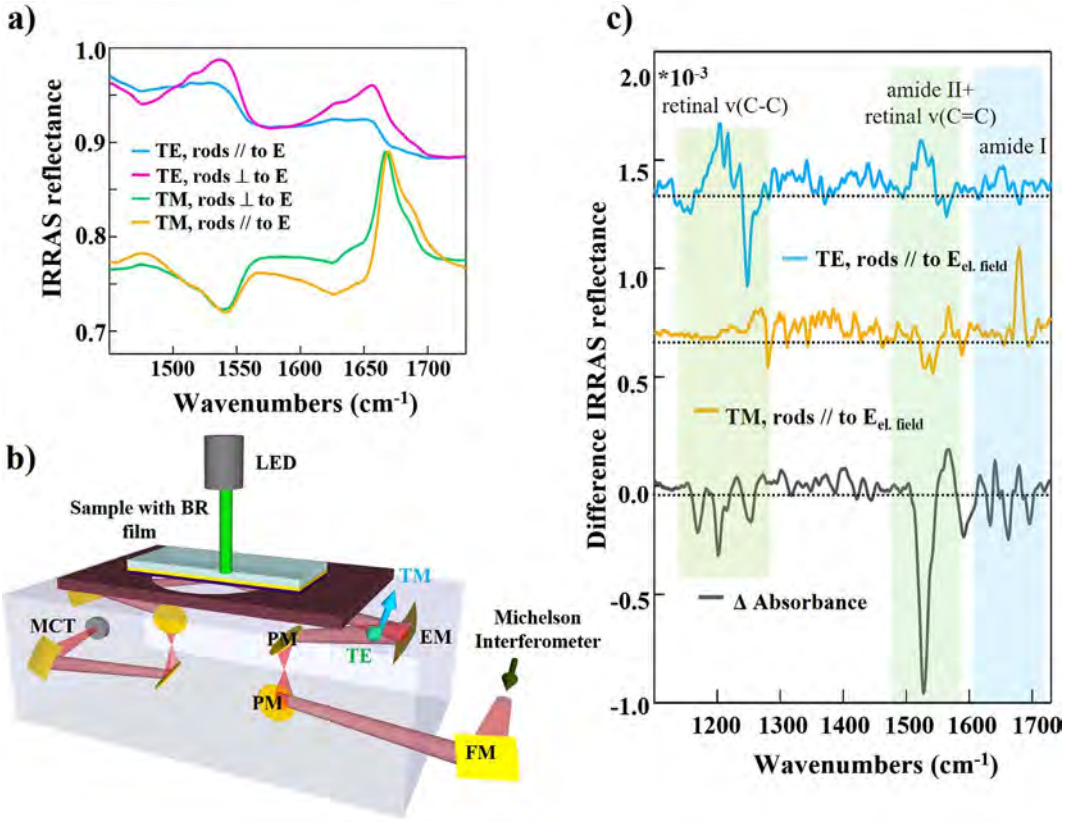

Fig. 4. (a) IRRAS reflectance spectra in the amide bands region of the nanorod platform with BR film deposited on top for all four possible configurations of nanorod orientation and light polarization. (b) Sketch of the experimental IRRAS setup to perform difference IRRAS spectroscopy of BR proteins. The green light emitted by a LED at 565 nm is sent to the backside of the platform exploiting its semi-transparency and it is used to start the BR photocyle. (c) IRRAS difference spectra of the nanorod platform with BR film using TE- (blue curve) and TM-polarized light (orange curve). For both curves the main axis of nanorods is parallel to E. The FTIR difference spectrum acquired on a 2-μm thick film of BR proteins deposited on a CaF_2 window in transmission mode is reported as grey curve.

band (1620–1680 cm^{-1}, blue region in Fig. 4c) it is clearly visible one intense feature for TM polarization that we explain due to the co-alignment of the C=O bonds of the protein backbone and the component of the E orthogonal to the substrate/nanorod surface that we expect to be strongest in this configuration. On the other hand, for TE polarization the peaks are really weak, as one can expect. One can note that instead in the spectral region that highlights modifications of the retinal (green regions in Fig. 4c) some peaks are completely different, and that some others are instead have opposing sign for the two polarizations, suggesting that in this case we can monitoring an overall rotation of the associated dipole moments.

3 Conclusion

We discuss the possibility to study polarization-resolved light-induced conformational changes of BR proteins drop cast on gold nanorods deposited on SiO_2. We exploit the transparency of the nanorod platform to perform difference IRRAS spectroscopy (visible light ON minus visible light OFF) with simultaneous visible light illumination from the backside of the platform. In our experiment we combine IRRAS with self-organized plasmonic nanorods in order to be able to probe with high sensitivity the modifications of the vibrational peaks over the entire fingerprint region. We show that it is possible to identify differences in the IRRAS difference spectra that imply we are monitoring over a broadband frequency range not only the chemical bonds with the dipole moment aligned orthogonally to our substrate/nanorod surface. This work is a first step into the polarization-resolved broadband sensing and conformational study of transmembrane proteins.

4 Materials and methods

4.1 Sample fabrication and morphology

Large area self-organized nanopatterns are obtained over large-area (cm^2) by defocused ion beam sputtering of low-cost glass substrates (soda-lime). Glass substrates are irradiated by means of a *Tectra GmhB* ion gun operating in Ar atmosphere at the pressure of 4.0×10^{-4} mbar and generating an ion beam of 800 eV energy. The substrate

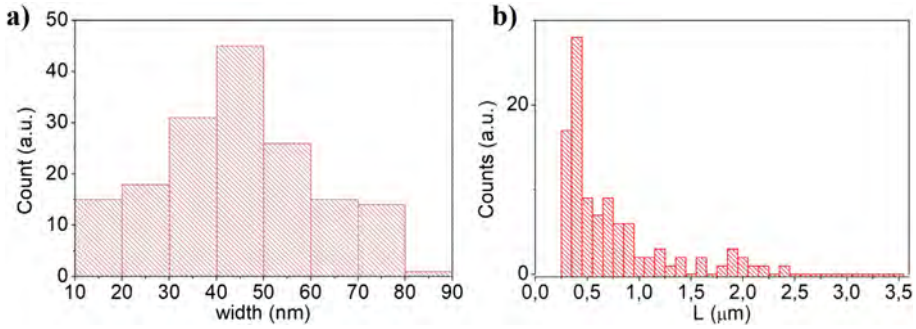

Fig. 5. Histograms of nanorods width (a) and length (b) measured by the statistical analysis of SEM images of the sample.

is irradiated at 30° incidence angle with respect to the glass surface normal, as described in detail in reference [29] with an ion fluence of 1.4×10^{19} ions/cm^2. To promote pattern formation under an ion induced wrinkling instability the sample is heated up to about 680 K temperature during the sputtering process.

This nanopatterned templates effectively promote confinement of anisotropic arrays of gold nanorods by glancing angle thermal evaporation perpendicular to the faceted glass nanoridges. Gold nanorods are confined on the short ripples facets (tilted at $\theta_{\text{facets}} = 50°$) by evaporation at θ_{Au} beam $= 70°$ with respect to the mean plane normal direction.

The local thickness of the gold stripes h is controlled by means of a calibrated quartz microbalance measuring the gold thickness deposited on a flat substrate (h_0). By basic trigonometric arguments the local thickness on the facets can be calculated $h = h_0 \times \cos(|\theta_{\text{Au beam}} - \theta_{\text{facet}}|)$. The distribution of the nanorods width, w, and length, L, is measured by the statistical analysis of SEM images of the sample. In Figure 5, the histograms of nanorods width (Fig. 5a) and length (Fig. 5b) are shown. The mean width reads about 45 nm with a relatively narrow distribution of size from 10 nm up to 70 nm, imposed by the template nanopattern. Conversely the nanorods length distribution is broad, extending from 250 nm up to 2 μm, with few counts up to 3.5 μm.

4.2 Cell membrane sample preparation

Patches of cell membranes containing BR were isolated as reported in reference [40] and stored in buffer solution (20 mM Bis-Tris propane, 100 mM NaCl, 1 mM MgCl2) at −80 °C. The thickness of an individual patch of cell membrane is 5 nm and the protein:lipid ratio is 75:25. For the IRRAS characterization, 6 μL of the suspension containing cell membranes were drop cast onto the nanorod platform for 3 min, then rinsed with 50 μL Milli-Q water and let dry in air.

4.3 IR spectroscopy

IR measurements in Figure 1f were performed in transmission mode with a Bruker VERTEX 80v spectrometer (*Bruker Optic GmbH*, Ettlingen, Germany) using an internal IR source and a MCT detector in vacuum condition. Spectra were recorded with a spectral resolution of 2 cm^{-1} and 512 interferometer scans using either perpendicular or parallel polarized light.

4.4 VIS spectroscopy

Normal incidence extinction spectra were acquired in the 300–1100 nm spectral range by coupling a compensated halogen-deuterium lamp (DH-2000-BAL, *Mikropak*) to a Vis-NIR spectrometer (HR4000, *Oceans Optics*) via fiber optics. The spot size is macroscopic with a diameter of about 2 mm. For linearly polarized measurements, a *Thorlabs Glen-Thompson* Polarizer was used, with a flat, bare glass serving as the reference. Normal incidence extinction spectra were also acquired in the Near Infrared (1000–2000 nm wavelength) by fiber coupling the same optical setup to a solid state Infrared spectrometer (*Arcoptix*).

4.5 IRRAS spectroscopy

IRRAS spectroscopy spectra were recorded with a Bruker VERTEX 80v spectrometer (*Bruker Optic GmbH*, Ettlingen, Germany) using a mirror system sketched in Figure 2a to focus polarized IR light onto the sample at a grazing angle of 80°. For the nanorod platform characterization (Fig. 2c), spectra were recorded with a spectral resolution of 2 cm^{-1} and 512 interferometer scans, using an aperture with a diameter of 1.5 mm. The measurements of the nanorod platform were referenced to the measurements of a reference gold substrate. For the nanorod platform with BR proteins on top characterization (Fig. 4a), spectra were recorded with a spectral resolution of 2 cm^{-1} and 1024 interferometer scans, using an aperture with a diameter of 1.5 mm. The measurements were referenced to the measurements of the nanorod platform without BR proteins on top.

4.6 IRRAS difference spectroscopy

IRRAS difference spectroscopy was performed by implementing a system of visible illumination to control BR photocycle. Visible light was provided by a LED (Thorlabs M565L3, center wavelength at 565 nm) and the power sent to the sample was around 10 mW/cm^2. The reflectance intensity was collected both in dark condition (R_{dark}) and under visible illumination (R_{green}) by averaging 256 interferometer scans at 2 cm^{-1} spectral resolution.

The difference IRRAS spectra in Figure 4c were calculated as: $-\log(R_{green}/R_{dark})$ by averaging over 100 illumination cycles.

4.7 AFM-IR imaging and nanospectroscopy

The AFM-IR imaging and nanospectroscopy were performed using a NanoIR2 system by Anasys Instrument relied on the photothermal expansion effect. The IR radiation impinges on the sample from the side at an angle of 70° and it is provided by an external-cavity broadly tunable quantum cascade laser (QCL) (MIRCATxB, by *Daylight Solutions*) with a spectral range 900–1800 cm^{-1}. The duration time of light pulses is 260 ns long and the laser repetition rate is chosen as to be in resonance with the second mechanical bending mode frequency of the cantilever (≈200 kHz). Commercial gold-coated AFM probes provided by Anasys/Bruker with free resonant frequency of 13 kHz and spring constant between 0.07 and 0.4 N/m were employed. The curvature radius of the probe tip apex is around 25 nm. AFM-IR spectra in Figure 3b were acquired with 4 cm^{-1} steps, with ≈0.3 s per step subdivided in tuning time and integration time. A smoothing spline algorithm has been applied to obtain the final AFM-IR spectra shown in Figure 3b. The AFM and AFM-IR images in Figures 3c and 3h were taken at 0.3 Hz with 100 × 100 points.

Funding

All the authors acknowledge support from the PRIN 2022 PNRR program, grant No. P2022JWKAC. M.C. Giordano acknowledges support from "Progetto Curiosity driven 2021" funded by *European Union – Next Generation EU.*

Conflicts of Interest

The authors declare no conflict of interest.

Data availability statement

Data will be made available from the corresponding author upon reasonable request.

Author contribution statement

FBM, MO, LB, and MCG: conceptualization, methodology, and design of the experiments; RP, SS, FS, GF, MET, VG, LB and MCG: investigation, RP, SS, FS, FB, MET, MO, and LB: analysis, and interpretation of the results; RP, FB, and LB: writing – original draft; all authors: writing – review and editing.

References

1 Baker M.J., Trevisan J., Bassan P., Bhargava R., Butler H.J., Dorling K.M., Fielden P.R., Fogarty S.W., Fullwood N.J., Heys K.A., Hughes C., Lasch P., Martin-Hirsch P.L., Obinaju B., Sockalingum G.D., Sulé-Suso J., Strong R.J., Walsh M.J., Wood B.R., Gardner P., Martin F.L. (2014) Using Fourier transform IR spectroscopy to analyze biological materials, *Nat. Protoc.* **9**, 1771–1791.

2 Brown L.V., Yang X., Zhao K., Zheng B.Y., Nordlander P., Halas N.J. (2015) Fan-shaped gold nanoantennas above reflective substrates for surface-enhanced infrared absorption (SEIRA), *Nano Lett.* **15**, 1272–1280.

3 Dong L., Yang X., Zhang C., Cerjan B., Zhou L., Tseng M.L., Zhang Y., Alabastri A., Nordlander P., Halas N.J. (2017) Nanogapped Au Antennas for ultrasensitive surface-enhanced infrared absorption spectroscopy, *Nano Lett.* **17**, 5768–5774.

4 Rodrigo D., Limaj O., Janner D., Etezadi D., De Abajo F.J.G., Pruneri V., Altug H. (2015) Mid-infrared plasmonic biosensing with graphene, *Science* **349**, 165–168.

5 Ataka K., Tilman K., Joachim Heberle H. (2010) Thinner, smaller, faster: IR techniques to probe the functionality of biological and biomimetic systems, *Angew. Chem. Int. Ed.* **49**, 32, 5416–5424.

6 López-Lorente Á.I., Mizaikoff B. (2016) Mid-infrared spectroscopy for protein analysis: potential and challenges, *Anal. Bioanal. Chem.* **408**, 2875–2889.

7 Ernst O.P., Lodowski D.T., Elstner M., Hegemann P., Brown L.S., Kandori H. (2014) Microbial and animal rhodopsins: structures, functions, and molecular mechanisms, *Chem. Rev.* **114**, 1, 126–163.

8 Barth A. (2007) Infrared spectroscopy of proteins, *Biochim. Biophys. Acta-Bioenergetics* **1767**, 9, 1073–1101.

9 Lorenz-Fonfria V.A. (2020) Infrared difference spectroscopy of proteins: from bands to bonds, *Chem. Rev.* **120**, 7, 3466–3576.

10 Blume A., Kerth A. (2013) Peptide and protein binding to lipid monolayers studied by FT-IRRA spectroscopy, *Biochim. Biophys. Acta-Biomembranes* **1828**, 10, 2294–305.

11 Enders D., Pucci A. (2006) Surface Enhanced Infrared Absorption of Octadecanethiol on Wet-Chemically prepared Au Nanoparticle Films, *Appl. Phys. Lett.* **88**, 184104.

12 Hoffmann F.M. (1983) Infrared reflection-absorption spectroscopy of adsorbed molecules, *Surf. Sci. Rep.* **3**, 2, 107–192.

13 Occhicone A., Pea M., Polito R., Giliberti V., Sinibaldi A., Mattioli F., Cibella S., Notargiacomo A., Nucara A., Biagioni P., Michelotti F., Ortolani M., Baldassarre L. (2020) Spectral Characterization of mid-infrared Bloch surface waves excited on a truncated 1D photonic crystal, *ACS Photonics* **8**, 1, 350–359.

14 Biagioni P., Huang J.S., Hecht B. (2012) Nanoantennas for visible and infrared radiation, *Rep. Prog. Phys.* **75**, 2, 024402.

15 Neubrech F., Huck C., Weber K., Pucci A., Giessen H. (2017) Surface-enhanced infrared spectroscopy using resonant nanoantennas, *Chem. Rev.* **117**, 7, 5110–5145.

16 Adato R., Altug H. (2013) In-situ ultra-sensitive infrared absorption spectroscopy of biomolecule interactions in real time with plasmonic nanoantennas, *Nat. Commun.* **4**, 1, 2154.

17 Adato R., Yanik A.A., Amsden J.J., Kaplan D.L., Omenetto F.G., Hong M.K., Erramilli S., Altug H. (2009) Ultra-sensitive vibrational spectroscopy of protein monnolayers with plasmonic nanoantenna arrays, *Proc. Natl. Acad. Sci.* **106**, 46, 19227–19232.

18 Temperini M.E., Di Giacinto F., Romanò S., Di Santo R., Augello A., Polito R., Baldassarre L., Giliberti V., Papi M., Basile U., Niccolini B., Krasnowska E.K., Serafno A., De Spirito M., Di Gaspare A., Ortolani M., Ciasca G. (2022) Antenna-enhanced mid-infrared detection of Extracellular Vesicles derived from human cancer cell cultures, *J. Nanobiotechnol.* **20**, 1, 530.

19 Neubrech F., Pucci A., Cornelius T.W., Karim S., García-Etxarri A., Aizpurua J. (2008) Resonant plasmonic and vibrational coupling in a tailored nanoantenna for infrared detection, *Phys. Rev. Lett.* **101**, 15, 157403.

20 Adato R., Serap A., Hatice A. (2015) Engineering mid-infrared nanoantennas for surface enhanced infrared absorption spectroscopy, *Mater. Today* **18**, 8, 436–446.

21 Rodrigo D., Tittl A., Ait-Bouziad N., John-Herpin A., Limaj O., Kelly C., Yoo D., Wittenberg N.J., Oh S.H., Lashuel H.A., Altug H. (2018) Resolving molecule-specific information in dynamic lipid membrane processes with multi-resonant infrared metasurfaces, *Nat. Commun.* **9**, 1, 2160.

22 Aouani H., Sipova H., Rahmani M., Navarro-Cia M., Hegnerova K., Homola J., Hong M., Maier S.A. (2013) Ultrasensitive broadband probing of molecular vibrational modes with multifrequency optical antennas, *ACS Nano* **7**, 1, 669–675.

23 D'Andrea C., Bochterle J., Toma A., Huck C., Neubrech F., Messina E., Fazio B., Marago O.M., Di Fabrizio E., Lamy de La Chapelle M., Gucciardi P.G., Pucci A. (2013) Optical Nanoantennas for Multiband Surface-Enhanced Infrared and Raman Spectroscopy, *ACS Nano* **7**, 4, 3522–3531.

24 Haupts U., Tittor J., Oesterhelt D. (1999) Closing in on bacteriorhodopsin: progress in understanding the molecule, *Annu. Rev. Biophys. Biomol. Struct.* **28**, 367–399.

25 Lanyi J.K. (2006) Proton transfers in the bacteriorhodopsin photocycle, *Biochim. Biophys. Acta-Bioenergetics* **1757**, 8, 1012–1018.

26 Giordano M.C., Longhi S., Barelli M., Mazzanti A., Buatier de Mongeot F., Della Valle G. (2018) Plasmon hybridization engineering in self-organized anisotropic metasurfaces, *Nano Research* **11**, 3943–3956.

27 Barelli M., Giordano M.C., Gucciardi P.G., Buatier de Mongeot F. (2020) Self-organized nanogratings for large-area surface plasmon polariton excitation and surface-enhanced Raman spectroscopy sensing, *ACS Appl. Nano Mater.* **3**, 9, 8784–8793.

28 Giordano M.C., Tzschoppe M., Barelli M., Vogt J., Huck C., Canepa F., Pucci A., Buatier de Mongeot F. (2020) Self-organized nanorod arrays for large-area surface-enhanced infrared absorption, *ACS Appl. Mater. Interfaces* **12**, 9, 11155–11162.

29 Giordano M.C., Buatier de Mongeot F. (2018) Anisotropic nanoscale wrinkling in solid-state substrates, *Adv. Mater.* **30**, 30, 1801840.

30 Giordano M.C., di Sacco F., Barelli M., Portale G., Buatier de Mongeot F. (2021) Self-organized tailoring of faceted glass nanowrinkles for organic nanoelectronics, *ACS Appl. Nano Mater.* **4**, 1940–1950.

31 Barelli M., Mazzanti A., Giordano M.C., Della Valle G., Buatier de Mongeot F. (2020) Color routing via cross-polarized detuned plasmonic nanoantennas in large-area metasurfaces, *Nano Lett.* **20**, 6, 4121–4128.

32 Almeida Rui M. (1992) Detection of LO modes in glass by infrared reflection spectroscopy at oblique incidence, *Phys. Rev. B* **45**, 1, 161–170.

33 Lu F., Jin M., Belkin M.A. (2014) Tip-enhanced infrared nanospectroscopy via molecular expansion force detection, *Nat. Photonics* **8**, 4, 307–312.

34 Lu F., Belkin M.A. (2011) Infrared absorption nano-spectroscopy using sample photoexpansion induced by tunable quantum cascade lasers, *Opt. Express* **19**, 21, 19942–19947.

35 Giliberti V., Polito R., Ritter E., Broser M., Hegemann P., Puskar L., Schade U., Zanetti-Polzi L., Daidone I., Corni S., Rusconi F., Biagioni P., Baldassarre L., Ortolani M. (2019) Tip-enhanced infrared difference-nanospectroscopy of the proton pump activity of bacteriorhodopsin in single purple membrane patches, *Nano Lett.* **19**, 5, 3104–3114.

36 Greenler R.G. (1966) Infrared study of adsorbed molecules on metal surfaces by reflection techniques, *J. Chem. Phys.* **44**, 1, 310–315.

37 Giliberti V., Badioli M., Nucara A., Calvani P., Ritter E., Puskar L., Aziz E.F., Hegemann P., Schade U., Ortolani M., Baldassarre L. (2017) Heterogeneity of the transmembrane protein conformation in purple membranes identified by infrared nanospectroscopy, *Small* **13**, 44, 1701181.

38 Polito R., Temperini M.E., Ritter E., Puskar L., Schade U., Broser M., Hegemann P., Baldassarre L., Ortolani M., Giliberti V. (2021) Conformational changes of a membrane protein determined by infrared difference spectroscopy beyond the diffraction limit, *Phys. Rev. Appl.* **16**, 014048.

39 Ritter E., Puskar L., Bartl F.J., Aziz E.F., Hegemann P., Schade U. (2015) Time-resolved infrared spectroscopic techniques as applied to channelrhodopsin, *Front. Mol. Biosci.* **2**, 38.

40 Oesterhelt D., Stoeckenius W. (1974) Isolation of the cell membrane of Halobacterium halobium and its fractionation into red and purple membrane, *Methods Enzymol* **31**, 667–678.

Appendix A

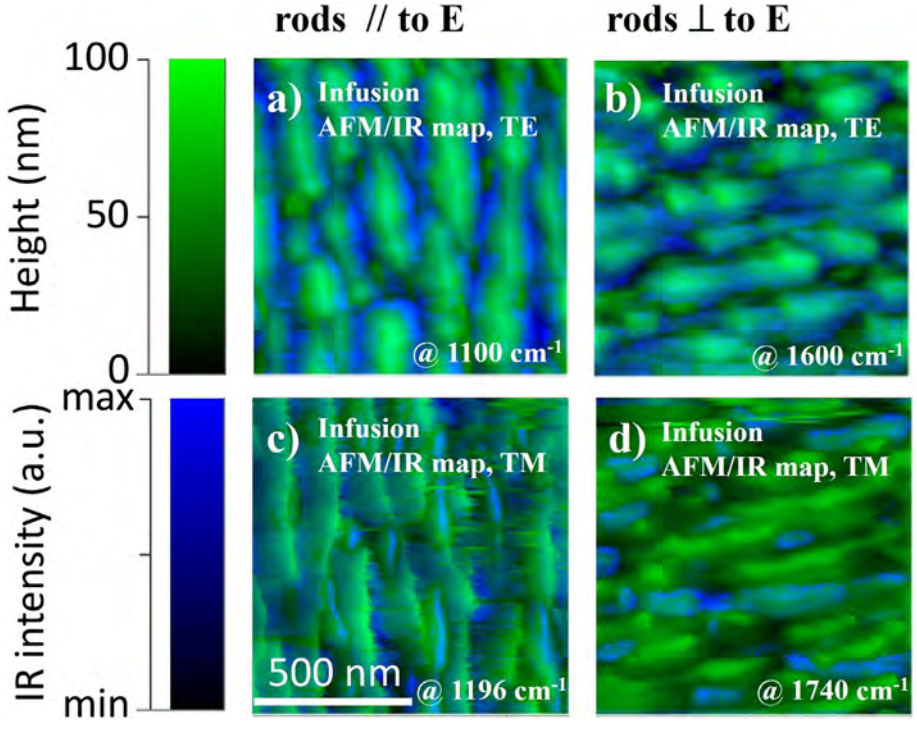

Fig. A1. (a, b) Infusion maps of AFM height maps (green scale bar) and IR maps (blue scale bar) for TE polarization with E parallel (a) and perpendicular (b) to the main axis of the nanorods. IR maps are acquired at 1100 cm^{-1} and 1600 cm^{-1} for (a) and (b), respectively. (c, d) Infusion maps of AFM height maps and IR maps for TM polarization with E parallel (c) and perpendicular (d) to the main axis of the nanorods. IR maps are acquired at 1196 cm^{-1} and 1740 cm^{-1} for (a) and (b), respectively. In all infusion maps, regardless of light polarization and relative orientations between E and the main axis of the nanorods, it is possible to identify an overall distribution of blue regions with higher IR intensity.

J. Eur. Opt. Society-Rapid Publ. 2024, **20**, 10

https://doi.org/10.1051/jeos/2024013
Available online at: https://jeos.edpsciences.org

Special Issue - Plasmonica 2023
Antonino Foti and Attilio Zilli (Guest editors)

Journal of the European Optical Society-Rapid Publications

RESEARCH ARTICLE

OPEN ACCESS

Development of a wearable surface enhanced Raman scattering sensor chip based on silver nanowires for rapid detection of urea, lactate and pH in sweat

Cristiano D'Andrea[1,*], Martina Banchelli[1], Chiara Amicucci[1], Panagis Polykretis[1], Filippo Micheletti[1], Marella de Angelis[1], Byungil Hwang[2,*], and Paolo Matteini[1,*]

[1] Institute of Applied Physics "Nello Carrara" (IFAC), Italian National Research Council (CNR), Via Madonna del Piano 10, Sesto Fiorentino (Florence) I-50019, Italy
[2] School of Integrative Engineering, Chung-Ang University, Seoul 06974, Republic of Korea

Received 9 January 2024 / Accepted 17 March 2024

Abstract. A wearable sweat sensor chip based on surface-enhanced Raman spectroscopy (SERS) is here presented. The plasmonic core of the chip, obtained by deposition of silver nanowires on a polytetrafluoroethylene (PTFE) porous membrane, permits the direct and label-free detection of urea and lactate at physiologic concentrations in combination with the pH measurement in the range between 5 and 9. Once integrated with commercial biocompatible and adhesive tape layers, the as produced SERS-active chip provides a low-cost, flexible and wearable sensing device for rapid and reliable human sweat analysis. The chip was finally tested on real sweat samples to estimate lactate and urea during medium-intense exertions.

Keywords: Wearable sensor, SERS, Sweat, Urea, Lactate, pH, Silver nanowires.

1 Introduction

In the last decades, wearable sensors have received much attention thanks to their ability to provide useful information about metabolism and health of individuals [1]. Wearable devices originally developed for tracking physical exercise activity (*i.e.*, heart rate, burned calories, steps count) or to monitor biomedical parameters (*i.e.*, glucose concentration in blood) have stimulated major technological efforts to turn them into advanced biosensing platforms (lab-on-chip) for continuous monitoring of multiple health parameters and real-time sensing of physiological information with a potentially large impact in our daily lives [1, 2]. Sweat contains a broad variety of non-invasively accessible biomarkers that can provide key information directly related to body health in a continuous and on-demand way. Typical sweat components are electrolytes (sodium, potassium), metabolites (lactate, glucose, urea, uric acid, creatinine), minerals (calcium, magnesium, iron, zinc), amino acids (tyrosine, tryptophan), hormones (cortisol, testosterone) and proteins (C-reactive protein), with concentrations that ranges from mM to tenths of nM. Moreover, compared with other biofluids like blood, interstitial fluid, tear, saliva, and urine, sweat probing can be easily achieved by placing a sensor patch on accessible locations of the skin [2].

Surface-enhanced Raman scattering (SERS) is a spectroscopic technique that permits the label-free detection and vibrational characterization of analytes at sub-micromolar concentrations thanks to the plasmonic amplification of the Raman optical signals generated in proximity of noble metal nanoparticles surface (hot spots) [3, 4]. The possibility to easily integrate SERS-active layers onto flexible substrates, coupled with the recent availability of low-cost, miniaturized, handheld commercial Raman spectrometers, have paved the way for the development of optical technological platforms for the non-invasive healthcare monitoring by sweat inspection.

Recently, silk fibroin protein films were used in combination with silver nanoparticles, as a biocompatible layer for detecting lactic acid or drugs directly on the skin [5, 6]. Nanostructured polymeric films or membranes were decorated with noble metals and exploited as substrates for detection of lactic acid, uric acid, ascorbic acid from trace amounts of sweat [7–10]. More complex superhydrophobic/superhydrophilic layers were also combined with SERS active nanoparticles for detection of narcotics or physiological biomarkers, such as dopamine, creatinine or cortisol, in real sweat samples. [11, 12]. Moreover, SERS-active layers were functionalized with pH sensitive molecules [13], or combined with microfluidic circuits developed

* Corresponding authors: c.dandrea@ifac.cnr.it; p.matteini@ifac.cnr.it.

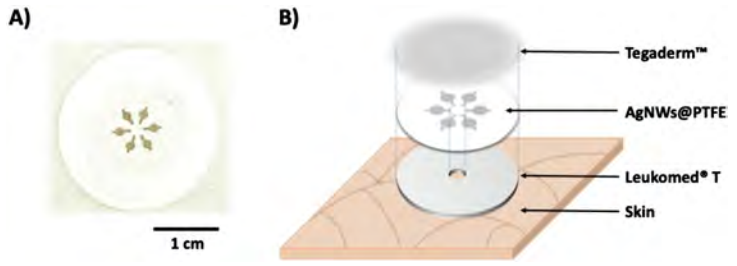

Figure 1. (A) Picture of a patterned AgNWs layer deposited on a hydrophobic PTFE filter membrane. Six 1.5 mm diameter circular spots are arranged with a radial bicycle spokes-like geometry. The AgNWs linear components have lengths of 2 mm and widths of 0.5 mm, respectively. (B) Schematic representation of a wearable SERS-active chip. The AgNWs@PTFE substrate is "sandwiched" between biocompatible and adhesive Tegaderm™ and Leukomed® T tapes. Both PTFE membrane and Leukomed® T tape are drilled in the centre in order to obtain an hole with a diameter of 2 mm that allows the direct flow of sweat from the skin to the hydrophilic AgNWs on top of PTFE. The Tegaderm™ tape instead acts as transparent and protective layer of the entire chip.

for collecting and guiding the sweat flow towards the sensor sensitive parts [14], in order to monitor the pH level of sweat or the content of its metabolites.

In this work we report the development of a SERS-active chip based on silver nanowires (AgNWs) deposited on a flexible polytetrafluoroethylene (PTFE) membrane. The SERS effect was successfully exploited for sensitive detection of urea and lactate from a model solution that mimics human sweat. By adding an additional functionalization step with a pH sensitive Raman probe, the AgNWs@PTFE substrate enabled the evaluation of sweat pH in the range of 5–9. Finally, the as-fabricated AgNWs@PTFE substrate was integrated with commercial, biocompatible and protective adhesive layers to obtain a fully flexible and wearable sensor chip for detection of analytes from sweat samples collected directly from the skin.

2 Materials and methods

AgNWs@PTFE chips were produced following the method recently reported by our group [4, 15]. In brief, 1 mL of commercial AgNWs dispersed in ethanol at concentration of 0.5 μg/μL (3D-nano Company, Poland), characterized by an average diameter of 100 nm and length ranging between 5 and 50 μm, were deposited by flow-through filtration (Amicon stirred cell 8003, Millipore) on a PTFE filter membrane (Sartorius, 25 mm diameter, 200 μm thick, pore size of 0.45 μm) with a final density of 0.1 $\mu g/mm^2$. The as-deposited AgNWs layer was patterned in 6 circular spots with 1.5 mm diameter and a radial geometry using a laser engraver (Neje, spatial resolution 0.45 mm, laser source tuned at 450 nm, max power 3W), in order to produce a hydrophilic and confined SERS-active region surrounded by a hydrophobic one (Fig. 1A). Laser pattern geometry includes the presence of an AgNWs rectangular channel radially arranged for each spot, with dimension of 2 mm in length and 0.5 mm in width, exploited for liquid flowing once the SERS chip is embedded with wearable tapes.

A human sweat model solution was prepared with the aim to test the SERS ability of the patterned AgNWs@PTFE membranes to detect urea and lactate at representative physiologic concentrations and to estimate the pH values. Simulated sweat (SS) was obtained by mixing (w/v) 0.1% urea, 0.1% lactate and 0.5% NaCl in ultrapure water (chemicals purchased by Merck), while the pH was fixed by using a phosphate buffer and tested by a bench pH-meter. The SERS activity of the substrate was studied varying the urea or lactate concentration from 0.01% (w/v) (1.67 mM) to 1.5% (250 mM), whereas the typical human physiologic values range between 5 and 200 mM. Each experiment was carried out by drop-casting 2 μL of analyte solution onto the AgNWs@PTFE spot, followed by waiting 1 min of incubation time and removal of the excess of liquid. All the experiments were conducted in triplicate and for three different pH values fixed at 4.8, 6.6 and 9.0. These values were selected to account for both the physiological mean pH value of sweat and any oscillations due to altered conditions.

A pH-sensitive probe molecule (4-mercaptobenzoic acid; 4-MBA) was employed to functionalize AgNWs and evaluate the pH level of sweat solutions [14]. Specifically, a spot of the as-fabricated AgNWs@PTFE was incubated for 12 h in a 4-MBA aqueous solution at 5×10^{-5} M concentration, washed and dried in air.

In parallel, identical SERS chips were integrated in a biocompatible tape sandwich including Tegaderm™ (3M™) and Leukomed® T (Leukoplast®) as protective/adhesive and spacer layers, respectively, as shown in Figure 1B. More in detail, both AgNWS@PTFE membrane and Leukomed® T tape were drilled in the center in order to produce a hole with diameter of 2 mm that allows the direct flow of sweat from the skin to the hydrophilic AgNWs on top of PTFE membrane. On the contrary, the Tegaderm™ tape act as transparent and protective layer on top of the chip.

Experiments on real sweat sample were performed directly sticking the biocompatible SERS chip on volunteer's arm and collecting the secretion during moderate to intense physical exercise.

SERS spectra were acquired using a micro-Raman spectrometer (LabRam HR800 Evolution, Horiba) equipped with an excitation laser tuned at 785 nm, focused through a 50× LWD objective (Olympus, NA 0.5), and using a laser power at sample and integration time fixed at 400 μW and 5 s, respectively. For each sample, 30 spectra were acquired

on different position of the SERS substrate. The acquired spectra were pre-processed and elaborated using Labspec 6.0 (Horiba) and OriginPro (Origin Lab) software. Specifically, the spectra were normalized with respect to the peak centred at 1765 cm^{-1} relative to the AgNWs@PTFE substrate, and the average spectrum was calculated and reported.

3 Results and discussion

The laser-patterned spot-deposition method recently described by our group [4, 15] guarantees a spatial control over the AgNWs area on PTFE, producing a confined SERS-active hydrophilic region surrounded by a hydrophobic one, as shown in Figure 1A. The immediate advantage is that few tens of μL of sweat secreted by the skin are enough to flow through the hole on the PTFE membrane and forced to be adsorbed on the AgNWs surface without the need of microfluidic channels.

Before the application of the wearable AgNWs@PTFE chip for sweat analysis, we firstly tested the ability of the patterned AgNWs layer on PTFE for the SERS detection of urea and lactate in simulated sweat (SS) at concentration values ranging between 0.01% and 1.5% (w/v) for three different pH values.

Figure 2 shows the SERS spectra of the SS for increasing concentration of urea, from 0.01% to 1.5% (w/v), and pH levels fixed at 4.8, 6.6 and 9.0. The spectra show a sharp dominant peak at 1002 cm^{-1} relative to the C–N symmetric stretching vibration of urea, which increases in intensity at higher concentrations. C–N vibrations are also responsible of the less intense peak centred at 1410 cm^{-1}, while the peaks at 934 cm^{-1}, 1048 cm^{-1}, 1426–1451 cm^{-1} are assigned to the CH_3 and CO modes of lactate [14, 16]. The area under the main vibrational peak of urea centred at 1002 cm^{-1}, in the spectral range from 950 to 1040 cm^{-1} was employed for the calibration curve reported in Figure 2B. For all three pH values, a sigmoidal behaviour can be observed. The data were further reported in log–log graph, showed in the inset of Figure 2B, and fitted by a linear function in the range from 16 to 250 mM.

SERS spectra of SS at increasing concentrations of lactate are reported in Figure 3A. The intense urea peak observed in Figure 2A is still visible but less dominant due to the urea concentration set at 0.1% (w/v), making the intensity of the lactate Raman modes more appreciable in the spectral region between 813–875 cm^{-1} and 1420–1450 cm^{-1} [14]. A slight fluctuation of urea peak is also observed despite its concentration being constant. We hypothesize mutual interference between lactate and urea that alters its SERS response with increasing lactate concentration. However, these fluctuations are negligible compared to the signal variations observed with varying urea concentrations (Fig. 2A). The area of the vibrational band related to the C–C aliphatic stretching peaked at 853 cm^{-1} was employed for calibration, as reported in Figure 3B. The data obtained exhibit a sigmoidal behaviour and when represented on a log–log scale as highlighted in the inset of Figure 3B, they adhere to a linear model in the range from 1.67 mM to 250 mM. These results confirm a concentration dependence of SERS response for these peaks, which is in accordance with the scientific literature [17–21].

As a proof of validation of the AgNWs@PTFE chip for detection and estimation of urea and lactate content in sweat, we also performed experiments using real sweat samples produced by a volunteer during physical exercise. Six different experiments were conducted and the SERS spectra are reported in Figure 4A. Specifically, these spectra were acquired under identical experimental conditions (laser wavelength, grating, detector) and normalized for laser power and integration time to ensure comparability with the spectra obtained from SS. The areas of the spectral regions assigned to lactate and urea vibrational bands, centred at 853 and 1002 cm^{-1}, respectively, were then calculated from the SERS spectra of real sweat and utilized for concentration estimation. Analysing the sweat from different rounds of physical activity, we detected lactate and urea concentrations ranging from 19 to 60 mM and from 50 to 80 mM, respectively, as shown in Figure 4B.

In order to improve the AgNWs@PTFE chip's sensing capabilities and expand its application to include sweat pH estimation, we functionalized the silver surface using a pH-sensitive molecule whose SERS spectral signature varies with pH. Some AgNWs spots on PTFE membrane were then incubated overnight in 4-MBA (see Materials and methods), allowing the formation of an effective pH-sensitive layer due to the formation of stable Ag–S bonds [14, 22]. We exploited the ability of 4-MBA to undergo a shift and an intensity variation of the Raman modes relative to the stretching of the carboxylate group (COOH) in the 1400–1425 cm^{-1} spectral region as consequence of the pH changes [23]. In particular, 2 μL of PBS solution with pH values ranging between 1.1 and 12.0 were drop-casted on the spots functionalized with 4-MBA and were incubated for 1 min followed by removal of excess liquid. The variation of the pH values from 1.1 to 12.0 induces a red-shift and an intensity increase of the peak centred at 1400 cm^{-1} (Fig. 5A). The changes become more evident at higher pH values, in which the carboxylate group vibration appears as a more intense and asymmetric band centred at 1425 cm^{-1}. On the contrary, pH variations do not affect the sharp peak assigned to the benzene ring breathing, centred at 1592 cm^{-1} [23]. The pH calibration curve can be then obtained normalizing the area of the bands in the 1400–1425 cm^{-1} interval to the area of the peak at 1592 cm^{-1}, as reported in Figure 5B. Such data, acquired in triplicate, can be described by a sigmoidal model function, with a linear trend in the pH interval between 5 and 9 and a correlation coefficient of 0.92. The AgNWs@PTFE functionalized with 4-MBA were moreover tested against three custom SS solutions at known pH values. The normalized areas of the 1400–1425 cm^{-1} band are reported in Figure 5B as geometrical symbols (red diamond, blue square and purple circle) for pH equal to 4.8, 6.6, 9.0, respectively, in any case falling within the 95% prediction interval.

When SERS chips and their application as innovative platform for fast monitoring of health status by sweat

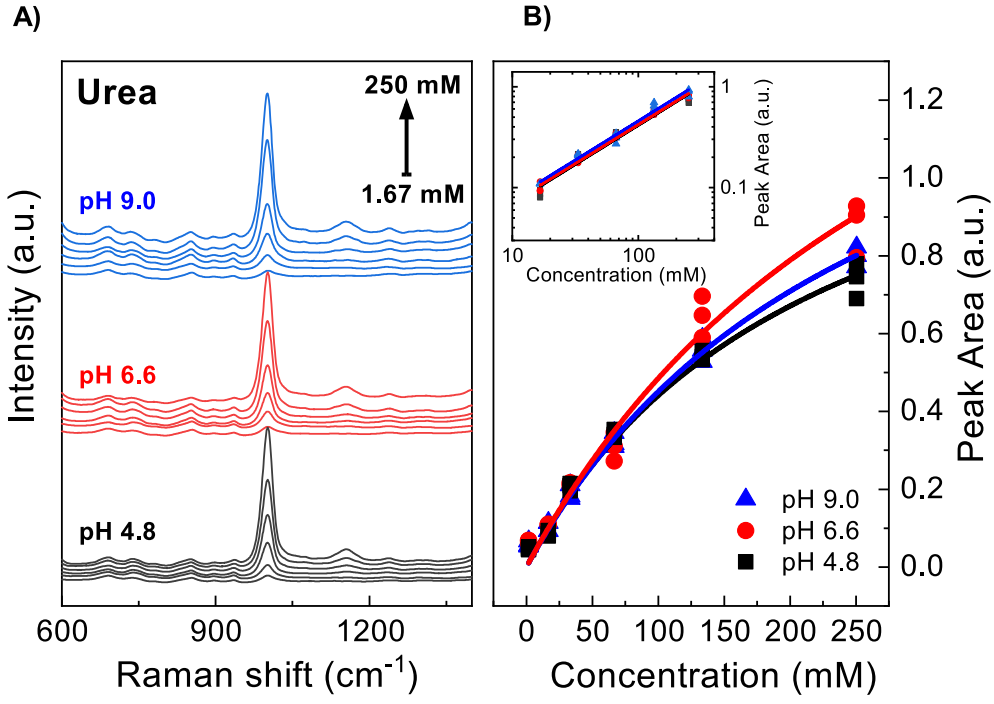

Figure 2. (A) SERS spectra of SS solutions at increasing concentrations of urea (0.01%, 0.1%, 0.2%, 0.4%, 0.8%, 1.5% (w/v)), acquired at three fixed pH values (black lines pH = 4.8, red lines pH = 6.6, blue lines pH = 9.0). The experiments were repeated three times on different AgNWs spots, the reported spectra represent the average of the three repetitions and were stacked for clarity. (B) Calibration curve obtained integrating the spectral raw data of the urea vibrational band comprised in the range 950–1040 cm^{-1} and peaked at 1002 cm^{-1} for each concentration value in three different experiments and for three pH values. Experimental data (scatter points) follow a sigmoidal model (coloured lines). The inset shows a log–log plot of the data, fitted by a linear function ($y = 4.10 + 0.77x$, $r^2 = 0.98$).

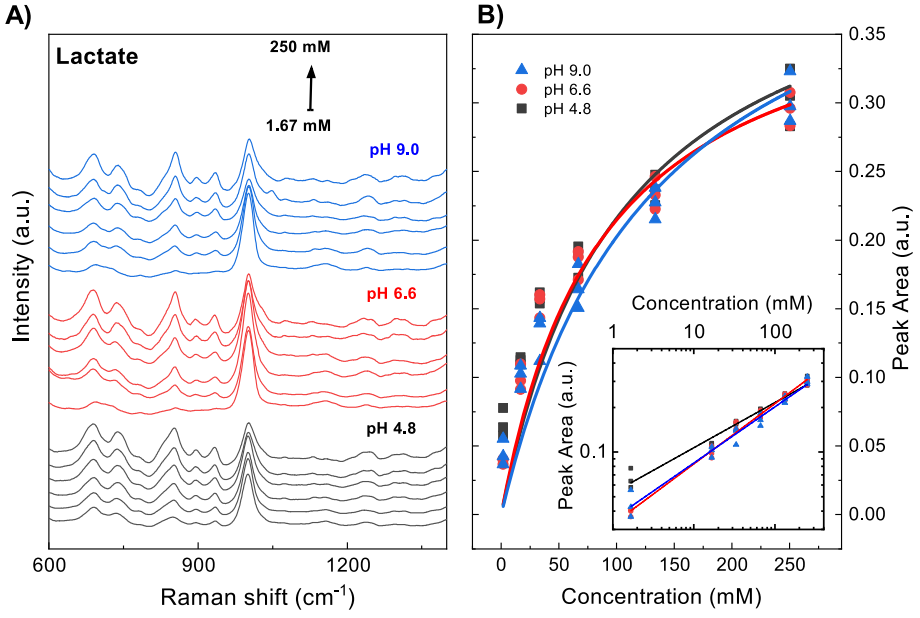

Figure 3. (A) SERS spectra of SS solution at increasing concentrations of lactate (0.01%, 0.1%, 0.2%, 0.4%, 0.8%, 1.5% (w/v)) acquired at three fixed pH values (black lines pH = 4.8, red lines pH = 6.6, blue lines pH = 9.0). The experiments were repeated three times on different AgNWs spots. The spectra reported represent the average of the three repetitions and were stacked for clarity. (B) Calibration curve obtained integrating the spectral raw data of the lactate vibrational band in the range 813–875 cm^{-1} for each concentration value in three different experiments and for three pH values. Experimental data (scatter points) exhibit a sigmoidal behaviour (coloured lines). When reported in a log–log plot (inset) the data follow a linear model ($y = 4.72 + 0.30x$, $r^2 = 0.98$ at pH 4.8; $y = 4.51 + 0.39x$, $r^2 = 0.99$ at pH 6.6 and 9.0).

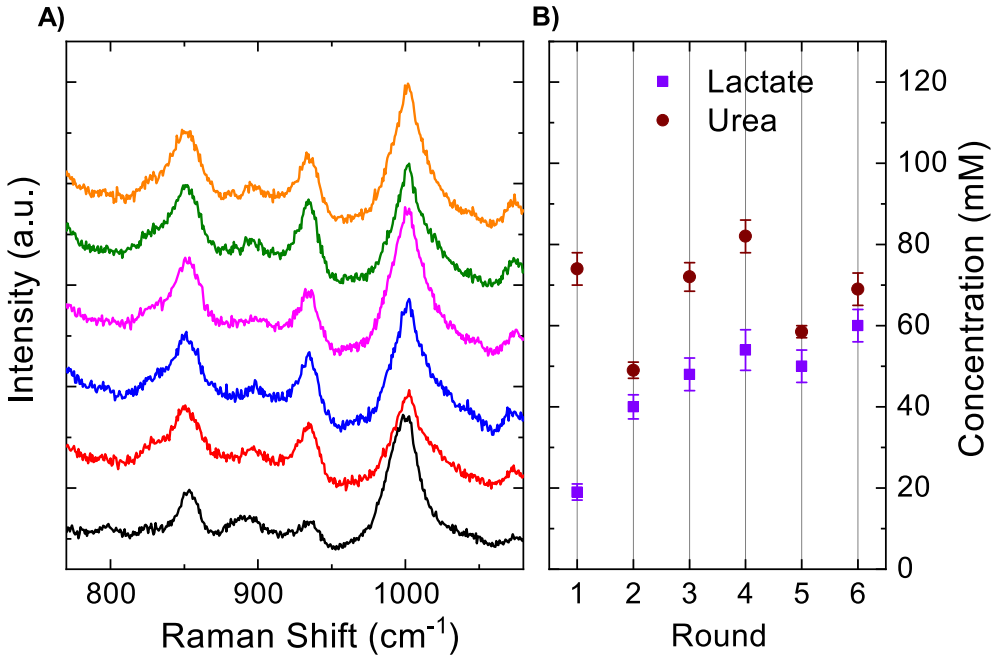

Figure 4. (A) SERS spectra of real sweat sample from a volunteer collected during six different rounds of physical exercise. Lactate and urea bands, centred at 853 and 1002 cm^{-1}, respectively, were used for estimating their concentration, as reported in panel (B) by using the calibration curves shown in Figures 2B and 3B.

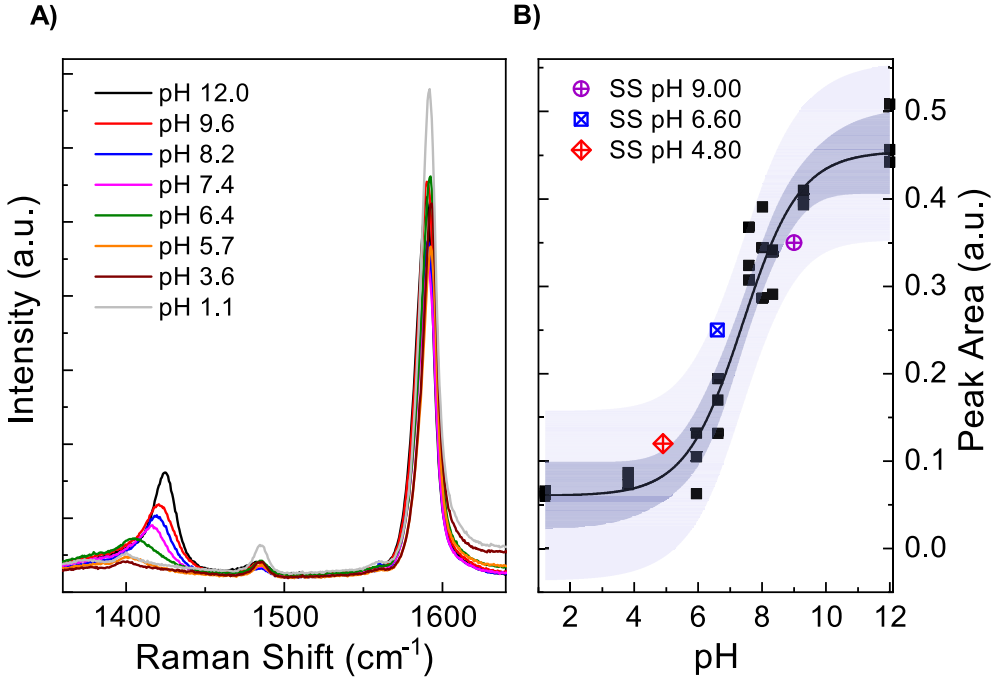

Figure 5. (A) SERS spectra of 4-MBA on AgNWs@PTFE after the incubation with 2 µL of PBS solution at different pH values. (B) Calibration curve obtained calculating the area under the bands in the 1400–1425 cm^{-1} interval relative to vibration of the carboxylate group, normalized for the area of the peak centred at 1592 cm^{-1} assigned to the benzene ring breathing mode. Calculated data (square symbols) are fitted with a sigmoidal function (black line) and the 95% confidence and prediction bands are reported in dark and light violet, respectively. Three SS solution with different pH values were used in order to test the chip and the obtained results are indicated with red, blue and purple geometrical symbols.

analysis are concerned, the manufacturing costs of the substrate must also be taken into account. At present, in our knowledge, there are no commercial SERS substrates on the market that meet the necessary flexibility and wearability requirements for such applications. Recent advancements in nanostructures production, affordability and signal reproducibility of substrates, led to a broader availability of commercial SERS platforms proposed by different companies [24–27]. These substrates are typically composed by a rigid glass support combined with a hydrophobic layer on which an area of few mm^2 is decorated with silver or gold nanostructures that act as sensitive region. Generally, the cost of these systems varies from 20 € to 80 € per substrate.

The wearable SERS chip here reported shows the advantage of being made up of only commercially available materials and do not require the application of technically complex and expensive fabrication procedures.

Moreover, both the instruments used for deposition by flow-through filtration (stirred cell) and laser patterning (laser engraver) of AgNWs require an initial total investment below 2 k€. We then tried to estimate the price of a wearable AgNWs@PTFE SERS chip calculated as the sum of the price of the AgNWs plus that of the PTFE filter membrane, of the chemicals needed for the deposition and of the biocompatible tapes used. In the calculation, we haven't considered labour cost, since it can be highly variable depending on the professional level of the operator and the country of production, nether we accounted for the cost of purchasing and managing the machinery. Considering an average cost of 30 €cents for the silver layer (1 mL of ten times diluted AgNWs solution), a unit prize of 3.75 € for each PTFE filter membrane and an average consumption of 2 mL of ethanol for dilution and preparation (ethanol 96%, price 51 €/L) a total cost of 4.15 € for each AgNWs@PTFE substrate can be estimated. Considering a 3 cm × 3 cm average area for both the Tegaderm™ (10 cm × 10 m non-sterile Roll, price 45 €) and Leukomed® T (8 cm × 10 cm patch, price 1.40 €/each) tapes, for the production of a wearable SERS chip a further cost of 40 €cents can be considered in addition to the aforementioned price. The final average cost per wearable SERS chip is thus below 5 €, at least 3 times less than SERS substrates commercially available. The competitive costs of the proposed AgNWs@PTFE platforms are furthermore supported by time-saving production processes, estimable in three different slots lasting 15 min each for silver deposition, laser patterning and embedding with biocompatible tapes, respectively.

4 Conclusions

In this work we describe a low-cost and time-saving method for producing a SERS sensor chip based on AgNWs deposited on PTFE, which allows the detection of urea and lactate at concentrations ranging from 1.67 to 250 mM. Such concentration range is compatible with typical physiological values of these metabolites in human sweat. The sensor chip was firstly calibrated using a simulated sweat solution, providing a linear response in the 4–250 mM and 1.67–250 mM ranges for urea and lactate, respectively. Moreover, upon functionalization with 4-MBA of AgNWs, we were able to measure the pH of simulated sweat by following the variation of the pH sensitive carboxylate vibrational mode normalized to that of the benzene ring of 4-MBA.

Furthermore, we reported on the integration of the SERS chip with commercial biocompatible tapes in order to obtain a wearable sensor patch for human sweat analysis. As proof of concept, the wearable chip was tested for the estimation of urea and lactate content from real sweat samples from a volunteer during several physical exercise rounds.

These results represent a significant advancement toward the development of a wearable and commercially-scalable sensor chip for sweat analysis by SERS spectroscopy, which could be easily implemented with portable Raman spectrometers for monitoring the health status of patients as well as the level of physical stress of athletes engaged in intense exercise sessions.

Acknowledgments

Authors acknowledge "Officine Riunite" of CNR of Florence, and in particular Andrea Donati from IFAC-CNR, for the technical support.

Funding

This paper was developed within the project funded by Next Generation EU – "Age-It – Ageing well in an ageing society" project (PE0000015), National Recovery and Resilience Plan (NRRP) – PE8 – Mission 4, C2, Intervention 1.3" and Next Generation EU – "Ecosistema dell'Innovazione" project (ECS00000017), National Recovery and Resilience Plan (NRRP) – Tuscany Health Ecosystem (THE), Spoke 4: Nanotechnologies for diagnosis and therapy. The views and opinions expressed are only those of the authors and do not necessarily reflect those of the European Union or the European Commission. Neither the European Union nor the European Commission can be held responsible for them. P.M. and B.W. acknowledge financial support from the Ministry of Foreign Affairs and International Cooperation of Italy (MAECI) and from the National Research Foundation of Korea (NRF) through the DESWEAT project (no._PGR01065; NRF-2019K1A3A1A25000230) funded within the frame of the Executive Program of Scientific and Technological Cooperation between the Italian Republic and the Korean Republic 2019–2021. This research was also supported by the Chung-Ang University research grant in 2024.

Conflicts of Interest

All the authors declare no conflict of interest.

Data availability statement

The raw data supporting the conclusions of this article will be made available by the authors on request.

Author contribution statement

CDA, PM: Conceptualization, Writing – original draft. CDA, MB, PM: Data curation, Investigation, Formal Analysis, Methodology, Visualization. CA: Investigation, Writing – review & editing. PP, FM, MdA, BH: Writing – review & editing. BW, PM: Supervision, Funding acquisition.

References

1 Kim J., Campbell A.S., de Ávila B.E., Wang J. (2019) Wearable biosensors for healthcare monitoring, *Nat. Biotechnol.* **37**, 4, 389–406.
2 Min J., Tu J., Xu C., Lukas H., Shin S., Yang Y., Solomon S.A., Mukasa D., Gao W. (2023) Skin-interfaced wearable sweat sensors for precision medicine, *Chem. Rev.* **123**, 8, 5049–5138.

3 Polykretis P., Banchelli M., D'Andrea C., de Angelis M., Matteini P. (2022) Raman spectroscopy techniques for the investigation and diagnosis of Alzheimer's disease, *Front. Biosci. (Schol. Ed.)* **14**, 3, 22.
4 Barucci A., D'Andrea C., Farnesi E., Banchelli M., Amicucci C., de Angelis M., Hwang B., Matteini P. (2021) Label-free SERS detection of proteins based on machine learning classification of chemo-structural determinants, *Analyst* **146**, 2, 674–682.
5 Ma H., Tian Y., Jiao A., Wang C., Zhang M., Zheng L., Li S., Chen M. (2022) Silk fibroin-decorated with tunable Au/Ag nanodendrites: A plastic near-infrared SERS substrate with periodic microstructures for ultra-sensitive monitoring of lactic acid in human sweat, *Vib. Spectrosc.* **118**, 103330.
6 Koh E.H., Lee W.C., Choi Y.J., Moon J.I., Jang J., Park S.G., Choo J., Kim D.H., Jung H.S. (2021) A wearable surface-enhanced Raman scattering sensor for label-free molecular detection, *ACS Appl. Mater. Interfaces* **13**, 2, 3024–3032.
7 Lu D., Cai R., Liao Y., You R., Lu Y. (2023) Two-dimensional glass/p-ATP/Ag NPs as multifunctional SERS substrates for label-free quantification of uric acid in sweat, *Spectrochim Acta A Mol. Biomol. Spectrosc.* **296**, 122631.
8 Durai L., Badhulika S. (2022) A wearable PVA film supported TiO_2 nanoparticles decorated $NaNbO_3$ nanoflakes-based SERS sensor for simultaneous detection of metabolites and biomolecules in human sweat samples, *Adv. Mater. Interfaces* **9**, 2200146.
9 Liu L., Pancorbo P.M., Xiao T.-H., Noguchi S., Marumi M., Segawa H., Karhadkar S., Gala dePablo J., Hiramatsu K., Kitahama Y., Itoh T., Qu J., Takei K., Goda K. (2022) Highly scalable, wearable surface-enhanced Raman spectroscopy, *Adv. Optical Mater.* **10**, 2200054.
10 Gui X., Xie J., Wang W., Hou B., Min J., Zhai P., Cai L., Tang J., Zhu R., Wu X., Duan J. (2023) Wearable and flexible nanoporous surface-enhanced Raman scattering substrates for sweat enrichment and analysis, *ACS Appl. Nano Mater.* **6**, 11049.
11 Liu Y., Zhang N., Tua D., Zhu Y., Rada J., Yang W., Song H., Thompson A.C., Collins R.L., Gan Q. (2022) Superhydrophobic 3D-assembled metallic nanoparticles for trace chemical enrichment in SERS sensing, *Small* **18**, 2204234.
12 Zhu K., Yang K., Zhang Y., Yang Z., Qian Z., Li N., Li L., Jiang G., Wang T., Zong S., Wu L., Wang Z., Cui Y. (2022) Wearable SERS sensor based on omnidirectional plasmonic nanovoids array with ultra-high sensitivity and stability, *Small* **18**, 2201508.
13 Zhang X., Wang X., Ning M., Wang P., Wang W., Zhang X., Liu Z., Zhang Y., Li S. (2022) Fast synthesis of Au nanoparticles on metal-phenolic network for sweat SERS analysis, *Nanomaterials* **12**, 2977.
14 He X., Fan C., Luo Y., Xu T., Zhang X. (2022) Flexible microfluidic nanoplasmonic sensors for refreshable and portable recognition of sweat biochemical fingerprint, *npj Flex Electron* **6**, 60.
15 Banchelli M., Amicucci C., Ruggiero E., D'Andrea C., Cottat M., Ciofini D., Osticioli I., Ghini G., Siano S., Pini R., de Angelis M. (2019) Spot-on SERS detection of biomolecules with laser-patterned dot arrays of assembled silver nanowires, *ChemNanoMat* **5**, 1036–1043.
16 Sikirzhytski V., Sikirzhytskaya A., Lednev I.K. (2012) Multidimensional Raman spectroscopic signature of sweat and its potential application to forensic body fluid identification, *Anal. Chim. Acta* **718**, 78–83.
17 Moore T.J., Sharma B. (2020) Direct surface enhanced Raman spectroscopic detection of cortisol at physiological concentrations, *Anal Chem.* **92**, 2, 2052.
18 Altun A.O., Bond T., Pronk W., Park H.G. (2017) Sensitive detection of competitive molecular adsorption by surface-enhanced Raman spectroscopy, *Langmuir* **33**, 28, 6999.
19 Chowdhury M.H., Gant V.A., Trache A., Baldwin A., Meininger G. A., Coté G.L. (2006) Use of surface-enhanced Raman spectroscopy for the detection of human integrins, *J. Biomed. Opt.* **11**, 2, 024004.
20 Haes A.J., Van Duyne R.P. (2002) A nanoscale optical biosensor: Sensitivity and selectivity of an approach based on the localized surface plasmon resonance spectroscopy of triangular silver nanoparticles, *J. Am. Chem. Soc.* **124**, 35, 10596.
21 Muehlig A., Jahn I.J., Heidler J., Jahn M., Weber K., Sheen P., Zimic M., Cialla-May D., Popp J. (2019) Molecular specific and sensitive detection of pyrazinamide and its metabolite pyrazinoic acid by means of surface enhanced Raman spectroscopy employing in situ prepared colloids, *Appl. Sci.* **9**, 12, 2511.
22 Huang Y., Liu W., Wang D., Gong Z., Fan M. (2020) Evaluation of the intrinsic pH sensing performance of surface-enhanced Raman scattering pH probes, *Microchem. J.* **154**, 104565.
23 Chung M., Skinner W.H., Robert C., Campbell C.J., Rossi R.M., Koutsos V., Radacsi N. (2021) Fabrication of a wearable flexible sweat pH sensor based on SERS-active Au/TPU electrospun nanofibers, *ACS Appl. Mater. Interfaces* **13**, 51504.
24 Ocean Insight Company. Available at: www.oceaninsight.com.
25 Silmeco Company. Available at: www.silmeco.com.
26 Nikalyte Company. Available at: www.nikalyte.com.
27 SERSitive Company. Available at: www.sersitive.eu.

J. Eur. Opt. Society-Rapid Publ. 2024, **20**, 28

https://doi.org/10.1051/jeos/2024028
Available online at: https://jeos.edpsciences.org

Special Issue - Plasmonica 2023
Antonino Foti and Attilio Zilli (Guest editors)

Journal of the European Optical Society-Rapid Publications

SHORT COMMUNICATION OPEN ACCESS

Towards a portable setup for the on-site SERS detection of miRNAs

Daniel Montesi[a], Sofia Bertone[a], Paola Rivolo, Francesco Geobaldo, Fabrizio Giorgis, Chiara Novara[*], and Alessandro Chiadò

Politecnico di Torino, c.so Duca degli Abruzzi 24, 10129 Torino, Italy

Received 5 April 2024 / Accepted 17 May 2024

Abstract. The actual implementation of on-site analysis of biomarkers, such as miRNAs, depends on the availability of portable and easy-to-handle detection systems that can be used as point-of-care in real life applications. In this work, an automatized microfluidic platform combined with a portable Raman spectrometer is reported and tested for miR-214 detection by surface enhanced Raman scattering (SERS). A multi-chamber SERS-active chip, functionalized according to a previously optimized two-step hybridization assay, was automatically incubated with the analyte solution. Preliminary tests allowed to adjust the portable Raman spectrometer acquisition conditions and to compare the obtained results with those of a bench Raman microscope. Finally, miR-214 at different concentrations was analyzed through an automatic procedure, achieving a limit of detection (LOD) in the picomolar range.

Keywords: Surface enhanced Raman scattering, miRNA, Microfluidic setup, On-site Raman measurements.

1 Introduction

Surface enhanced Raman scattering (SERS) has provided excellent results in optical biosensing, since it can be used for the highly sensitive detection of molecules in complex biological samples, such as cell extracts or biofluids, taking advantage of plasmonic nanostructures [1, 2]. Indeed, the excitation of Localized Surface Plasmon Resonances of noble metal nanoparticles (NPs) generates a great enhancement of the local electric field that can be exploited to boost the Raman scattering efficiency and, thus, the sensitivity. These features are fundamental for the analysis of contaminants in food or in the environment, as well as of drugs and biomarkers in medical applications [3, 4]. In this context, the automatization and simplification of the whole analytical procedure is highly desirable as the measurements have to be performed by non-specialized users [5]. Recently, the availability of portable Raman spectrometers and the integration of plasmonic nanostructures into microfluidic devices allowed the growth of on-site sensing applications of SERS [6, 7]. However, the use of SERS biosensors in real life case studies is still sporadic due to the reduced performances out of the laboratory, to the challenges in the integration of cheap and efficient substrates into microfluidic devices and to the lack of easy-to-handle SERS detection platforms [8].

In this work, the development and optimization of a portable and automatic setup for SERS analyses is reported. The described system includes a motorized sample injection module, a support for the proper positioning of the Raman probe on the SERS-active device, the microfluidic chip and a portable Raman spectrometer, as well as a custom script that allows for syringe-pump and spectrometer control and data processing. As a proof of concept, Ag-decorated porous silicon membranes integrated into a polydimethylsiloxane (PDMS) chip were combined with the portable setup and tested for the detection of miR-214, a biomarker deregulated in several human cancers [9]. Preliminary tests were performed to adjust the acquisition conditions and to set the automatic procedure. Afterwards, the performances of the portable automatized system and of a state-of-the-art bench Raman microscope were compared by analyzing solutions containing several miR-214 concentrations, following a recently optimized two-step hybridization assay [10, 11]. The *in-chip* analysis of miR-214 and its quantification by an entirely automatized procedure was thus demonstrated.

2 Material and methods

The SERS nanostructures (Ag-pSi-PDMS membranes) non-integrated in the microfluidic device were used for preliminary tests and prepared as previously reported [11], while the multi-chamber SERS chip integrating the same

[a] These authors equally contributed to the work.
* Corresponding author: chiara.novara@polito.it

Figure 1. (A) Schematic top view and cross section of the microfluidic chip (dimensions in mm); (B) Representative picture of the multi-chamber microfluidic chip; (C) Experimental setup for portable SERS analyses.

nanostructures was fabricated as in [10, 12] and used for all the other tests. Compared to the previous reference works, little variations have been done to the dimensions of the microfluidic chambers and inlet/outlet ports have been moved from the top PDMS cover to the bottom layer, as detailed in Figure 1A. A picture of the microfluidic chip is reported in Figure 1B. A two-step hybridization assay exploiting DNA probes complementary to the sequence of the target miRNA was employed for miR-214 detection. Briefly, a first probe (H1, 5′-C6SH-ACTGCCTGTCT-3′) is immobilized on the AgNPs surface to capture the analyte from the sample, while the second one (H2, 5′-RGX-GTGCCTGCTGT-3′) binds the captured miRNA and is labelled with Rhodamine Green X (RGX) as Raman reporter, to increase the sensitivity of the assay. These steps were done as detailed in [11]. Instead, the sample incubation step was performed with the automatic injection system, by flushing 100 µL of analyte solution continuously back and forth into the chambers of the microfluidic chip. All the SERS analyses were performed at an excitation wavelength of 532 nm in order to match the plasmon resonance of the employed SERS-active substrates [11]. An InVia Qontor Raman microscope was used as the reference bench-top instrumentation to acquire SERS maps over an area of 110 µm × 110 µm (step size = 55 µm) using a Leica 10× objective (NA 0.22, laser spot size 3.5 µm). A B&W Tek i-Raman plus spectrometer was instead included in the portable setup and used to collect SERS spectra with an optical fiber probe (laser spot size 85 µm) at three different points of the microfluidic chambers. SERS spectra were processed with the HyperSpec R package [13] and the Renishaw software WiRe 5.5 as described in [11]. The WiRe software was also exploited to perform cosmic rays removal and to slightly smooth the raw spectra. The limit of detection (LOD) for the calibrations measured with both setups was calculated as reported in [14] by following the linear regression method.

3 Results and discussion

The presented setup is composed of a portable Raman spectrometer, combined with three syringe-pumps that can be controlled to simultaneously flow the sample or washing solutions into the multi-chamber SERS chip. A special chip holder was designed to allow the microfluidic connections with the syringe-pumps and to optimize the coupling with the optical fiber probe used for the measurements with the portable spectrometer. An image of the setup is shown in Figure 1C. The injection as well as the Raman acquisition parameters can be adjusted through a custom script aimed to automatically run the microfluidics and the optical measurements, whereas only the test-tubes with sample/washing solutions must be manually changed.

Each chamber of the SERS chip integrates AgNPs of an average size of 30 nm that form a homogeneous and densely packed layer on the porous silicon membrane, providing numerous hot-spots for an efficient SERS detection [11].

Preliminary tests were performed to compare the performances of the portable spectrometer with those of the bench Raman microscope. To this aim, solutions with different concentration of Rhodamine 6G, a typical SERS reporter, were incubated on the surface of non-integrated SERS-active nanostructures and measured with the two instruments. As reported in Figure 2A, similar spectra were obtained with the two spectrometers. Indeed, by adjusting the exposure time and the excitation laser power, the vibrational fingerprint of Rhodamine 6G (main peaks at 612, 774, 1364, 1509, 1573 and 1648 cm^{-1} [15]) was detected with comparable intensity and signal-to-noise ratio for the same concentration of the analyte. Then, acquisition conditions were further optimized by analyzing the SERS chip functionalized by the two-step assay with the portable setup. In particular, since proper focusing of solid SERS substrates is crucial, the chip holder was designed to control the distance of the sample vs. the optical fiber probe, which

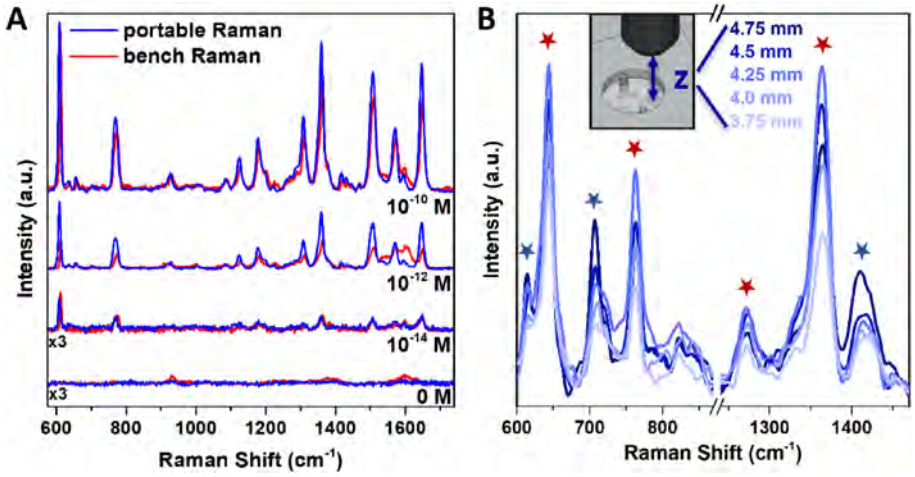

Figure 2. (A) SERS spectra of Rhodamine 6G ethanolic solutions at different concentration (10^{-10}–10^{-14} M) incubated on the non-integrated SERS-active nanostructures measured with a bench Raman microscope (red curves – acquisition time 60 s, laser power 0.02 mW) or with the portable Raman spectrometer (blue curves – acquisition time 150 s, laser power 0.6 mW); (B) Optimization of the chip-optical fiber probe distance ($z = 0$ corresponds to the microfluidic chip surface). SERS spectra (acquisition time 30 s, laser power 3.8 mW) of the microfluidic chip functionalized with the H1 probe, incubated with the target miR-214 at 10 nM concentration and then with 1 μM RGX-labelled H2 probe (red stars: RGX bands; blue stars: PDMS bands).

is used to excite the plasmonic substrate and to collect the scattered beam. As a result, the SERS signal can be maximized to reach satisfying results without a bulky microscope. Figure 2B provides a clear demonstration of this feature: in this example, the microfluidic chip, functionalized with the H1 probe, was incubated with the target miR-214 and then with the RGX-labelled H2 probe. Afterwards, the Raman measurements were performed by moving in z the optical fiber probe. By looking at the vibrational bands of the Raman reporter (highlighted by red stars), it is clear that the maximum of the RGX signal intensity is reached when the probe is located 4.25 mm far from the surface of the chip. In such configuration, the laser beam is suitably focused on the surface of the plasmonic nanostructures integrated in the microfluidic chip, thus maximizing the intensity of the SERS signal and increasing the sensitivity of the bioassay. At the same time, such optimal distance reduces the unwanted background due to PDMS vibrational pattern (blue stars), one of the main components of the microfluidic device.

After these optimizations, the microfluidic chip combined with the portable setup was tested for miR-214 detection and the results compared with those of the bench Raman microscope. Therefore, the AgNPs were functionalized to graft the H1 probe, and then the chip was connected to the microfluidic setup. A volume of 100 μL of miR-214 solution in the 10–0.1 nM range was dynamically incubated in the microfluidic chips, followed by the incubation of the H2-RGX probe at 1 μM concentration. Afterwards, the device was analyzed by means of the bench and portable Raman spectrometers. The results are displayed in Figure 3A and 3B. In both cases the Raman signal of the vibrational bands of RGX at 635 and 1364 cm^{-1} are clearly detectable down to the lowest analyzed concentration, namely 0.1 nM. Moreover, a quantitative comparison of the performances of the bench and portable setups was accomplished by calculating the LOD of miR-214. To this aim, deconvolution procedures through Lorentzian curves were carried out in order to calculate the areas under the isolated peak at 635 cm^{-1}, which were then plotted as a function of the miRNA concentration. By performing a linear regression of such calibration curves, LODs equal to 0.27 nM and 0.21 nM were obtained concerning the measurements with the bench (Figure 3C) or the portable (Figure 3D) spectrometers, respectively. Such result demonstrates that both setups can achieve the same level of sensitivity, within a picomolar regime. This outcome is probably due to the high sensitivity that can be reached in the detection of miRNAs by using the optimized two-step bioassay combined with the integration of the SERS substrates in microfluidic chips. Thus, even with a portable Raman spectrometer a similar sensitivity can be attained at a lower cost, compared to the bench apparatus.

Finally, the automatic spectral analysis was also tested. Indeed, a calibration curve similar to the one reported in Figure 3 can be obtained by analyzing the spectra measured through the portable apparatus by means of custom scripts able to automatically remove the background and calculate the area under the vibrational band of interest. More in detail, 6th-degree polynomial curves were employed to subtract the baseline from the spectra, mostly due to the intrinsic fluorescence of the Raman reporter. An example of such automatic baseline subtraction procedure is reported in Figure 4A. The areas under the RGX peak at 635 cm^{-1} were calculated as the sum of the intensity counts in a specific Raman shift range (615–655 cm^{-1}) and afterwards plotted as a function of the miRNA concentration. The corresponding calibration curve is reported in Figure 4B, which can be exploited to quantify miR-214 in a sample analyzed by means of the portable setup. By performing a linear regression of this calibration curve, a LOD equal to 0.44 nM was obtained. Such value is almost double than

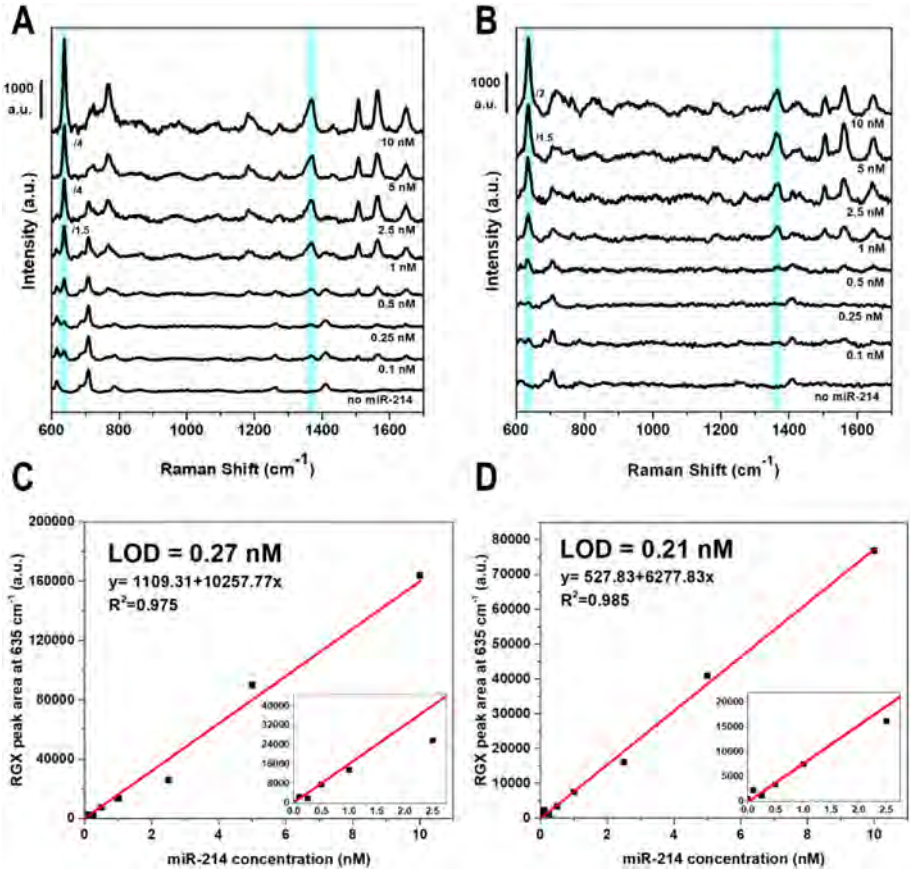

Figure 3. SERS spectra obtained by measuring the plasmonic nanostructures integrated in microfluidic chips and functionalized according to the two-step assay for the detection of miR-214 (0.1–10 nM), by means of (A) the bench (acquisition time 60 s, laser power 0.2 mW) or (B) the portable (acquisition time 10 s, laser power 3.8 mW) Raman spectrometers. The light blue bars highlight the main vibrational bands of RGX reporter. Linear regression of the calibration curves relative to the in-chip SERS analysis of miR-214; (C) obtained with the bench spectrometer; (D) obtained with the portable setup; the insets highlight the trend at the lowest miRNA concentrations.

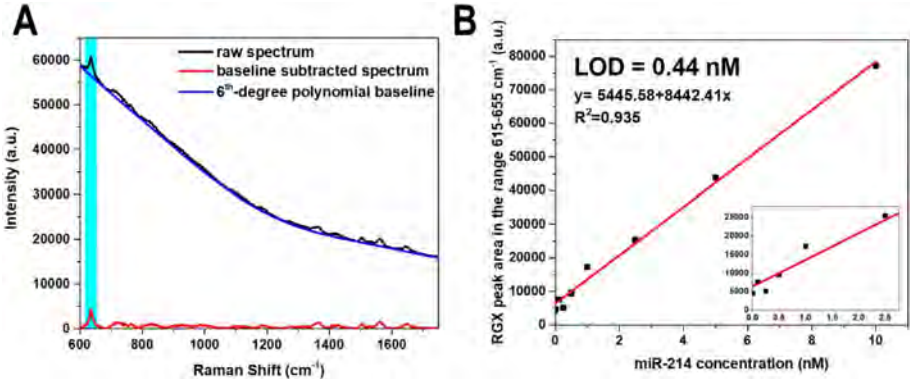

Figure 4. (A) Example of automatic baseline subtraction concerning the analysis of 10 nM miR-214 (main vibrational band of RGX at 635 cm^{-1}, light blue bar); (B) linear regression of the calibration curve obtained by the automatic analysis of the spectra measured with the portable Raman spectrometer. The inset highlights the trend at the lowest miRNA concentrations.

the one previously calculated by manually analyzed spectra. This is probably explained by the rough method employed to automatically process the spectral data. Indeed, the area of the peak of interest calculated as the sum of counts in a predetermined Raman shift interval may include the contribution of overlapped vibrational bands, especially at low target concentrations. Such approach yields a possible overestimation of the detection limit. Nevertheless, it should be

noted that the simplified and automatic procedure developed has the advantage to be suitable for on-site analyses, while rigorous deconvolution processes are extremely difficult to automate with reliability in this kind of applications.

4 Conclusions

A portable and automated setup for the detection of miRNAs by SERS analysis was developed and tested for the detection of miR-214. After a fine adjustment of the acquisition conditions, similar spectra, in terms of intensity and signal-to-noise ratio, were obtained with the portable spectrometer compared to a bench Raman microscope. The performances of the portable setup were checked also by measuring different concentrations of miR-214 with both the bench and the portable Raman spectrometers. Comparable LODs were attained by analysing the spectra acquired with both setups. Moreover, the combination of the SERS-chip with the liquid handling system and the portable Raman spectrometer through custom scripts, allowed to automate both the measures and the analyses, showing a high potential for on-site analyses of miRNAs with a sensitivity at picomolar concentration.

Funding

This publication is part of the project NODES which has received funding from the MUR – M4C2 1.5 of PNRR with grant agreement no. ECS00000036.

Italian Ministry of University and Research (MUR) is acknowledged for funding through the project PRIN 2022 SEMPER (Grant Nr. 20227ZXT4Z).

Conflicts of interest

The authors declare that they have no competing interests to report.

Data availability statement

Data will be made available on request.

Author contribution statement

Conceptualization: AC, CN; Formal analysis: CN, AC and DM; Investigation: DM, SB, AC, PR and CN; Methodology: SB, AC and CN; Supervision: AC, CN, FrG and FaG; Visualization: CN, DM and AC; Writing– original draft: AC; Writing – review & editing: AC, CN, PR, DM, SB, FrG and FaG.

References

1 Langer J., et al. (2020) Present and future of surface-enhanced Raman scattering, *ACS Nano* **14**, 28–117.
2 Fan M., Andrade G.F.S., Brolo A.G. (2020) A review on recent advances in the applications of surface-enhanced Raman scattering in analytical chemistry, *Anal. Chim. Acta* **1097**, 1–29.
3 Perumal J., Wang Y., Attia A.B.E., Dinish U.S., Olivo M. (2021) Towards a point-of-care SERS sensor for biomedical and agri-food analysis applications: A review of recent advancements, *Nanoscale* **13**, 553–580.
4 Liao W., Lu X. (2016) Determination of chemical hazards in foods using surface-enhanced Raman spectroscopy coupled with advanced separation techniques, *Trends Food Sci. Technol.* **54**, 103–113.
5 Jahn I., Zukovskaja O., Zheng X.-S., Weber K., Bocklitz T., Cialla-May D., Popp J. (2017) Surface enhanced Raman spectroscopy and microfluidic platforms: Challenges, solutions and potential applications, *Analyst* **142**, 1022–1047.
6 Guo J., Liu Y., Ju H., Lu G. (2022) From lab to field: Surface-enhanced Raman scattering-based sensing strategies for on-site analysis, *TrAC – Trends Anal. Chem.* **146**, 116488.
7 Sun J., Gong L., Wang W., Gong Z., Wang D., Fan M. (2020) Surface-enhanced Raman spectroscopy for on-site analysis: A review of recent developments, *Luminescence* **35**, 808–820.
8 Guo J., Zeng F., Guo J., Ma X. (2020) Preparation and application of microfluidic SERS substrate: Challenges and future perspectives, *J. Mater. Sci. Technol.* **37**, 96–103.
9 Penna E., Orso F., Taverna D. (2015) miR-214 as a key hub that controls cancer networks: Small player, multiple functions, *J. Investig. Dermatol.* **135**, 960–969.
10 Novara C., Chiadò A., Paccotti N., Catuogno S., Esposito C. L., Condorelli G., De Franciscis V., Geobaldo F., Rivolo P., Giorgis F. (2017) SERS-active metal-dielectric nanostructures integrated in microfluidic devices for label-free quantitative detection of miRNA, *Faraday Discuss.* **205**, 271–289.
11 Novara C., Montesi D., Bertone S., Paccotti N., Geobaldo F., Channab M., Angelini A., Rivolo P., Giorgis F., Chiadò A. (2023) Role of probe design and bioassay configuration in surface enhanced Raman scattering based biosensors for miRNA detection, *J. Colloid Interface Sci.* **649**, 750–760.
12 Novara C., Lamberti A., Chiadò A., Virga A., Rivolo P., Geobaldo F., Giorgis F. (2016) Surface-enhanced Raman spectroscopy on porous silicon membranes decorated with Ag nanoparticles integrated in elastomeric microfluidic chips, *RSC Adv.* **6**, 21865–21870.
13 Beleites C., Sergo V. (2015) *hyperSpec: A package to handle hyperspectral data sets in R.* http://hyperspec.r-forge.r-project.org.
14 Shrivastava A., Gupta V. (2011) Methods for the determination of limit of detection and limit of quantitation of the analytical methods, *Chronicles Young Sci.* **2**, 21–25.
15 Virga A., Rivolo P., Frascella F., Angelini A., Descrovi E., Geobaldo F., Giorgis F. (2013) Silver nanoparticles on porous silicon: Approaching single molecule detection in resonant SERS regime, *J. Phys. Chem. C* **117**, 20139–20145.

J. Eur. Opt. Society-Rapid Publ. 2024, **20**, E1
© The Author(s), published by EDP Sciences, 2024
https://doi.org/10.1051/jeos/2024038
Available online at: https://jeos.edpsciences.org

Special Issue - Plasmonica 2023
Antonino Foti and Attilio Zilli (Guest editors)

Journal of the European Optical Society-Rapid Publications

EDITORIAL OPEN ACCESS

PLASMONICA and JEOS-RP: A new partnership for European nanophotonics

Antonino Foti[1] and Attilio Zilli[2,*]

[1] CNR-IPCF, Istituto per i Processi Chimico-Fisici del Consiglio Nazionale delle Ricerche – Viale F. Stagno D'Alcontres 37, I-98156, Messina, Italy
[2] Department of Physics, Politecnico di Milano – Piazza L. da Vinci 32, 20133, Milano, Italy

Plasmonica (https://www.plasmonica.it) is the Italian community of researchers in nanophotonics. It was founded in 2013 by a collective of young physicists, when nanophotonics still was a niche endeavor in Italy. In 2015, Plasmonica joined the Italian Society of Optics and Photonics (SIOF, the Italian branch of EOS) and since then has been active within it as the *Plasmonics and Nano-Optics Working Group*. Over the past decade, this community has flourished and earned recognition also beyond the national borders. Throughout this evolution, its mission has not changed: organizing events and other initiatives aimed at gathering the Italian nanophotonics community, whose research interests are spread across different disciplines such as physics, engineering, chemistry, and biology; and fostering its connections to wider European research networks. Plasmonica is also particularly committed to supporting early-stage researchers by encouraging their scientific development through doctoral schools, and by providing them with a platform to showcase their work to broad academic audiences.

This Special Issue is linked to the 2023 edition of the annual workshop of Plasmonica – a special occasion to mark the tenth anniversary of the foundation of the community – which was held in Politecnico di Milano, Italy. The selection of manuscripts we received from the participants of the workshop spans across the whole breadth of the scope of Plasmonica, ranging from the fabrication and study of the optical properties of plasmonic materials [1] and dielectric nanoresonators [2] to the enhancement and control of nonlinear [3] and chiral [4] light with nanostructures, and including examples of plasmon-enhanced sensing [5] as well as demonstrations of plasmonic biosensors based on surface-enhanced Raman scattering [6, 7] which are closer to the prototype stage.

We sincerely thank Prof. Paolo Biagioni of Politecnico di Milano, Italy (co-founder of Plasmonica, past president of SIOF, and presently in the EOS Board of Directors) and Prof. Emiliano Descrovi of Politecnico di Torino, Italy (EOS President Elect). They conceived this Special Issue which, without their coordination activity between EOS and SIOF and their promotional efforts within the Plasmonica community, would not have seen the light. Finally, we wish to acknowledge the generous contribution towards the article processing charges offered by SIOF – particularly thanks to the commitment of Prof. Alessandro Belardini of Sapienza University of Rome (SIOF secretary and member of the EOS Board of Directors).

Let us conclude this Editorial with an announcement concerning the future of the collaboration between Plasmonica and JEOS-RP. This Special issue was initially intended as a one-off initiative, but its warm reception encouraged the Steering Committee of Plasmonica to continue and expand it in the form of an open-ended Collection. Its goal is to establish a go-to venue for gathering and highlighting the ongoing research of the Plasmonica community, so as to progressively make JEOS-RP a more visible and attractive outlet for researchers in plasmonics and nano-optics throughout Europe. Indeed, much like this Special Issue, the upcoming Collection is motivated by the intent of Plasmonica to tangibly support a scientific society-based publication model – that is, made by scientists and for scientists. Moreover, it strives to leverage the synergy between SIOF and EOS to redress a bit the current imbalance of the publishing ecosystem, by trying to tilt the scale back towards European-based scholarly circuits. Indeed, most of the output of the European research in optics is currently published in journals which are commercially owned and/or based overseas, with a significant portion of research funding thus drained with little return to the European research environment. We hope that the successful realization of editorial initiatives like this Special Issue and the Plasmonica Collection will contribute to spread within the European optical community the awareness of being an actor fully capable of self-determining its own publishing and research policies.

References

1 Celebrano M, Savoini M, Biagioni P, Della Valle G, Pellegrini G, Cantoni M, Rinaldi C, Cattoni A, Petti D, Bertacco R, Duò L, Finazzi M, Towards the epitaxial growth of Au thin films on MgO substrates for plasmonic applications, *J. Eur. Opt. Society-Rapid Publ.* **20**, 1, 12 (2024). https://doi.org/10.1051/jeos/2024011.

* Corresponding author: attilio.zilli@polimi.it

2 Mignuzzi S, Wu X, Hecht B, Frigerio J, Isella G, Celebrano M, Finazzi M, Sapienza R, Biagioni P, Germanium Fabry-Perot nanoresonators investigated by cathodoluminescence spectroscopy, *J. Eur. Opt. Society-Rapid Publ.* **20**, 1, 14(2024). https://doi.org/10.1051/jeos/2024012.
3 Petronijevic E, Sibilia C, Tailoring second harmonic emission by ZnO nanostructures: Enhancement of directionality, *J. Eur. Opt. Society-Rapid Publ.* **20**, 1, 11 (2024). https://doi.org/10.1051/jeos/2024009.
4 Skubisz C, Petronijevic E, Leahu G, Cesca T, Scian C, Mattei G, Sibilia C, Belardini A, Photo-acoustic technique with widely tuneable laser: Metasurface circular dichroism response, *J. Eur. Opt. Society-Rapid Publ.* **20**, 1, 20 (2024). https://doi.org/10.1051/jeos/2024016.
5 Polito R, Sotgiu S, Sohrabi F, Ferrando G, Berkmann F, Temperini ME, Giliberti V, Buatier de Mongeot F, Ortolani M, Baldassarre L, Giordano MC, Polarization-resolved surface-enhanced infrared spectra with nanosensors based on self-organized gold nanorods, *J. Eur. Opt. Society-Rapid Publ.* **20**, 1, 15 (2024). https://doi.org/10.1051/jeos/2024015.
6 D'Andrea C, Banchelli M, Amicucci C, Polykretis P, Micheletti F, de Angelis M, Hwang B, Matteini P, Development of a wearable surface enhanced Raman scattering sensor chip based on silver nanowires for rapid detection of urea, lactate and pH in sweat, *J. Eur. Opt. Society-Rapid Publ.* **20**, 1, 10 (2024). https://doi.org/10.1051/jeos/2024013.
7 Montesi D, Bertone S, Rivolo P, Geobaldo F, Giorgis F, Novara C, Chiadò A. Towards a portable setup for the on-site SERS detection of miRNAs, *J. Eur. Opt. Society-Rapid Publ.* **20**, 1, 28 (2024). https://doi.org/10.1051/jeos/2024028.

PLASMONICA

The Italian Community of Plasmonics and Nano-optics

The Italian Society of Optics and Photonics (SIOF, Società Italiana di Ottica e Fotonica) is the Italian branch of the European Optical Society (EOS) and serves as the national reference organization for the Italian community active in optics and photonics.

Within SIOF, the PLASMONICA Working Group, established in 2015, brings together the Italian researchers in plasmonics and nano-optics. Its mission is to promote scientific coordination, knowledge exchange, and the consolidation of national expertise in these rapidly advancing, cutting-edge research areas. The Working Group originated from the annual PLASMONICA workshop series, launched in 2013 by a group of young Italian physicists to provide a dedicated forum for researchers in nano-plasmonics—at the time still a pioneering field within the Italian research landscape. Over the past decade this community has thrived and vastly expanded its reach internationally; accordingly, the core mission of PLASMONICA is to bring together the Italian nanophotonics community across disciplines such as physics, engineering, chemistry, and biology, fostering collaboration, mobility, dissemination (seminars and workshops), and outreach activities while covering a broad scientific scope that includes nanoresonators, meta-optics, thermo- and magneto-plasmonics, ultrafast and nonlinear phenomena, quantum plasmonics, strong coupling in nanoscale systems, chiral effects, near-field optics, surface- and tip-enhanced spectroscopies, optical forces at the nanoscale, plasmonic (bio)sensing, semiconductor and THz plasmonics, and novel optical nanomaterials. A distinctive feature of PLASMONICA is its strong commitment to fostering early-stage researchers, whom it supports by providing opportunities for their scientific development and the chance to present and discuss their work.

These guiding principles shape the two main activities of the group, namely the organization of an annual workshop and a biennial residential school. Both events are held in person and conducted in English to encourage participation from the broader international community and to align with European research priorities. All the events were organized by research groups working on plasmonics and nano-optics across Italy, as shown in the map, promoting a shared sense of community, enhancing mutual visibility, and ensuring that all participating groups are fully recognized as active and integral members of the PLASMONICA network, within a framework characterized by a bottom-up approach and transparent governance.

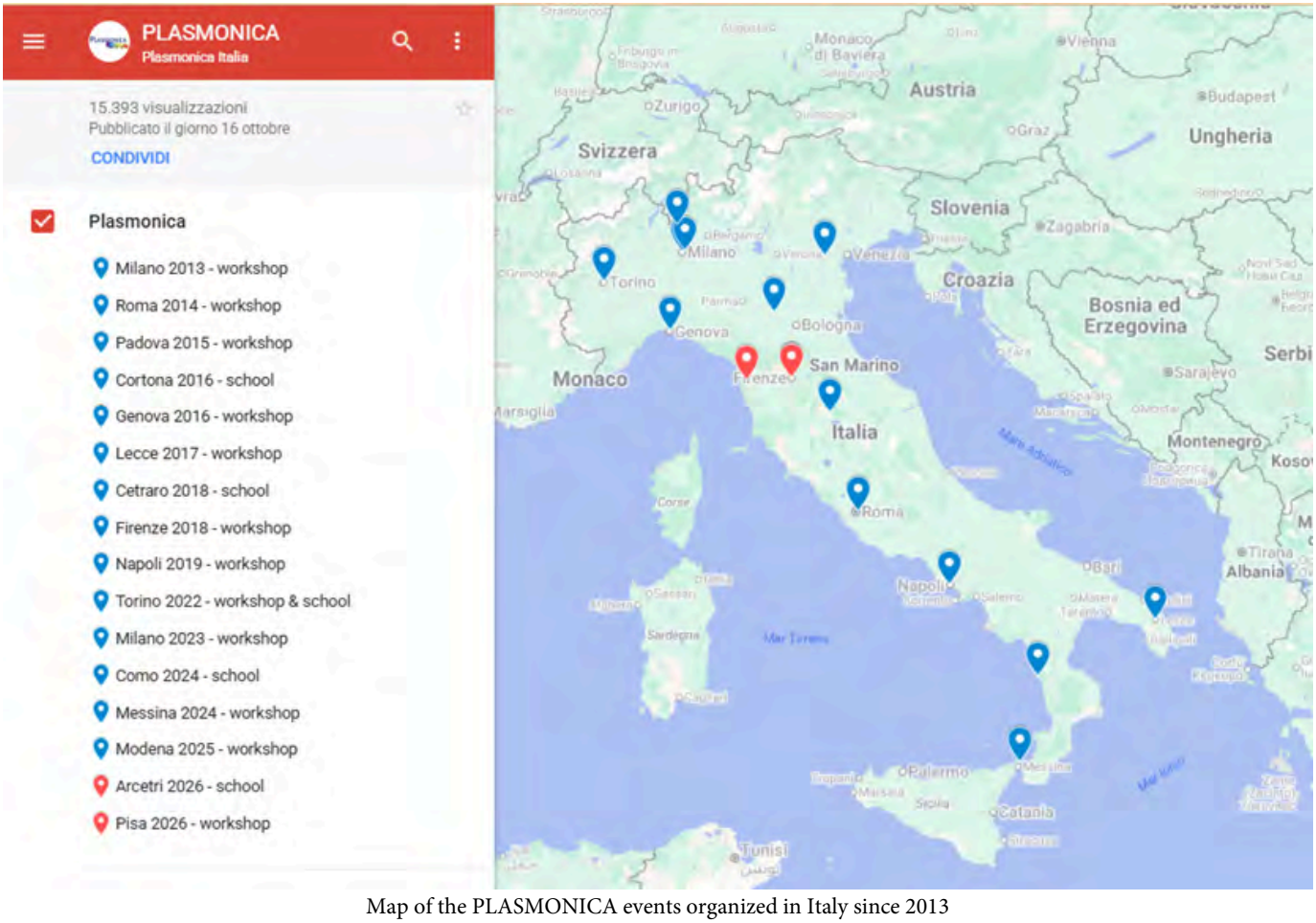

Map of the PLASMONICA events organized in Italy since 2013

Compared to other major conferences, PLASMONICA events provide a more accessible research environment with reduced competition and greater opportunities for dialogue, foster genuine collaborations among research groups. Moreover, they often represent the first venue where PhD students and postdoctoral researchers can present their work, and facilitate access to national and international projects by enhancing the awareness of ongoing research activities within the closely connected community.
Ultimately, the joint action of SIOF and PLASMONICA, with the endorsement of EOS, supports cross-border collaboration and strengthens the engagement of Italian research groups within the European research system, contributing to the development of strategic roadmaps in nanophotonics, advanced sensing, integrated photonics, and emerging quantum technologies.

UPCOMING EVENTS

The next school and workshop of PLASMONICA are both scheduled for 2026. The former will be held in Florence at the Galileo Galilei Institute from March 23rd to 27th, while the latter will be held at the University of Pisa from July 8th to 10th (more info soon available). Up-to date information on the upcoming events can be found on the organization website www.plasmonica.it as well as on our social channels @plasmonica on X/Twitter, BlueSky, Instagram and SIOF-plasmonica on LinkedIn.

Why Publish in JEOS-RP?

- Rigorous peer review
- Strict ethical policies following the COPE code of conduct (read more)
- Rapid publication: median time from submission to online publication of preprint ≈ 73 days (calculated over 2023)
- 2024 impact factor: 3.2
- Very fair publication fees with further discounts for EOS members
- Open-access Creative Commons licence (CC BY)
- Author services: performant search engine, article metrics, bookmarking, online submission, and peer review portal ...
- Reader services: free e-mail alerts and RSS Feeds, CrossRef®, and DOI
- Large visibility of the published papers through indexation in main databases
- 2024 immediacy index: 0.9

PLASMONICA

The Italian Community of Plasmonics and Nano-optics

Collection

www.plasmonica.it/#collection

Società Italiana di Ottica e Fotonica

PLASMONICA COLLECTION TOPICAL ISSUE:

Submission is restricted to authors belonging to the Plasmonica community, whose core mission is gathering the nanophotonics community in Italy.

The papers included in this Topical Issue are published within the regular volumes of the Journal of the European Optical Society – Rapid Publications (JEOS-RP).

JEOS-RP published by EDP Sciences in cooperation with:

DGaO Deutsche Gesellschaft für angewandte Optik — The German Branch of the European Optical Society

SIOF Società Italiana di Ottica e Fotonica

SEDOPTICA SOCIEDAD ESPAÑOLA DE ÓPTICA

PromOptica

SPOF

Photonics Finland

LOS LATVIAN OPTICAL SOCIETY — The Latvian Branch of the European Optical Society